Multiferroic perovskites under epitaxial strain

Daumont, Cristophe

Multiferroic perovskites under epitaxial strain: The case of $TbMnO_3$ thin films.

Christophe Daumont

Front cover pictures: Temperature dependence of the Cole-Cole plot for a 40nm $TbMnO_3$ film grown at 0.9mbar. Evolution of the Density of domain walls and the magnitude of the ZFC-FC splitting as a function of the inverse thickness of $TbMnO_3$ films grown at 0.9mbar. Transmission electron microscopy plane-view image of a $TbMnO_3$ film grown on $SrTiO_3$. Grazing incidence diffraction map around the (110) of the $SrTiO_3$ substrate evidencing domains formation.

Back cover picture: Snapshot of the laser plume during deposition of $BiFeO_3$ on a $SrTiO_3$ substrate.

Background: Picture of the vineyard in the region of Champagne, France.

Cover design: Christophe Daumont.

University of Groningen
Zernike Institute
for Advanced Materials

The work described in the thesis was performed in the Chemical Physics department of the Zernike Institute for Advanced Materials, University of Groningen, Nijenborgh 4, 9747AG Groningen, The Netherlands. Financial support provided by the Zernike Institute for Advanced Materials and the European MaCoMufi project.

Christophe Daumont,
Multiferroic perovskites under epitaxial strain: The case of $TbMnO_3$ thin films.

Printed by: Facilitair Bedrijf RuG, Groningen.
ISBN: 978-90-367-4030-2
Zernike Institute for Advanced Materials Ph.D. thesis series 2009-08.
ISSN:1570-1530

UNIVERSITEIT VAN GRONINGEN

Multiferroic perovskites under epitaxial strain: The case of $TbMnO_3$ thin films

Proefschrift

ter verkrijging van het doctoraat in de
Wiskunde en Natuurwetenschappen
aan de Rijksuniversiteit Groningen
op gezag van de
Rector Magnificus, dr. F. Zwarts,
in het openbaar te verdedigen op
maandag 19 oktober 2009
om 11.00 uur

door

Christophe Jean Maurice Daumont

geboren op 3 juni 1979
te Troyes, Frankrijk

Promotores: Prof. dr. B. Noheda
Prof. dr. T.T.M. Palstra

Beoordelingscommissie: Prof. dr. J. Fontcuberta
Prof. dr. P. Rudolf
Prof. dr. ir. P.H.M. van Loosdrecht

ISBN:
Digital: 978-90-367-4029-6
Printed: 978-90-367-4030-2

I dedicate this thesis to my family and friends.

Contents

Chapter 1

General introduction

1.1 Multiferroic materials

Multiferroic materials form a special class of materials exhibiting coexistence of two or more ferroic orders (ferromagnetism, ferroelectricity and ferroelasticity) [1–8]. This coexistence is difficult to achieve for various reasons. On the one hand, in most conventional ferroelectrics, the chemical bonding, which results in an off-centre position of the transition metal ions creating electric polarization, requires a formally empty d-electron configuration. On the other hand, ferromagnetism requires unpaired d-electrons. Then, the coexistence of the two properties seems incompatible with the local chemistry [2]. Therefore, non-conventional mechanisms are required to explain the occurrence of multiferroicity in materials and to create new multiferroics.

Initially, partial substitution of ferroelectrics with paramagnetic cations was proposed [9]. In this case, the requirements for the d-shell are met, and one crystallographic site may contain both an empty d-shell cation and a partially filled d-shell cation [9]. Examples of this mechanism are compounds such as $PbFe_{1/2}Nb_{1/2}O_3$ [10] and $PbFe_{1/2}Ti_{1/2}O_3$ [11]. Another mechanism leading to multiferroic behaviour is using the stereochemical activity of Bi^{3+} and/or Pb^{2+} "lone pairs", as in the case of $PbVO_3$, $BiFeO_3$ or $BiMnO_3$, although the multiferroic nature of $BiMnO_3$ is still disputed [12–23]. In these compounds, the ferroelectric distortion is caused by the 6s lone pair, while Fe/Mn/V are responsible for the magnetism [2, 13, 24]. However, due to the different origin of ferroelectricity and magnetism in these materials, the coupling be-

tween these two properties is generally weak [2,3].

Other mechanisms, by which the polar state is induced by an unconventional type of ordering, can also be found. Examples are the geometric ferroelectrics, in which the structure is distorted in a complex way. Hexagonal $YMnO_3$ is an example of such a multiferroic, in which ferroelectricity is induced by a tilting of the MnO_5 bipyramids and buckling of the Y-O planes [2,25–28]. Another mechanism relates to charge ordering. In some materials, charge ordering can give rise to polarization. This was theoretically predicted for systems with intermediate site-centred and bond-centred charge ordering [29], and observed for $LuFe_2O_4$ [3, 4]. Finally, important cases, in terms of the magnitude of the coupling, are those in which the polar state is directly induced by the magnetic ordering. Examples of such systems are the spiral magnets. In these materials, the polar state arises from the breaking of inversion symmetry by a spin cycloidal structure [30]. $TbMnO_3$, the subject of this thesis, belongs to this class of spiral magnets.

A related class of materials are magnetoelectric (ME) materials. Here, a polarization (magnetization) is linearly induced by an applied magnetic (electric) field [31]. The search for materials showing the ME effect started with the prediction of a possible ME coupling [32]. This was soon afterwards observed in Cr_2O_3 [33, 34]. The ME effect is currently having a revival due to its potential for data storage and other applications [7]. Figure 1.1 shows the relationship between multiferroic and magnetoelectric materials, within the broader class of materials that are susceptible to polarize or magnetize under electrical or magnetic fields. This figure shows that not all multiferroics display ME coupling and that not all materials exhibiting ME coupling are multiferroics. However, it is believed that the largest ME couplings are to be found among the multiferroic materials. The nature of the coupling in multiferroic and magnetoelectric materials is still not fully understood and has attracted much interest in the past years, also from a fundamental perspective.

There has been renewed interest in studying the perovskite-based multiferroic materials, such as rare earth manganites $TbMn_2O_5$, $YMnO_3$, $BiMnO_3$, $HoMnO_3$ etc., which

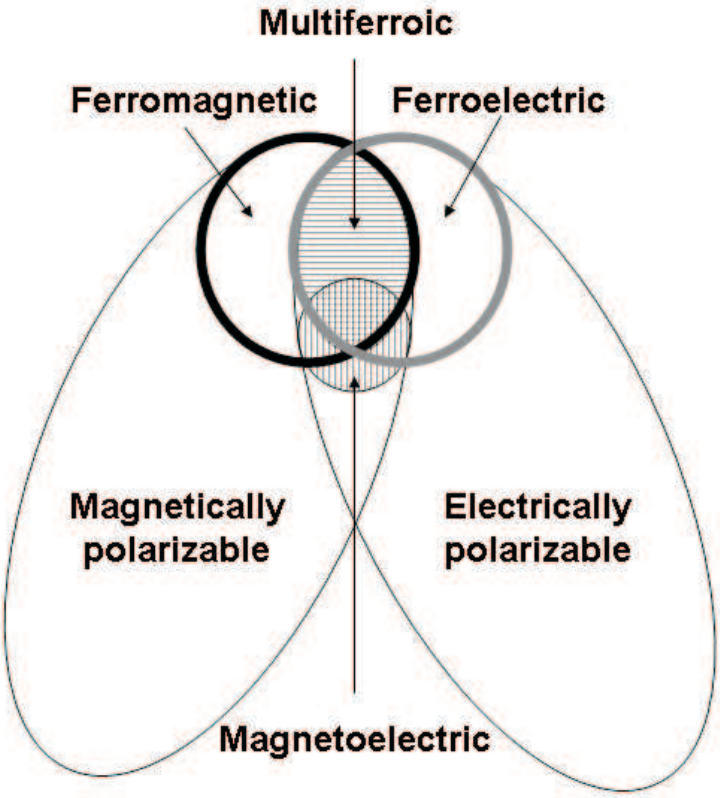

Figure 1.1: *Ferromagnetic (ferroelectric) materials have spontaneous magnetization (polarization), as shown by the black (grey) circle. The horizontally hatched region represents the multiferroics, a class of materials in which both a spontaneous polarization and magnetization are present within the same phase. The vertical hatched region shows the class of magnetoelectric materials, in which both the electrical and magnetic properties are coupled linearly to both applied electrical and magnetic fields. This figure is adapted from [7].*

have been shown to display large magnetoelectric effects. Although ferromagnetic multiferroics are preferred for applications, most of the multiferroics under investigation are antiferromagnets. This is because very few ferromagnets are good insulators, an important requirement for ferroelectricity. Moreover, recent efforts have been made to synthesize new multiferroics in the form of thin films, desirable for applications [35–37]. Interesting substrate effects, due to the epitaxial strain, can be obtained, such as stabilization of new phases that do not exist in bulk, modifications of the ferroelectric and magnetic exchange interactions or changes in electronic properties. Strain effects can be difficult to assess due to extrinsic effects, such as secondary

phases, difficulties in the synthesis of good quality materials and issues related to the characterization of very small volumes of material present in thin films. Therefore, a general explanation of the role of strain in multiferroic materials has still not been formulated. Since the main exchange interactions are sensitive to changes in the metal-oxygen bond angle and bond distances, not only the investigation of the physical response, but also an exhaustive study of the structure is essential for understanding the physics behind epitaxial strain effects.

1.2 Perovskite-based compounds

When attempting epitaxy, the relatively simple chemistry and structure of perovskites is very helpful. Moreover, several ferromagnets, various ferroelectrics and some of the most popular multiferroic materials are perovskites.

The general formula for perovskite-based materials is ABO_3, where A and B are cations with different sizes and/or valences. The B cation is located at the centre of 6 oxygen atoms with a octahedral coordination. The ideal perovskite structure is cubic, as shown in figure 1.2 (a). The distortion of the perovskites from the cubic symmetry is measured by the so-called tolerance factor, defined by Goldschmidt in the early 1920's [38], and expressed as:

$$t = \frac{r_A + r_O}{\sqrt{2}(r_B + r_O)} \tag{1.1}$$

where r_A, r_B and r_O are the ionic radii of A cation, B cation and oxygen O, respectively. Almost all perovskites have a tolerance factor between 0.75 and 1. Moreover, the distortion of the unit cell increases as the tolerance factor decreases from 1 (the tolerance factor for an ideal cubic perovskite).

1.3 Structure of bulk $TbMnO_3$

The perovskite terbium manganite has an orthorhombic unit cell (space group: Pbnm), as shown in figure 1.2 (b), a tolerance factor of 0.89, and lattice parameters of a_o = 5.2931 Å, b_o = 5.8384 Å, and c_o = 7.4025 Å [39]. The lattice parameters reported for bulk/single crystal samples, in particular the c-lattice parameter, vary significantly. This variation has been attributed to different growth conditions and it is most likely due to different oxygen contents [40–42]. The unit cell is rotated by 45^o around the c-axis, with respect to the primitive cubic cell, it is doubled along the c axis and multiplied by $\sqrt{2}$ along the a and b-axis. The unit cell thus contains 4 formula units (see figure 1.2 (b)).

This is due to the distortion and tilt of the oxygen octahedra (antiphase rotation of the oxygen octahedra along the a and b axes of the pseudo cubic unit cell and the in-phase rotation along the c axis of the pseudocubic unit cell), which is known as $GdFeO_3$ distortions [43, 44]. The in-phase and antiphase rotations of the oxygen octahedra, in the space group Pbnm, can be described as $a^-a^-b^+$, using the Glazer notation [45]. This type of distortion is associated with orthorhombic lattice parameters that follow the relationship $c_o/\sqrt{2} > a_o$ and $a_o < b_o$. The lattice parameters, in the case of $TbMnO_3$, have a different relationship ($c_o/\sqrt{2} < a_o$), indicating that the Pbnm structure of $TbMnO_3$ presents another distortion superimposed on the $GdFeO_3$-like rotations.

Indeed, the manganese ions in the structure are in an octahedral coordination and possess a valence of 3+. In the high spin state (S=2), three electrons occupy the t_{2g} orbitals and one electron occupies the doubly degenerate e_g orbitals. This implies that the high spin state of manganese in $TbMnO_3$ is Jahn-Teller active (see table 1.1) [46]. Moreover, the manganese ions can also exist in a low spin state (S=1) with 4 electrons occupying the t_{2g} orbitals, leading to a weak Jahn-Teller effect in this spin state (as shown in table 1.1).

The Jahn-Teller effect is most pronounced when an odd number of electrons oc-

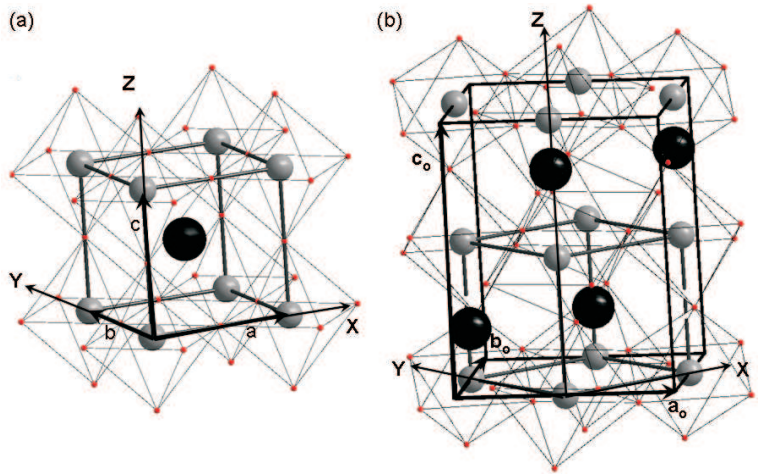

Figure 1.2: *(a) Crystal structure of ABO_3 in its cubic form. (b) Crystal structure of $TbMnO_3$ in its room temperature orthorhombic symmetry, as indicated by black contour. The pseudo cubic unit cell is drawn inside the orthorhombic unit cell as grey contour.*

Table 1.1: *Strength of the Jahn Teller effect in an octahedral TM-O_6 complex considering the number of electrons in the d orbitals of the transition metal TM. s=strong effect; w=weak effect.*

number of electrons	1	2	3	4	5	6	7	8	9	10
High spin	w	w	-	s	-	w	w	-	s	w
Low spin	w	w	-	w	w	-	s	-	s	-

cupy the e_g orbitals. This is because the e_g orbitals point directly at the coordinating oxygen atoms. The effect also occurs for a strong degeneracy of electrons in the t_{2g} orbitals. However, the effect is much less noticeable than when e_g orbitals are involved, because the t_{2g} orbitals do not point directly in direction of the coordinating oxygens. The expected effects for an octahedrally coordinated system are given in table 1.1.

The Jahn-Teller effect leads to distortions of the oxygen octahedron as shown in figure 1.3.

Another effect of the Jahn Teller distortion is the lifting of degeneracy of the e_g orbitals, stabilizing the d_{z^2} or $d_{x^2-y^2}$ orbitals depending on if the Jahn-Teller distortion compresses or expands one of the directions of the oxygen octahedra (Q3 mode).

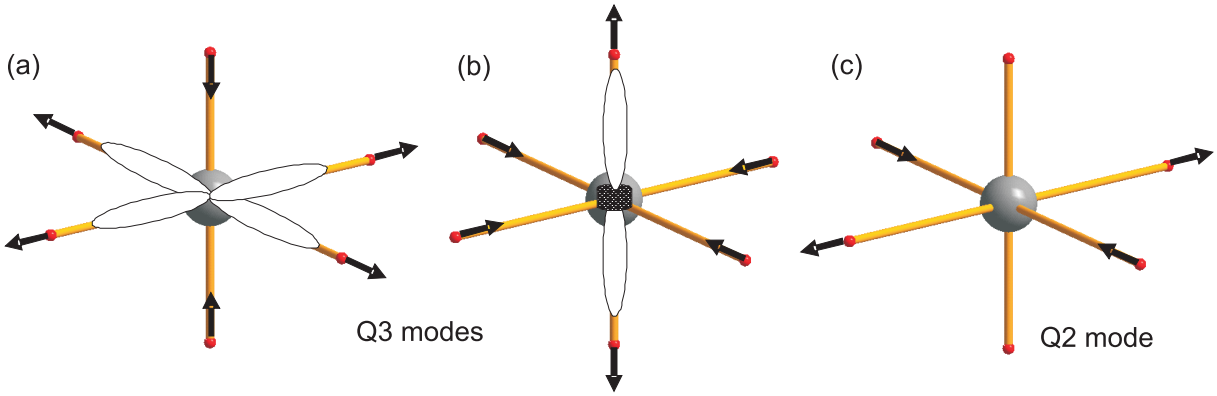

Figure 1.3: *(a), (b) Two different types of Q3 mode of Jahn-Teller distortion stabilizing the $d_{x^2-y^2}$ and d_{z^2}, respectively. (c) Q2 mode of the Jahn-Teller distortion favouring a superposition of $d_{x^2-y^2}$ and d_{z^2}.*

Compression in the (ab)-plane stabilizes the d_{z^2} orbital whereas expansion stabilizes the $d_{x^2-y^2}$ orbital, as shown in figure 1.3 (a) and (b). The Jahn-Teller distortion can also produce an effect of orthorhombic distortion of the oxygen octahedra (Q2 mode), stabilizing a superposition of the d_{z^2} and $d_{x^2-y^2}$ orbitals (as shown in figure 1.3 (c)). In the case of $TbMnO_3$, the longest Mn-O bond is on the (ab) plane, whereas the shortest Mn-O bond is along the out-of-plane direction. This means that the $d_{3x^2-r^2}$ and $d_{3y^2-r^2}$ orbitals are stabilized in $TbMnO_3$ as shown in figure 1.4 (a). Finally, a cooperative Jahn-Teller distortion in a thin film under epitaxial strain might influence the cation-ligand-cation superexchange interactions; this is further described in the next section.

1.4 Superexchange and double-exchange interactions.

The magnetic interactions in $TbMnO_3$ are dominated by the so-called 'superexchange'. Superexchange is the magnetic coupling between two ions (Mn^{3+}) through a nonmagnetic intermediate anion (O^{2-}) and was originally proposed by Kramers in 1934. He noticed that in crystals like MnO, the Mn atoms interact magnetically despite having a nonmagnetic oxygen ion between them [47]. Anderson later refined Kramers' model [48]. The main features of the superexchange interactions are usually summa-

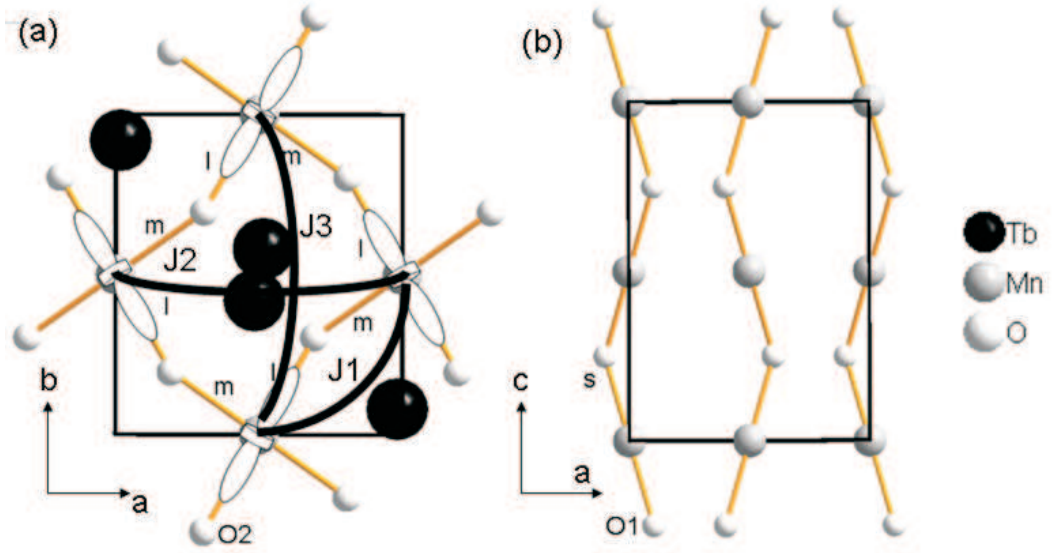

Figure 1.4: *(a) Representation of the structure of $TbMnO_3$ in the (ab) plane. The alternating medium and long bond length are indicated as 'm' and 'l', respectively. The stabilized $d_{3x^2-r^2}$ and $d_{3y^2-r^2}$ are represented by their classical shape. The NN and NNN superexchange interactions are shown in the picture, denoted by J1 (nearest neighbour superexchange), J2 (next nearest neighbour along a) and J3 (next nearest neighbour along b). (b) Representation of the structure of $TbMnO_3$ in the (ac) plane. The short bond length is indicated a 's' in the picture. This representation emphasizes the tilting of the oxygen octahedra along the c axis of the structure.*

rized by the so-called 'Goodenough-Kanamori-Anderson (GKA)' rules. According to these rules, the 180^o superexchange between two magnetic ions, in which the magnetic ion-ligand-magnetic ion angle is closest to 180^o, is strongly antiferromagnetic. The 90^o superexchange (magnetic ion-ligand-magnetic ion angle close to 90^o) interaction is weakly ferromagnetic. Moreover, the 180^o superexchange is maximum for an angle of 180^o, allowing maximum overlap of the relevant orbitals. The 180^o superexchange becomes weaker as the angle decreases [49].

The GKA rules are valid for transition metals that are not Jahn-Teller active. For Jahn-Teller distorted systems, the 180^o superexchange rules are different. Superexchange adheres to the quantum mechanic requirement of an antisymmetric total wave function. For cooperatively Jahn-Teller distorted perovskites, the antisymmetric wave function is imposed by the antiferrodistorted structure. The latter is the result of the corner-sharing octahedra of the perovskite structure, as described in the previous sec-

tion. Thus, the orbital part of the wave function imposes the antisymmetric symmetry and thus the magnetic interaction is ferromagnetic in the a-b basal plane. For Pbnm-symmetry perovskites, the mirror symmetry perpendicular to the c-axis results in the same orbital occupation along the c-axis. This imposes antiferromagnetic interactions along the c-axis.

Besides superexchange, there is another interaction for mixed valence compounds. E.g. for Mn^{3+}-O-Mn^{4+} fragments, charge transport results in a stabilization of the ferromagnetic interactions. This mechanisms operates for doped compounds and is known as double-exchange. Here, it involves the simultaneous charge transfer of an electron from Mn^{3+} to O^{2-} and another from O^{2-} to Mn^{4+}. For high enough doping, it can lead to a metallic ferromagnetic state as e.g. in $La_{1-x}Ca_xMnO_3$ for $0.2 < x < 0.5$.

1.5 $TbMnO_3$ and its complexity.

In bulk form, $TbMnO_3$ is one of the most popular multiferroics. In manganites, the magnetic ground state as a function of the size of the A-site cation shows a rich behaviour that gives rise to different magnetic structures. Changing the size of the A-site cation by choosing different rare earth ions is known as applying 'chemical pressure'.

The magnetic structure of bulk $TbMnO_3$ is complicated and is the result of the competition between ferromagnetic (FM) and antiferromagnetic (AFM) interactions, leading to frustration and incommensurability of the spin structure. This competition arises as the Mn-O-Mn bond angle gives rise to intermediate interactions between antiferromagnetic 180^o superexchange and ferromagnetic 90^o superexchange [49]. This material is then an interesting candidate for studying the effect of epitaxial strain. Indeed, as shown in figure 1.5, $TbMnO_3$ lies in between two different magnetic structures. For Mn-O-Mn bond angles higher than 146^o, an A-type antiferromagnetic structure is found, as in the case of $LaMnO_3$ [51]. For bond angles lower than 144^o, an E-type antiferromagnetic structure is found, as in the case of $HoMnO_3$ [52]. Both A-type

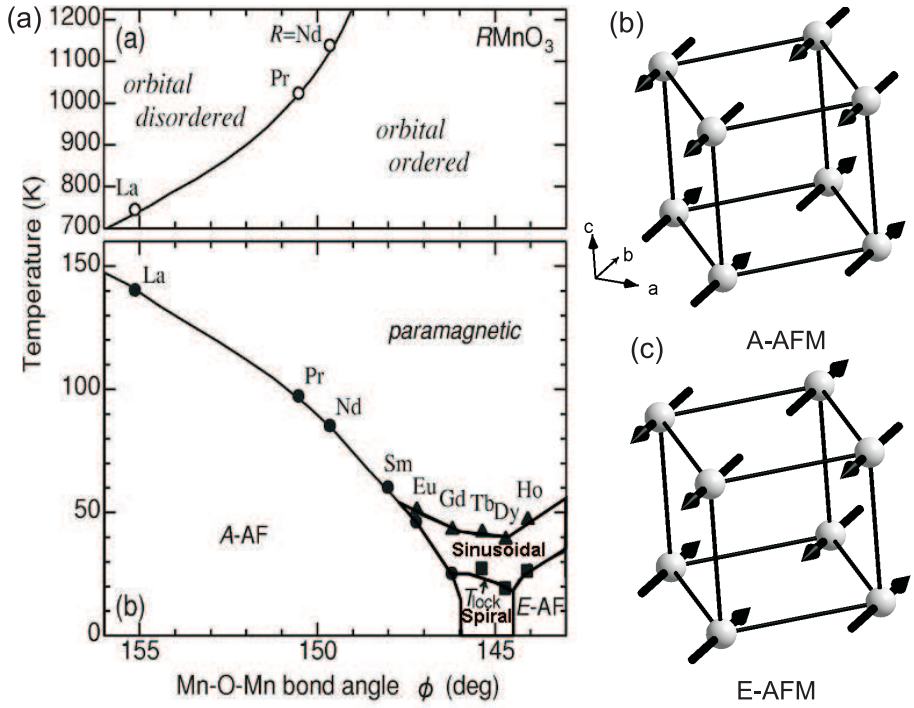

Figure 1.5: *(a) Magnetic phase diagram for orthorhombic rare earth manganites showing temperature as a function of the Mn-O-Mn bond angle. The figure is taken from [50]. $TbMnO_3$ lies in an intermediate region between the A-type (b) and E-type (c) antiferromagnetic magnetic structures. Moreover, the upper plot shows that all the rare earth manganites are orbitally ordered at room temperature.*

and E-type are schematically shown in figure 1.5 (b) and (c), respectively. At smaller ionic radii (not shown in the figure), the hexagonal crystallographic structure is more stable but it is outside the scope of this thesis. Moreover, the rare earth manganites $RMnO_3$ (from La to Ho) are all orbitally ordered at room temperature, because of the Jahn-Teller active Mn^{3+} ion with an increasing ordering temperature as the ionic radius is decreased [53]. The orbital ordering temperature for $TbMnO_3$ is of the order of 1500K [53].

The magnetic structure of $TbMnO_3$ has been exhaustively studied [40, 50, 54] and it is shown to display an incommensurate antiferromagnetic sinusoidal spin ordering below 40K. A transition to a non-collinear antiferromagnetic cycloid spin ordering along the b-direction follows below 27K (see figure 1.6). Phenomenologically, a way to generate the cycloidal phase is to consider that the ferromagnetic nearest-

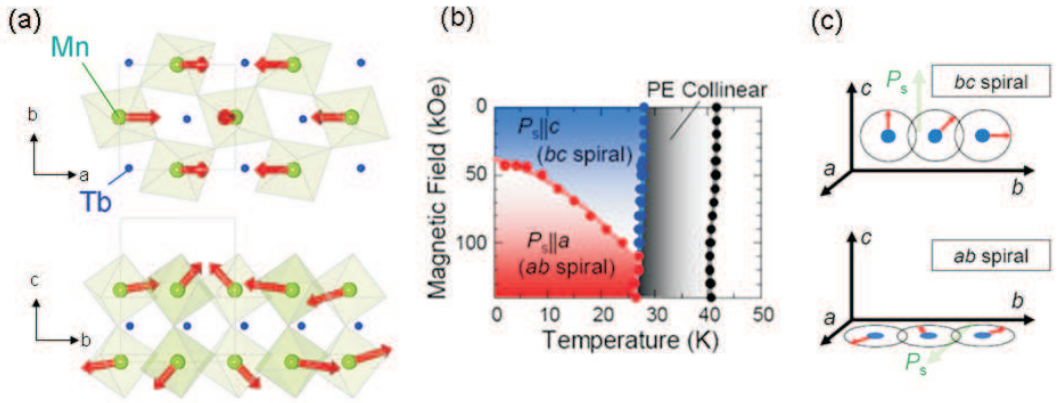

Figure 1.6: *(a) Magnetic structure of $TbMnO_3$ in the spin cycloid state. The spin cycloid is indicated by arrows and projected in the (a,b) plane (top panel) and (b,c) plane (bottom panel). (b) Applied magnetic field versus temperature phase diagram for $TbMnO_3$. (c) Schematic representation of the polarization flip transition under field. The figure is adapted from references [58, 59]*

neighbour (NN) superexchange is frustrated by a sufficiently strong antiferromagnetic next-nearest-neighbour (NNN) superexchange, allowing for the observed incommensurability of the magnetic structure with respect to the lattice periodicity [3]. This is the so-called J1-J2-J3 model, using classical spins, where J1 is the NN superexchange, J2 and J3 are the NNN superexchange along the a and b directions, respectively, as shown in figure 1.4 [55].

The cycloid phase requires the Lifshitz invariants in the Landau free energy [56]. Using Landau free energy, it has be shown that the cycloidal ordering breaks the inversion symmetry and allows for a polarization, perpendicular to both the wave vector ($\vec{q}$) and the spin rotation axis ($\vec{e_3}$) of the cycloid (P $\propto \vec{e_3}$x$\vec{q}$) [30, 40, 57]. In the case of $TbMnO_3$, the wave vector is along the b-axis and the spin rotation is around the a-axis, as shown in figure 1.6. Therefore, the experimentally observed polarization along the c-direction confirms the theory.

Microscopically, two possible mechanisms have been used to explain the appearance of the ferroelectric polarization at the cycloidal ordering: (a) An electronic contribution due to spin-orbit coupling [60, 61] and (b) a cation displacement due to the inverse Dzyaloshinskii-Moriya (DM) interaction (P $\propto \vec{D}.(\vec{S_i}x\vec{S_j})$) [62, 63]. Recently,

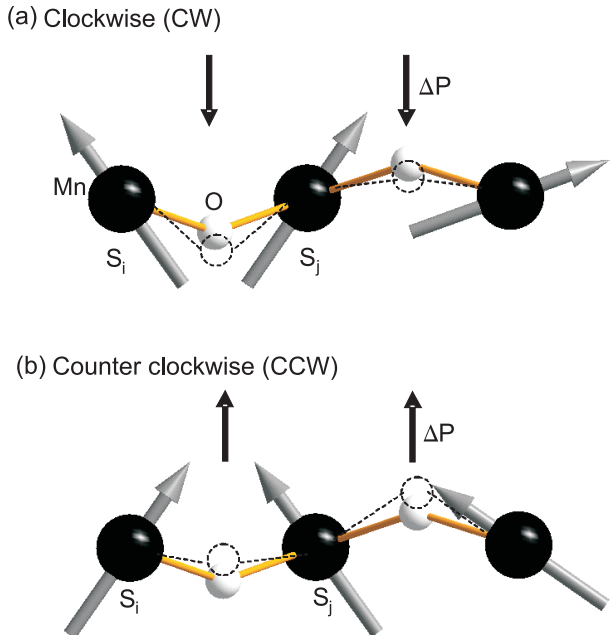

Figure 1.7: *(a) Schematic drawing of the local polarization in a clockwise cycloid (a) and in a counter-clockwise cycloid (b). The related local electric polarizations are shown as black arrows. The spins are indicated as grey arrows, whereas the manganese and oxygens atoms are represented by black and white spheres, respectively. The shifts of oxygen atoms, due to the spin canting of neighbouring atoms, are indicated as dashed lines. Figure adapted [69]*

however, it has been theoretically shown that the inverse effect of the Dzyaloshinskii-Moriya interaction [64,65], and its related atomic displacement, is the mechanism that explains the emergence of a net ferroelectric polarization in $TbMnO_3$ [66–68].

Indeed, the cycloidal arrangement of the spins induces an orientation of the local electric polarizations along the same direction, due to the inverse DM interaction, and allows for a net macroscopic polarization, as shown in figure 1.7 (a), for the case of a clockwise cycloidal. Moreover, it is also expected, that due to the asymmetric DM interaction $[(\vec{S_i}\mathrm{x}\vec{S_j})\text{=-}(\vec{S_j}\mathrm{x}\vec{S_i})]$, the polarization can be switched by time reversal of the cycloid, as shown in figure 1.7 (b) for a counter-clockwise cycloid. In the case of a cycloidal ordering, a strong coupling can be expected between the electric and magnetic orders, as they are associated with a single mechanism. Even though cycloidal spin structures and related polarizations usually appear at low temperatures, such systems are of special fundamental interest because of this large coupling be-

tween the magnetic and electric orders, and the fundamental challenges they pose. Indeed, it has been shown for $TbMnO_3$ that a field of around 5T along the a-direction flips the spin rotation axis and simultaneously the polarization, from the c-axis to the a-axis [54, 70](as shown in the phase diagram in figure 1.6(b) and sketched in figure 1.6(c)).

1.6 Manganites thin films

Studies of rare earth manganites ($RMnO_3$, R=rare earth ion) in thin film form started to be available only since 2006 and have been performed in various compositions for R changing from La to Ho. The most studied being $LaMnO_3$, due to its colossal magnetoresistance observed in bulk, upon doping by Sr or Ca. Only the multiferroic rare earth manganites close to $TbMnO_3$ (i.e. R = Gd, Ho, Y, Yb, Tb) will be discussed here. In particular, we focus on several reports that reveal induced or enhanced ferromagnetic interactions, which are absent in the bulk [71–80].

Among them, orthorhombic $HoMnO_3$ films of about 150nm [71] and 200nm [72] have been deposited on (001)-$SrTiO_3$ by pulsed laser deposition. In both cases, a split between the zero-field-cooled (ZFC) and the field-cooled (FC) of the magnetization-temperature curves is observed below the antiferromagnetic transition (occurring at the same temperature as the bulk) [71, 72]. In the work of J.G. Lin *et al.*, the ZFC-FC splitting was attributed to a field induced magnetization in the region of incommensurate to commensurate spin structure [72]. It is worth to note that two types of crystallographic domains were present in the films. T.H. Lin *et al.* suggested that the ZFC-FC splitting was due to weak ferromagnetism [71]. Although no clear statement is offered about its nature, two possible origins were discussed: One relates the weak ferromagnetism to spin canting and the other one to uncompensated spins at the boundaries of AFM domain walls [71], giving as example the weak ferromagnetism observed in AFM nanoparticles [71, 81]. These reports are very recent and the origin of the weak

ferromagnetism has yet to be confirmed.

Epitaxial stabilization of metastable structures is also possible. $YMnO_3$ was grown on $SrTiO_3$ with an orthorhombic (o-)structure by *X. Marti et al.* [73] by using pulsed laser deposition. A ZFC-FC hysteresis was also found below the antiferromagnetic ordering temperature, associated with a ferromagnetic response [73]. Roughness effects were suggested but experimentally discarded whereas the strain state (and specially the contraction of the b-axis) of the films was suggested as the likely origin [73]. Another report on o-$YMnO_3$ thin films grown on $SrTiO_3$ also showed a splitting between zero field cooled (ZFC) and field cooled (FC) curves below the antiferromagnetic transition [74]. The authors tentatively suggest that a strain-induced canted AFM state, for thin films, instead of the incommensurate to lock-in transition reported for bulk samples, is occurring [74]. Roughness effects were also suggested to account for the ferromagnetic interactions observed in the epitaxially grown thin films of o-$YbMnO_3$ [75].

When decreasing the ionic radius of the rare earth in bulk $RMnO_3$ compounds beyond R=Dy, the stable crystalline phase changes from orthorhombic to hexagonal [50]. Contrary to the orthorhombic phase, in which the ferroelectric ordering originates from the magnetically-induced lattice modulation, the ferroelectricty in hexagonal manganites arises from the tilting of the MnO_5 bipyramids [25]. Over the last few years, a wide variety of hexagonal/orthorhombic rare earth manganites (h-$RMnO_3$ have been grown in thin film form (including studies with R=Nd, Ho, Tm, Lu, Yb, Gd, Tb) [76–78, 80, 82]. However, hexagonal manganites under epitaxial strain are not the scope of this thesis.

The examples described above show that induced/enhanced magnetization was consistently reported for different manganite thin films in the last couple of years, a clear explanation has not been offered yet and a general origin for the induced ferromagnetism observed in epitaxially stabilized $RMnO_3$, specially those with similar ionic radii, cannot be discarded.

1.7 Outline of this thesis

This thesis addresses the role of strain on the multiferroic behaviour of orthorhombic rare earth manganites, focusing on $TbMnO_3$. As explained above, the structural distortion of the orthorhombic perovskite unit cell can lead to large modifications of the ferroelectric, magnetic and electronic properties of rare earth manganites. The advantage of the thin films is that they allow to change the crystallographic structure without modifying the cation on the rare earth site. This permits a detailed understanding of the relationships between the structure and the physical properties in thin film form. In particular, we have dedicated special effort to reveal the origin of the ZFC-FC hysteresis, observed in thin films of $TbMnO_3$ and that could be a more general effect of strain in orthorhombic manganites (see previous section). The ultimate goal is to try to tune the physical properties of the material using epitaxial strain, imposed by the substrate.

Although films of $TbMnO_3$ have been previouly grown by Cui *et. al.* [83–85], these were polycrystalline and not strained. Thin films of $TbMnO_3$ under epitaxial strain have been deposited in this thesis for the first time, using pulsed laser deposition on single crystals of (001)-oriented $SrTiO_3$ (after the publication of our results, a second, less exhaustive, report on epitaxially grown $TbMnO_3$ has been published by other authors [86]. Thin films of $TbMnO_3$ were also deposited on $SrRuO_3$ buffered (001)-oriented single crystals of $DyScO_3$ for the first time, during this thesis. Detailed structural, magnetic and dielectric characterization has been performed in order to answer the following main questions:

- What are the structural modifications by the strain induced from the substrate?
- How does strain affect the ferroic properties and the magnetoelectric coupling?
- Can the properties be systematically tuned by strain?
- What can we learn from the thin film behaviour of $TbMnO_3$ about the properties of multiferroics and manganites in general?

The thesis is organized as follows: Chapter 2 describes the experimental techniques used in this thesis. Chapter 3 presents the growth and a detailed structural characterization of $TbMnO_3$ thin films grown on $SrTiO_3$, using synchrotron and high resolution laboratory x-ray diffraction, as well as TEM. Chapter 4 describes the magnetic and electronic properties of the films, characterized using SQUID magnetometer and x-ray photoelectron spectroscopy; Chapter 5 reports the dielectric and magnetoelectric response of the $TbMnO_3$ thin films grown on $SrTiO_3$. Finally, Chapter 6 presents the growth and characterization of $TbMnO_3$ thin films on $SrRuO_3$ buffered $DyScO_3$ substrates. The chapters are designed such that they can be read independently.

Chapter 2

Experimental techniques

2.1 Pulsed laser deposition

Pulsed laser deposition (PLD) is a thin film growth technique by which a high power pulsed laser beam with short duration pulses hits a target with a certain laser energy density. The target is located inside a high vacuum chamber (with background pressures of 10^{-7} to 10^{-8} mbar) and a lens is placed just outside one of the optical ports of the chamber, to focus the laser close to the target. If the laser energy density is large enough, the material can be dissociated from the surface of the target and ablated away, with the same stoichiometry as that of the target. This process is called laser ablation. Contrary to the simplicity of the set-up, the interaction between the laser and the target is very complex [87] and out of the scope of this thesis. It is, however, important to emphasize that the laser energy density at the target is a crucial parameter, both to ensure a homogeneous ablation of the different species in the target, avoiding *preferential ablation* (or so-called incongruent deposition/ablation) [88] and to determine the deposition rate, the energy of the species arriving at the substrate surface and, thus, the growth mode.

The species ablated away from the target expand into the surrounding gas in the form of a plasma. The plasma forms a highly directional cloud (forward peaking phenomenon [89]) in front of the target (so-called 'plasma plume' due to its shape). The plume brings the species from the target onto a, typically, hot substrate (usually a single crystal). This is performed with a background gas, such as oxygen in the case of

oxides growth, at pressures of pO_2=0.01-1mbar. In the case of non-volatile species, and when the energy threshold for ablation of all the target species is reached, there is a very good stoichiometric transfer from the target to the substrate. This is one of the main advantages of PLD with respect to other thin film deposition techniques, specially for the growth of complex materials. Moreover, because of the plasma phase involved in the process, having the proper stoichiometry and a proper homogeneity of the target is important, but there is no need for phase-pure targets or targets with the crystal structure intended for the film, which can be difficult or impossible to achieve by standard synthesis techniques.

The next process occurring during pulsed laser deposition is the transition from a plasma phase to a solid (crystalline) phase at the surface of the substrate. This process can be compared to the supersaturation that takes place between the vapour and the solid phase of a material during crystallization. In the case of pulsed laser deposition, growth takes place far from the dynamical equilibrium conditions and the difference in chemical potentials between the plasma and the solid phase is also the thermodynamic force to trigger crystallization [90]. Supersaturation is thus crucial for determining the type of growth [90]. The different types of growth will be described in the section 1.2.2.

Our PLD setup allows for scanning the target in the vertical and horizontal directions during deposition to improve the homogeneity of the ablated area. The growth of multilayers is also possible thanks to a multi-target holder, which can hold up to 5 different targets. In practice, many other intercorrelated parameters should be taken into account in the optimization of the growth: The temperature of the substrate, the background pressure and type of gas (pure gas of mix of gases), the frequency of the pulses, the distance from the surface of the target to the surface of the substrate and the spot size on the target (the area defined by the defocused laser spot, and whose shape and homogeneity is controlled by a mask). Figure 2.1 shows a sketch of the vacuum chamber used in this thesis. Apart from the standard elements described above, the PLD system used in this thesis includes a Reflective High Energy Electron Diffrac-

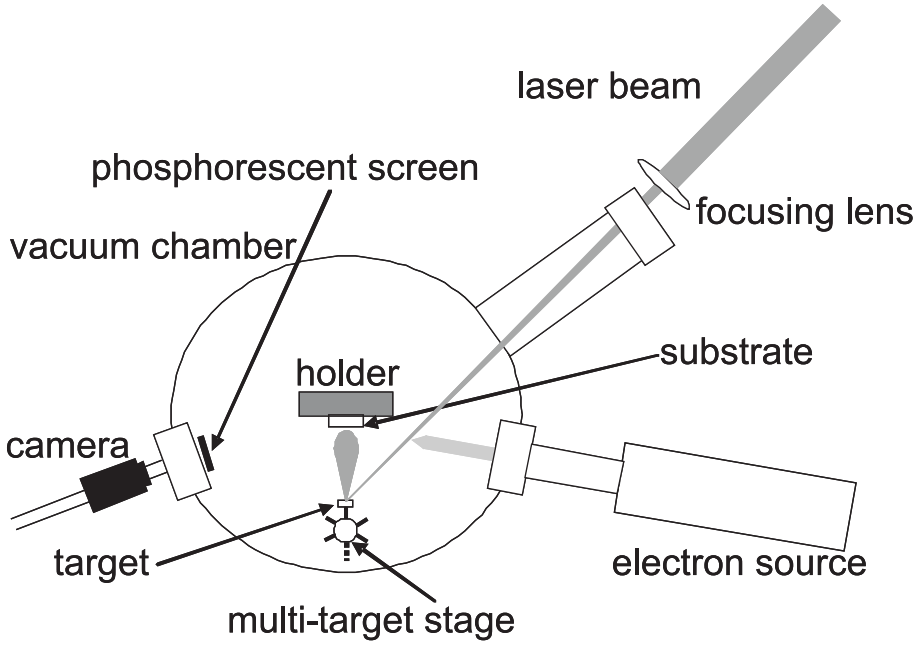

Figure 2.1: *Top view of the PLD deposition chamber set-up of the Zernike Institute for Advanced Materials, University of Groningen.*

tion (RHEED) set-up, specifically designed for PLD by Twente Solid State Technology B.V. [91].

RHEED is, in principle, incompatible with PLD because of the high pressure needed during growth (up to 1 mbar), which gives rise to a large scattering of the electrons before they reach the phosphorescent screen and, thus, a too low intensity collected by the CCD camera (see figure 2.1). To avoid this problem, the group of Prof. Blank in Twente (The Netherlands) added an extension to a standard RHEED-gun, consisting of a tube that goes from the gun to the substrate [91]. The electron gun and the tube are then differentially pumped with respect to the main chamber, to minimize the scattering along the incident electron path and, at the same time, avoid the breaking of the filament of the gun due to the high pressures. Moreover, the chamber is designed to keep a minimum distance between the substrate and the screen [91]. Under these conditions, RHEED-assisted PLD is possible although the alignment is more difficult than that used in Molecular Beam Epitaxy set-ups, due to the small size of the hole at the end of the tube.

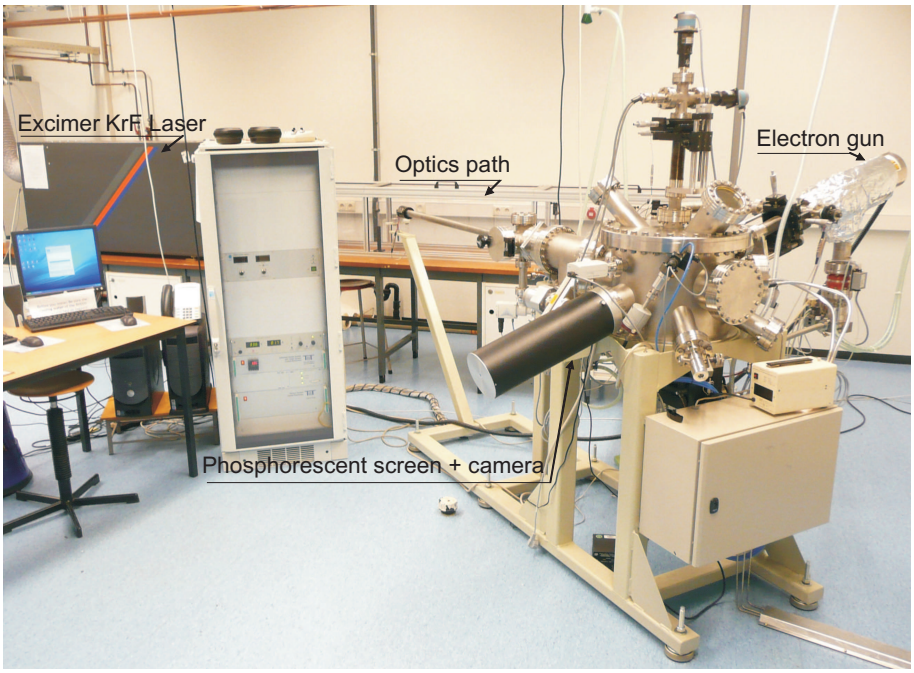

Figure 2.2: *Picture of the pulsed laser deposition system at the Zernike Institute for Advanced Materials, University of Groningen, used to in this thesis.*

Figure 2.2 shows the PLD system at the Zernike Institute for Advanced Materials, University of Groningen, used to grow the samples discussed in this thesis. The small pump used for the differential pumping of the electron path can be seen on the picture hanging below the electron gun. The laser is a Lambda PhysiK COMPex Pro 205 KrF excimer laser (λ=248nm), providing pulses of about 25ns. The long optics path is designed to achieve the laser energy densities typically needed at the target position (1-5 J/cm^2), using a limited range of laser voltages (19kV-26kV). In this thesis, the changes in laser energy density are obtained by changing the voltage of the laser to keep a constant spot size at the target while a fixed mask is used to select the central, most homogeneous part of the laser beam. Finally, to ensure reproducibility, the laser was refilled with new gases when the voltage required for a chosen laser energy density was too high with respect to the above mentioned conditions.

Pulsed Laser Deposition has advantages with respect to other physical deposition techniques [92]. First, PLD is an experimentally simple deposition technique, attractive for fundamental research. Moreover, it is a versatile technique which allows the

deposition of many different types of materials in various gases and various pressures. This wide range of background gas parameters makes the PLD unique because it can be used to modify the growth mode, changing the kinetic energy of the ablated particles by interaction with the background gases [92]. It is a fast process that allows the growth of high quality samples in short deposition times. Moreover, because of the very short duration of a pulse, the deposition can be regarded as instantaneous with annealing between pulses, which is advantageous for the study of growth kinetics [92]. A laser can be used along with more than one UHV chamber, making the use of PLD cost-efficient. A major drawback of this deposition technique is the scalability. Indeed, the area deposited is small compared to many other deposition techniques, making PLD difficult for large scale purposes.

2.2 Reflective high energy electron diffraction (RHEED)

2.2.1 RHEED set-up

In RHEED, an electron beam hits the surface of a crystalline sample at a grazing angle (typically below 3^o). The grazing angle provides surface sensitivity and allows to use electron diffraction in-situ during growth, with minimum interference between the electron beam and the plume. Because of this, RHEED is a very common technique for monitoring the growth of thin films, in particular for those processes using low background pressures, such as Molecular Beam Epitaxy [93]. Although, as explained in the previous section, RHEED-assisted PLD is also becoming very popular.

A RHEED set-up requires two rotation circles in order to modify the sample azimuth and the incident angle (see figure 2.3(a)). Qualitative information of the RHEED patterns can be extracted from a simple kinematical diffraction model. Most of the incident electrons are elastically scattered by the atoms at the first few atomic planes below the surface of the sample and a diffraction pattern forms at the phosphorescent screen. Moreover, the electrons are also scattered multiple times. Therefore, contrary

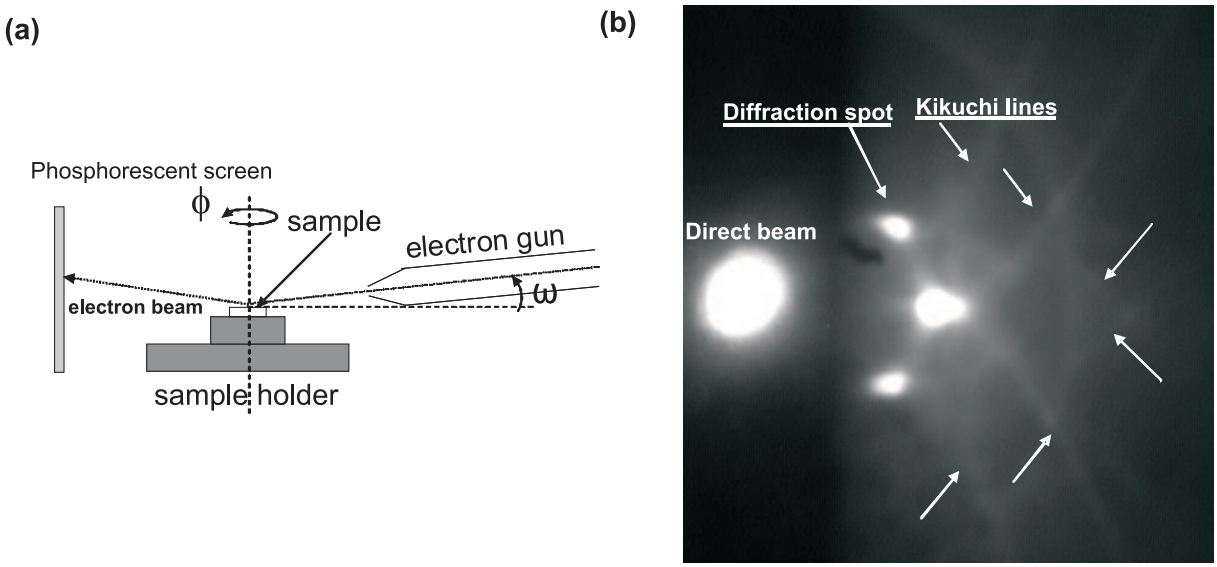

Figure 2.3: *(a) Sketch of a RHEED set-up, where the azimuth (ϕ) and tilt (ω) angles are shown. (b) RHEED pattern showing Kikuchi lines. The picture was taken for an TiO_2-terminated (001)-oriented $SrTiO_3$ substrate with a miscut of $\approx 0.1^o$ under an acceleration voltage of 28kV in a vacuum of the order of 10^{-6}mbar and at room temperature.*

to x-ray diffraction, the dynamical theory of electron diffraction must be used for a full interpretation of the patterns. The inelastically scattered electrons contribute to the diffuse background. This being enhanced with increasing partial oxygen pressure in the chamber. Moreover, the multiple inelastic scattering of electrons can give rise to cones of intensity that can, in turn, be diffracted by the sample and form the so-called Kikuchi lines [94]. Kikuchi lines are often found in RHEED patterns from surfaces of high quality (see figure 2.3 (b)).

The reciprocal space associated with the 2D lattice of a perfect crystal surface, consists of infinite rods perpendicular to the surface of the sample and passing through the 2D lattice points (also called crystal truncation rods or CTRs), due to the relaxation of the third Laue condition [95]. So a RHEED pattern will then be determined by the intersection of the rods with the Ewald's sphere, whose radius is inversely proportional to the wavelength of the incoming electron beam [95]. If the surface is perfectly flat, the reciprocal rods have no width and this intersection gives rise to a pattern of spots aligned along semicircles (Laue circles), as schematically shown in figure 2.4 (a).

In a RHEED pattern during PLD, in practice, only the low order diffraction spots (so called '0^{th} Laue circle') can be seen under proper conditions of tilt (ω) and azimuth (ϕ) (ω_1 in figure 2.4 (a)). By changing the tilt angle of the sample, higher order diffraction spots can be accessed, as shown in figure 2.4 (a). Moreover, as shown schematically and illustrated by an example (TiO_2-terminated (001)-oriented $SrTiO_3$ single crystal) in figure 2.4 (b), rotating the sample around the azimuth allows access to different planes and gives extra information about the structure of the surface .

If the surface has a roughness of the order of one monolayer, the reciprocal rods are broaden and their intersection with the Ewald's sphere gives rise to streaks (see figure 2.5 (a)). In practice, the observation of spots or streaks for an atomically flat surface also depends on the set-up (mainly, the wavelength of the electrons that determines the radius of the Ewald's sphere). When using RHEED to monitor the growth, we call both these patterns '2D-patterns', because they reflect an atomically flat surface.

Moreover, the tilting of the CTRs can give information about the step-terraces structure of the surface of a substrate (the length of the terraces being determined by the miscut angle), and/or possible tilt distortion of the growing film with respect to the substrate, as shown in figure 2.5 (b) and illustrated for the case of a 10nm $BiFeO_3$ film grown on $SrTiO_3$. If the roughness of the surface is increased, such as during three-dimensional (island) growth, electron transmission across islands can take place and the RHEED pattern consists of a 3D net of spots, which are not arranged along a semi-circle, as in a standard diffraction pattern (see figure 2.5 (c)).

2.2.2 Growth monitoring

Since the intensities of the individual spots on the RHEED patterns change according to the surface coverage and roughness, we can use these changes to follow the thin film growth. Generally speaking, the relative values of the free energies of the surface of the substrate, the surface of the film and the interface between the substrate and the film, determine the nucleation of the arriving species and the wetting of the substrate by

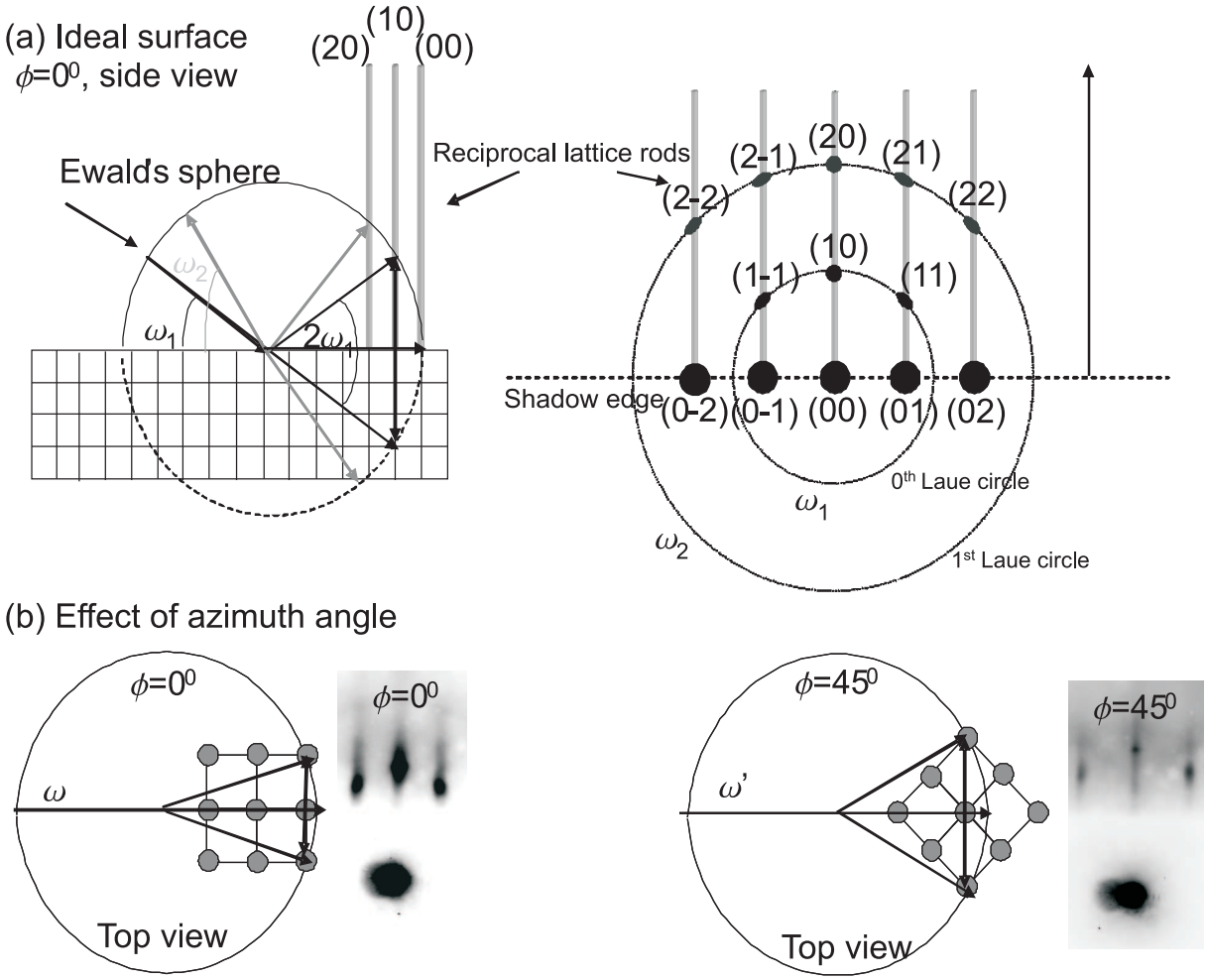

Figure 2.4: *(a) Side view of a schematic representation of the intersection of the Ewald's sphere with the reciprocal lattice rods in the case of an ideal surface (left panel). The drawing represents the RHEED pattern for the electron beam oriented along the [100] direction. The reciprocal lattice rods, perpendicular to the surface, are labelled by their respective Miller indexes (h,k). The view on the right panel is the projection on the phosphorescent screen. (b) The left panel shows a schematic top view of (a), along with an illustration of a TiO_2-terminated (001)-oriented $SrTiO_3$ substrate with a miscut of ≈0.08^o under an acceleration voltage of 28kV in a vacuum of the order of 10^{-6}mbar and at room temperature. The right panel shows the effect of rotating the substrate by ϕ=45^o (see ϕ angle in figure 2.3) of the same sample as shown on the left panel, highlighting the (110) planes.*

the film [87]. For low supersaturation (not too far from thermodynamic equilibrium), three different growth modes have been defined: If the total free energy of the film plus the interface is larger than the free energy of the substrate surface, the arriving species will tend to form islands on the substrate (figure 2.6(a)-(b)-(c)). This type of growth

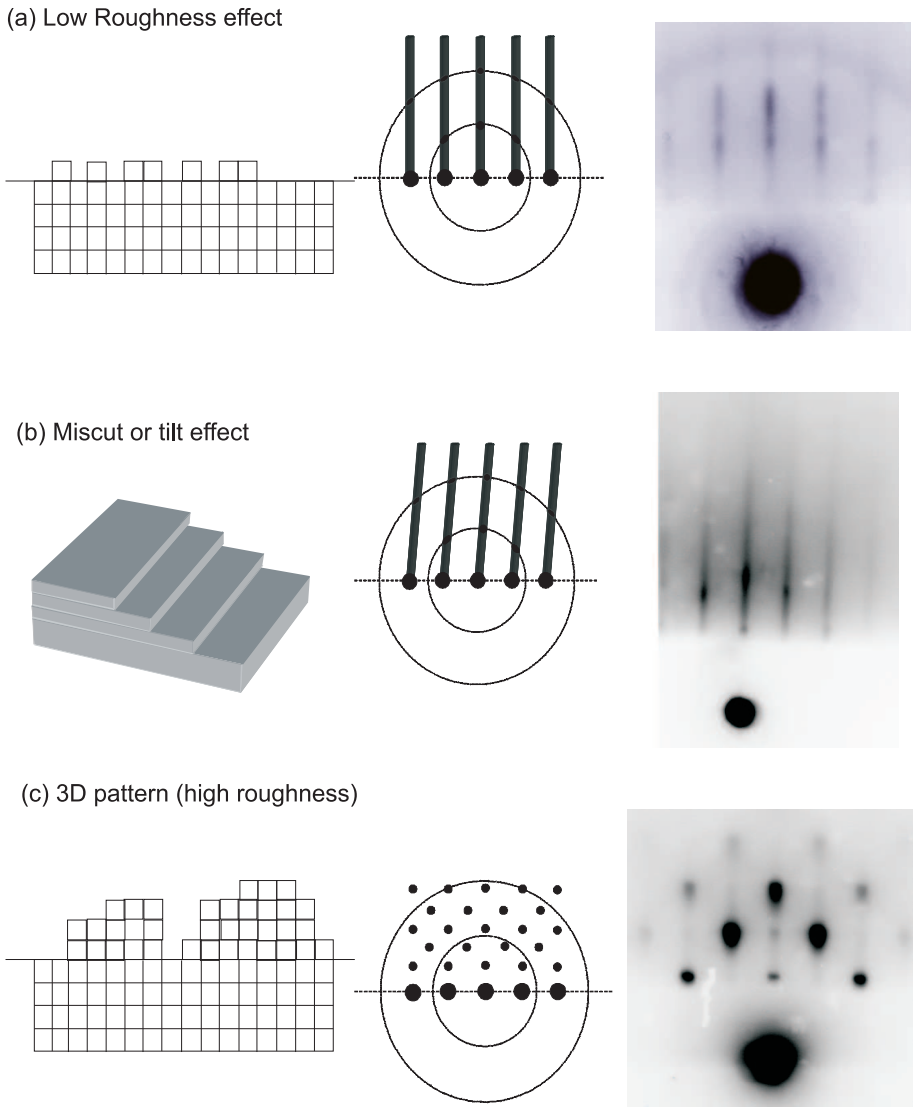

Figure 2.5: *(a) Schematic representation of the effect of low roughness, of the order of one monolayer, on the RHEED pattern. A picture, seen on the right panel, has been added to illustrate this effect. The picture was taken along the [100] direction of $SrTiO_3$ for a 20nm $BiFeO_3$ film. (b) Effect of miscut or film tilt on the crystal truncation rods. The picture to illustrate the effect, on the right panel was recorded in vacuum for a 10nm $BiFeO_3$ film on a $SrTiO_3$ having an overall tilt of the order of 0.2^o with respect to the lattice planes of the substrate. (c) Schematic representation of the effect of a rough surface, leading to transmission through the three dimensional 'islands'. This is also illustrated for the case of a $SrTiO_3$ film grown on $SrTiO_3$ with a RMS roughness of the order of 1nm (3-4 unit cells).*

mode is seen as a sharp decrease of the RHEED intensity and a '3D' RHEED pattern of spots (see previous subsection). It is referred as 3D growth or Volmer-Weber growth.

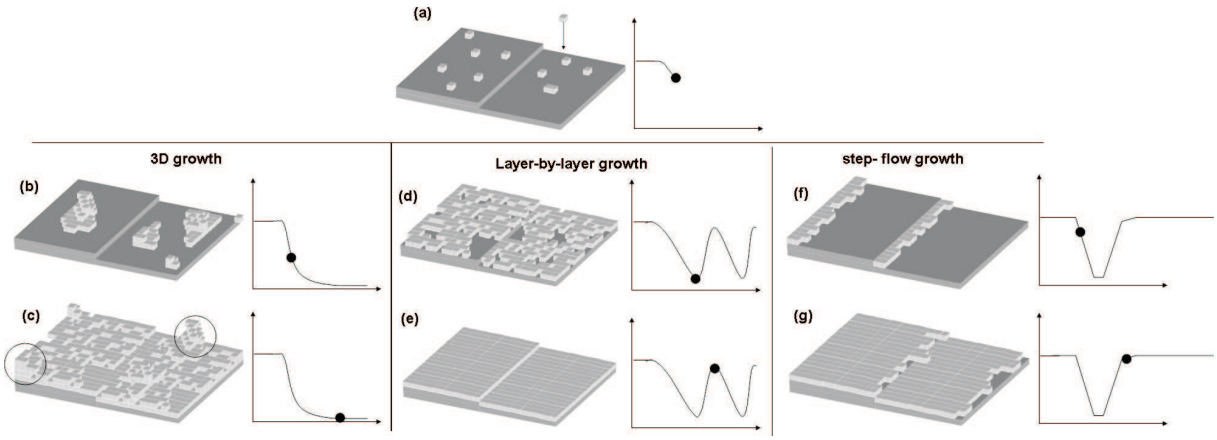

Figure 2.6: *Typical modes observed in thin film growth close to thermodynamic equilibrium and the corresponding evolutions of the RHEED intensity. (a) Arrival of species at the substrate. (b)-(c) 3D island growth (Volmer-Weber). (d)-(e) 2D layer-by-layer growth (Frank-Van der Merwe). (f)-(g) 2D step-flow mode.*

For total free energies of film plus interface equal to or smaller than the free energy of the substrate surface, the film will wet the substrate, leading to 2D layer-by-layer growth (figure 2.6(a)-(d)-(e)). This mode is seen as RHEED oscillations that keep the same amplitude with time. This type of growth is also known as Frank-Van der Merwe growth. The intermediate mode is also frequently observed in heteroepitaxy: After a few monolayers, the interfacial energies lead to a decrease of the wetting and the growth switches from 2D to 3D mode. This can be seen by RHEED oscillations whose maxima decreases as the thickness increases until the oscillations fade away. The final RHEED pattern also usually displays 3D-like spots (i.e. not aligned on a Laue circle). This type of growth is known as Stranski-Krastanov growth (not shown in the figure).

The misfit strain between the film and the substrate, specially at high misfit values, can modify considerably the growth modes during deposition. Indeed, the first monolayers are heavily strained on the substrate so that their chemical potential is considerably modified with respect to that of the bulk. The chemical potential of the film is then thickness (t) dependent ($\mu(t)$), approaching the bulk value as the thickness increases [90].

Moreover, in PLD, supersaturation is large and the growth takes place far from ther-

modynamic equilibrium. Limited diffusion creates different growth modes than those explained above and other parameters, such as the miscut angle of the substrate, become important. The presence of a miscut angle (substrate steps) and large supersaturation can give rise to the step-flow mode (2.6(a),(f),(g))). In this case, after a first decrease and further increase of the RHEED intensity, no RHEED oscillations are observed because the film morphology does not change during growth. The steps can rapidly move over the surface with different velocities leading to step bunching and an atomically flat surface with few steps, for high enough thicknesses. In this case, very high quality films can be grown but no layer-by-layer control is possible.

2.3 X-ray diffraction (XRD)

2.3.1 Crystal truncation rods and specular scans

In the case of an infinite three-dimensional crystal, the x-ray diffracted intensity is proportional to a delta function for allowed values of integers (h,k,l), giving rise to spots in a diffraction pattern. However, for a cleaved crystal such as a substrate, a relaxation of these conditions occurs perpendicular to the cleavage direction and streaks of scattering appear, along this direction [95]. A crystal with a perfect surface can be mathematically expressed as the multiplication of the electron density of the bulk crystal, ρ(z), with z being the normal to the cleavage plane, with a step function, h(z). The scattered amplitude is then proportional to the convolution of the fourier transforms of $\rho(z)$ and h(z). The fourier transform of the electron density being a delta function whereas the fourier transform of the step function is proportional to the inverse of the wavevector along the direction perpendicular to the cleavage direction [95]. In practice, the use of typical $2\theta - \omega$ scans (where 2θ and ω are, respectively, the angles that the detector and the sample form with the incident beam) allows to monitor the profile of intensity along the CTRs in the (00L) direction, which is proportional to the square of the inverse of the wavevector [95]. When a film is grown on a perfect substrate surface and

the film is thin enough, the x-rays can penetrate through the film and the interference effects from reflections at the surface and the interface with the substrate, produce fringes (Laue fringes) in the CTRs, whose periodicity can be related to the thickness of the film.

2.3.2 Reciprocal space mapping

In addition to the structural information that can be extracted from standard $2\theta - \omega$ scans, the epitaxial relationships between film and substrate can be investigated by mapping different areas of the reciprocal space, in particular, around non-specular Bragg peaks. This is done by performing series of 2θ-ω scans (radial scans) for different ω angles. Figure 2.7 shows a sketch of the reciprocal space mapping principle. The radial (2θ-ω) scans change the length of the scattering vector ,ΔK, while keeping its direction, whereas the ω scans keep the length constant but change the direction of the scattering vector.

The recorded angles (θ,ω) are then transformed to reciprocal units ($K_{\perp}$,$K_{\|}$) using the simple following relationships: $K_{\perp}$= ΔK.cosδ and K$\|$= ΔK.sinδ, where δ=θ-ω is called the *offset* and ΔK= 2 k_{in}.sinθ.

2.3.3 Grazing incidence diffraction

When characterizing the structure of the films, standard diffraction geometries have limited use. As explained above, in the standard Bragg-Brentano geometry, the finite thickness of the films gives rise to Laue oscillations along the crystal truncation rods [95] that limit the resolution in the direction perpendicular to the surface. Although, as shown in the previous section, information about the in-plane structure can be obtained in this geometry, the small volumes of material involved in the scattering event leads to a considerable reduction of the diffracted intensities. In addition, the much more intense substrate peaks often hide the film reflections.

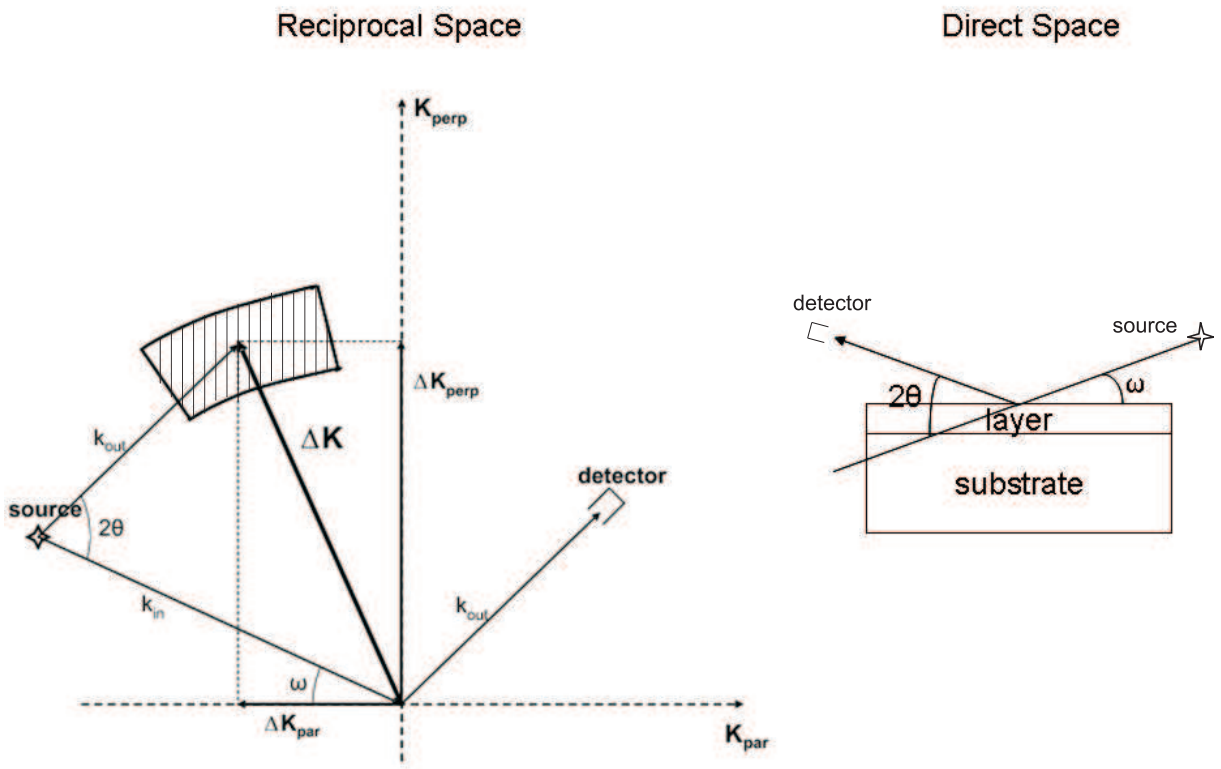

Figure 2.7: *Reciprocal space mapping using x-ray diffraction. The control of the motion of the sample and the detector allows the spanning of the shaded area. The collected data are plotted in a 2D contour plot, where the horizontal and vertical axes correspond to K_{par} and K_{perp}, respectively.*

In order to have access to the in-plane structure of the films with scattering vectors fully contained in the plane (and, therefore, be insensitive to the finite thickness of the films and the presence of the substrate), grazing incidence x-ray diffraction (GIXD) is performed. The setup for GIXD is plotted in figure 2.8. The wave k_{in} is incident on the surface at a very small angle θ_0, just below critical angle for total reflection, which is about 0.2-0.3^o for most materials. In total reflection conditions, with the absence of wavevectors propagating perpendicular to the surface, an evanescent wave is produced, which is only significant close to the surface and decays exponentially into the films. This evanescent wave is able to scatter with the in-plane lattice planes. If the sample is rotated around its surface normal, thus preserving the small angle θ_0, the wave k_{in} can fulfill the Bragg condition with some atomic planes perpendicular to the

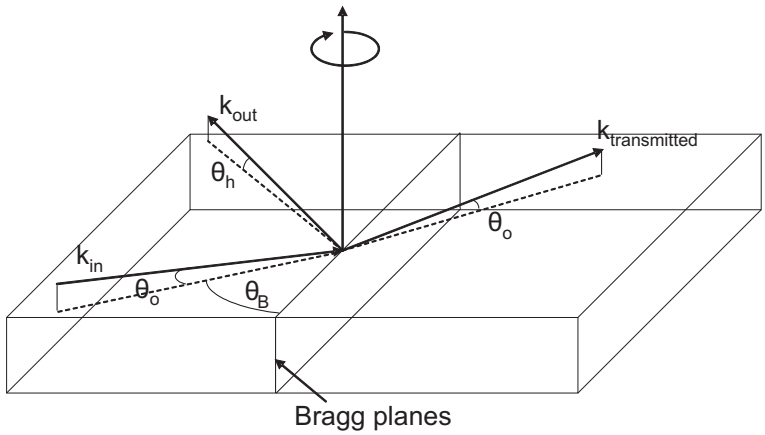

Figure 2.8: *Grazing incidence diffraction geometry.*

surface at some angle θ_B, giving rise to the diffracted wave, k_{out}.

GIXD also allows to perform depth dependence measurement by tuning of the incident angle θ_o [95]. Another advantage of GIXD is that, due to the small penetration depth of the evanescent wave, the substrate peak is not seen. The disadvantage of this technique is that it requires specific motion of the detector and the sample stage that are not available in many diffractometers. Moreover, since the evanescent wave is very weak, and the incident angle needs to be well defined, it requires the large intensities and highly collimated beams of synchrotron sources. The GIXD experiments in this thesis were performed at HaSyLab (DESY, Hamburg) on the beam line W1 and at the ESRF (Grenoble, France) on the beam line BM28.

2.4 X-ray photoelectron spectroscopy (XPS)

X-Ray Photoelectron spectroscopy allows the chemical analysis of surfaces by gathering information of the elemental composition, valence and electronic states. XPS requires ultra-high vacuum (UHV) conditions (typically 10^{-9}-10^{-10} mbar). XPS spectra are obtained by irradiating the material with a beam of monochromatised x-ray photons produced from aluminum or magnesium sources. Electrons, within a depth of a few nanometers, can absorb the x-rays and leave the material with a characteristic ki-

netic energy, directly related to their binding energy ($E_{binding}$). A typical XPS spectrum is a plot of the number of electrons arriving at the detector as a function of the binding energy of the collected electrons. $E_{binding}$ of each emitted electron can be calculated by: $E_{binding} = E_{photon} - E_{kinetic} - \Phi_{sp}$, where E_{photon} is the energy of the absorbed x-rays, $E_{kinetic}$ is the kinetic energy of the emitted electron, as measured by the analyzer, and Φ_{sp} is the work function of the spectrometer, taking into account the difference of kinetic energy seen at the detector with respect to the kinetic energy seen at the sample. These characteristic peaks, or binding energies, identify the atoms present at the surface and their electronic configuration. Moreover, XPS is a non-destructive technique that can measure the surface chemistry of any material and is not restricted to crystals. The measurements using this technique have been performed in a SSX-100 (Surface Science Instruments) photoemission spectrometer, with a monochromatic Al Kα X-ray source (hν=1486.6 eV, base pressure during measurement: 10^{-10} mbar), belonging to the Surfaces and Thin films research group at the Zernike Institute for Advanced Materials.

2.5 Atomic force microscopy (AFM)

The Atomic Force Microscope (AFM) consists of a microscale cantilever with a sharp tip at its end that is used to scan a sample surface. The cantilever is typically silicon or silicon nitride with a tip radius on the order of 10 nanometers. When the tip is approached to the sample surface, forces between the tip and the sample lead to a deflection of the cantilever. Typically, the deflection of the cantilever is measured by detecting the movements of a laser spot that is reflected from the top of the cantilever into an array of photodiodes.

The AFM can be operated in a number of modes, depending on the application, but most of the AFM images presented in this thesis were performed using the AFM in tapping mode, which is more gentle on the sample and the tip than the contact mode.

In tapping mode, the cantilever vibrates with a frequency close to its resonance frequency. The amplitude of this oscillation is typically 100 nm. Due to forces acting on the cantilever when the tip is approaching the surface, the amplitude of the vibration decreases. The height of the cantilever is modified by the system electronics using a piezoelectric actuator, in such a way that a constant amplitude of the cantilever vibrations is kept during the scanning of the surface by the AFM tip. Tracking the cantilever height results in a map of the area that represents the topography of the sample.

2.6 Magnetization measurements

The measurements of the magnetization of the thin films produced in this thesis were performed using a Quantum Design Magnetic Property Measurement System MPMS7. The (MPMS) is composed of a liquid-helium cooled SQUID (Superconducting QUantum Interference Device) that measures the changes in the magnetic flux as the sample moves through a superconducting detection coil. This device acts as a very sensitive magnetometer, since it can detect changes as small as one flux quantum. The MPMS system at the Zernike Institute for Advanced Materials, used in this thesis, allows the measurement of the magnetic properties from around 2K up to 400K under magnetic fields up to $\pm$7T. The sensitivity of the measurement is 10^{-6}-10^{-8} emu, depending on the setup. However, despite this high sensitivity, measurements on non-ferromagnetic ultra-thin films (below 50nm) are very difficult, as the signal from the layer can be below the sensitivity value and the signal of the substrate may mask that of the film.

The samples are inserted in the device by placing them inside a plastic straw (with a low diamagnetic signal) that is attached to the end of the MPMS probe. Most of the measurements presented here are done after zero-field-cooling (ZFC) and field-cooling (FC) conditions. For ZFC, the sample is cooled down below its transition temperature under no applied field. A field is then applied at the lowest temperature and

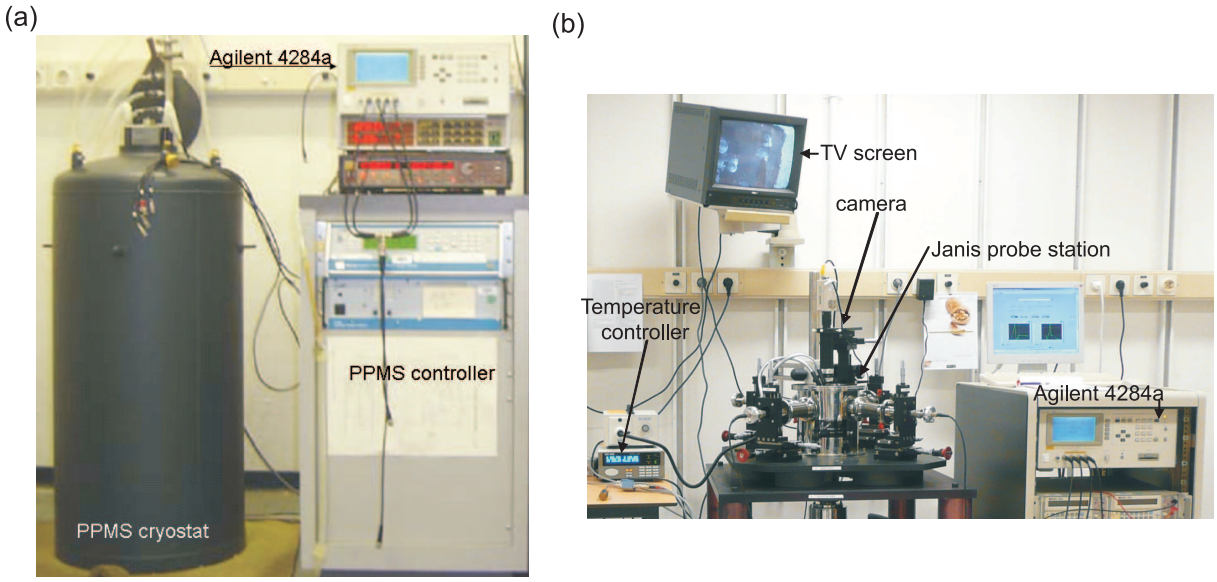

Figure 2.9: *Pictures of the Quantum Design PPMS system (a) and the Janis probe station (b) used to perform the dielectric measurements.*

the sample is measured upon heating. For the FC measurements, the sample is cooled down through the transition under an applied magnetic field. At the lowest temperature, the field applied during cooling is removed and the same field as used in the ZFC measurement is then applied while the sample magnetization is measured upon heating.

2.7 Dielectric measurements

Measurements of the capacitance and the dielectric loss of a material give valuable information about phase transitions and conduction processes in a dielectric [96]. However, these measurements are not so often performed due to issues distinguishing intrinsic and extrinsic behaviour. This is specially difficult in thin films, where leakage currents and interface effects can be important. In this thesis we show the usefulness of this technique when properly applied.

The capacitance and the loss of a dielectric sandwiched in between two parallel electrodes can be written as C=$\epsilon_o \epsilon' \frac{A}{d}$ and $\tan(\delta)=\frac{\epsilon''}{\epsilon'}$, where ϵ_o is the permittivity of free

space, ϵ' and ϵ'' are the real part and imaginary part of the dielectric permittivity of the material, A is the area of the electrodes and d is the thickness of the sample. Peter Debye developed a model of dielectric relaxation by considering a delay of the response of a dipole under an alternating electric field due to a surrounding viscous medium [97]. According to this model:

$$\epsilon(\omega) = \epsilon_\infty + \frac{\epsilon_s - \epsilon_\infty}{1 + j\omega\tau} \tag{2.1}$$

where τ is the relaxation time associated with the orientation process, ϵ_s is the static permittivity (zero frequency limit), ϵ_∞ is the permittivity at optical frequencies, τ is the relaxation time and ω is the (angular) frequency of the applied electric field. By separating the real part from the imaginary part in the Debye equation, one obtains:

$$\epsilon'(\omega) = \epsilon_\infty + \frac{\epsilon_s - \epsilon_\infty}{1 + (\omega\tau)^2}, \epsilon''(\omega) = \frac{\omega\tau(\epsilon_s - \epsilon_\infty)}{1 + (\omega\tau)^2} \tag{2.2}$$

This implies that in a Debye-like relaxation, ϵ' and ϵ'' show a step and a peak, respectively, at the relaxation frequency, τ^{-1}.

Using impedance spectroscopy, the evaluation of different electrical functions (impedance Z, admittance Y and modulus M) is possible. These are defined as: $M = \epsilon^{-1}$; $Z = (j\omega C_o\epsilon)^{-1}$; $Y = j\omega C_o\epsilon$, where C_o is the capacitance of an empty cell with the same dimension as the sample. The frequency behavior at a given temperature of the impedance functions is often used to determine the equivalent circuit of a material [96] and separate the intrinsic and extrinsic dielectric behavior.

A home-built sample holder was used to measure the dielectric properties of the thin films placed in a Quantum Design Physical Properties Measurement System, or PPMS, (see figure 2.9(a)). The PPMS was used to carry out temperature or magnetic field dependence on the dielectric properties. Bottom and top contacts were deposited using pulsed laser deposition and the details about the growth of the electrode will

be given in chapter 4. Pt wires were connected to the top electrodes by using a two-component silver epoxy. The other end of the Pt wire was soldered to the sample holder contacts. Dielectric measurements were performed using an LCR Meter (Agilent 4284a) for frequencies between 20Hz and 1MHz, and under an applied ac voltage of 50 mV.

The results presented in chapter 6 of this thesis were performed with the sample placed inside a Janis probe station that allows 2 and 4 points measurements (see figure 2.9(b)). The system can be cryogenically cooled down to 10K. The capacitance measurements were performed using the same Agilent LCR Meter, as in previous experiments. The sample preparation differs slightly from the one used for the PPMS: The thin films with $SrRuO_3$ electrodes were glued on a thin glass sheet using wax, and a two-component silver glue was deposited on the top electrodes, keeping the added silver within the perimeter of the electrodes.

Chapter 3

$TbMnO_3$ thin films on (001)-$SrTiO_3$: growth and structure.

3.1 Abstract

In this chapter, we present the growth and structural characterization of $TbMnO_3$ thin films on (001)-oriented $SrTiO_3$ single crystals. (001)-$SrTiO_3$ is preferred in studies of epitaxy in perovskites because it can be obtained with atomically flat surfaces, favoring high quality growth. The films are shown to be very flat, c-oriented and compressively strained. Their unit cell is orthorhombic with an orthorhombic distortion that can be tuned with the film thickness up to a thickness of about 50nm. A fine domain microstructure has been revealed by synchrotron x-ray diffraction and transmission electron microscopy, showing an increasing number of orthorhombic domains as the thickness is decreased. Additionally, we show that the density of domain walls follows a linear dependence with the inverse of thickness.

3.2 Substrate treatment

Prior to deposition, the single crystals of $SrTiO_3$ (with size 5x5x0.5mm^3) were chemically and thermally treated in order to obtain high quality surfaces, following the procedure reported in reference [98]. Figure 3.1(a) shows the AFM image of an as-received $SrTiO_3$ substrate. Although a steps and terraces structure is clearly visible and the ter-

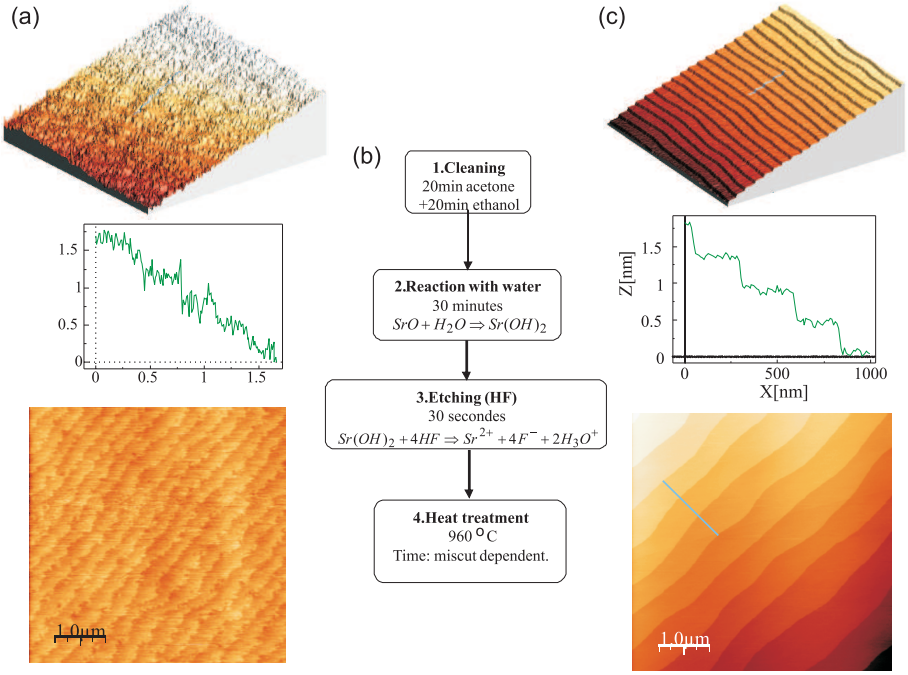

Figure 3.1: *(a) Typical AFM topography image of an as-received (001)-oriented $SrTiO_3$ substrate. (b) Procedure elaborated by ref. [98] to obtain high quality substrate surfaces. (c) AFM topography image for a TiO_2-terminated (001)-$SrTiO_3$ substrate. (d) Profile along the line seen in (c). The 4Å steps are clearly visible and the flatness of the terraces is evidenced.*

races are regularly spaced, the terraces edges are not straight. Moreover, the steps are not one unit cell high (4 Å), indicating that different terminations (SrO or TiO_2 planes) are present in the as-received substrates.

As shown in figure 3.1(b), the treatment procedure includes, first, the cleaning of the substrates with acetone and ethanol. The substrates are then put into water so that a chemical reaction between SrO and H_2O can occur, forming strontium hydroxide ($Sr(OH)_2$). The strontium hydroxide is then dissolved in a commercial solution of mixed ammonium fluoride (NH_4F, 87.5%) and ammonium hydrogen difluoride ($(NH_4)HF_2$, 12.5%) during a short time of 30s, enough to dissolve the strontium hydroxide without attacking the surface of the substrate and creating holes (so called 'etch pits'). At this point, the substrates are TiO_2 terminated and present steps of 4$\mathring{A}$. The final step is to induce a thermal motion of the adatoms at the surface of the substrate to obtain straight terraces. The length of the terraces is given by the miscut

angle of the substrate which determines then the duration of the thermal treatment. This implies that the smaller the miscut, the longer the time needed for the adatoms to reach a step. However, even though the time is miscut dependent, the temperature at which the substrate are treated is constant. In our case, a temperature of 960^{o}C was found to give good results. Figure 3.1 (c) shows an AFM topography picture of a treated substrate. The terraces are well defined and straight. Moreover, the flatness of the terraces and the height of the steps of 4$\mathring{A}$ are evidenced by a profile line, shown in figure 3.1(d), taken along the line shown in figure 3.1(c). All the samples grown on $SrTiO_3$ in this thesis were deposited using substrates treated using this procedure.

3.3 Growth conditions

The films were grown by pulsed laser deposition, using the system described in chapter 2. A stoichiometric target of $TbMnO_3$ was prepared by means of a standard solid-state reaction. The films discussed in the thesis were grown at a temperature of 750^{o}C in oxygen pressures of 0.25 mbar and 0.9 mbar. The laser energy density on the target was set at 2 J/cm^2, with a pulse repetition rate of 1Hz and a distance between the surface of the substrate and the surface of the target of 55mm. After deposition, the films were slowly cooled down (-3^{o}C/min) to room temperature after an oxygen pressure of 100 mbar was inserted in the chamber.

3.4 Structure and microstructure.

About eight RHEED intensity oscillations can be seen at the beginning of the growth corresponding to an initial layer-by-layer (2D-like) growth, see figure 3.2 (a). However, those oscillations are superimposed on a decreasing intensity background, indicating that an overall roughening occurs as the growth proceeds. After the oscillations have faded away, the intensity of the specular spots remains constant and the pattern

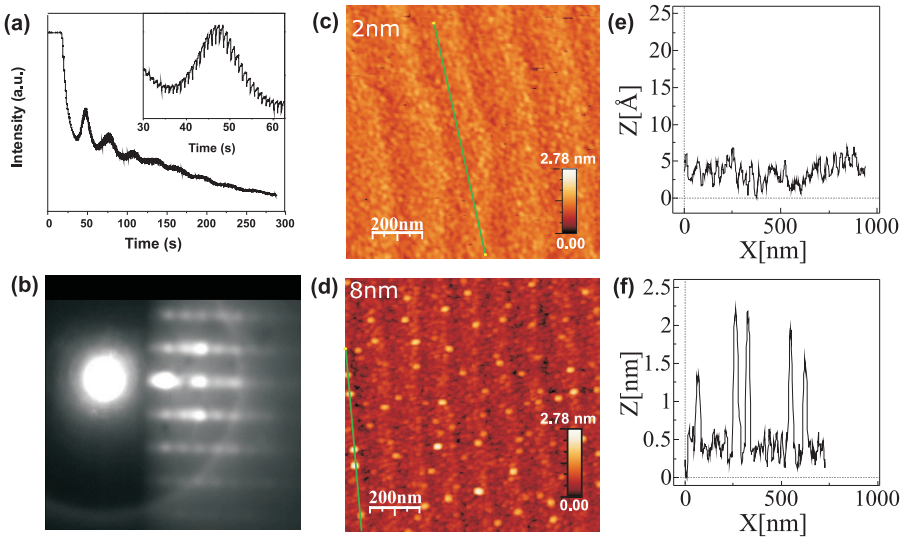

Figure 3.2: *(a)Intensity of the specular spot of the RHEED pattern as a function of deposition time. The inset is a blow-up of the first RHEED oscillation showing the laser pulses. (b) Typical RHEED pattern obtained after growth and annealing. The picture is taken after cooling down to room temperature and under vacuum. (c) and (d) AFM images of an 2nm and 8nm thin film, respectively, grown at pO_2= 0.25 mbar. The vertical and horizontal scales are shown at the bottom of the pictures. red(e) and (f) Profile of the surface taken along the lines drawn in (c) and (d), respectively.*

changes from a purely stripy pattern to the mixed stripe-spot pattern shown in Figure 3.2(b).

Figure 3.2 (c) shows the morphology of a 2nm film grown at 0.25mbar. It can be seen that the film is atomically flat, showing the step-and-terrace morphology of the substrate. However, when the deposition is stopped after 8nm, particles with a diameter of around 30 nm start appearing, as shown in figure 3.2 (d). In figure 3.2 (e) and (f), profile lines were taken in the AFM images of the 2nm and 8nm film, respectively. The profile line for the 8nm film was chosen to pass through a particle at the surface. This shows that for a 2nm film, the features at the surface have a height corresponding to half-unit cell to 1 unit cells whereas the particles on the 8nm sample have a height corresponding to one or two unit cells, showing the beginning of the islands nucleation.

Figures 3.3(a)-(c) show AFM images of three $TbMnO_3$ films with different thicknesses grown under the same conditions. In the 17nm film (figure 3.3 (a)), the grains

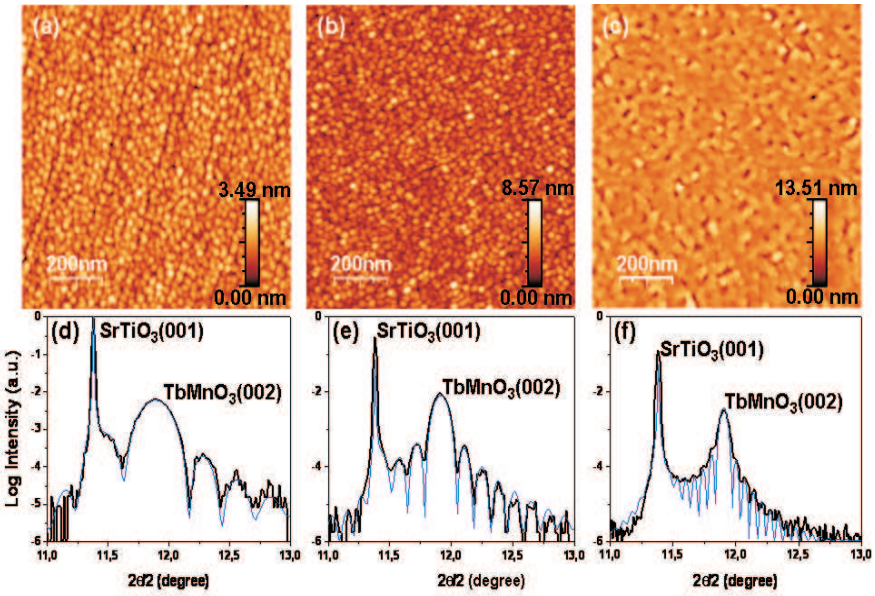

Figure 3.3: *AFM images of 17nm (a), 34nm (b) and 67nm (c) thick $TbMnO_3$ thin films grown with a pO_2= 0.25 mbar. The scans area is 1μmx1μm. The corresponding diffraction patterns can be seen in (d), (e) and (f), respectively. The experimental data are the thick black lines. The fit to the data is shown in each case as a thin line.*

dominate the film morphology but the steps from the substrate are still visible. Figures 3.3 (d)-(f) show typical 2θ-ω x-ray diffractograms along the $(00L)_c$ crystal truncation rod (the most intense peak in the pattern corresponds to the reflection of the substrate), for the same three films. The film peaks are those at the right hand-side of the $SrTiO_3$ reflections. The grey lines are the fit to the crystal truncation rods using a program based on a kinematical model. These calculations take into account, not only the complex refractive index of the substrate and the film, but also the angular dependent atomic scattering factors [99]. Despite the island-like growth discussed previously, the high quality and flatness of the interfaces is evidenced by the presence of Laue fringes around the film peak for thicknesses up to 67nm.

Figure 3.4 shows a broader 2θ-ω scan including both the $(001)_c$ and the $(002)_c$ $SrTiO_3$ Bragg reflections[1]. No secondary or impurity phases could be observed. A phi-scan around the $(024)_{pc}$ (i.e. $(2\bar{2}8)_o$) of $TbMnO_3$ (see inset) shows the peaks separated 90

[1]the subscript *c* refers to cubic indexes whereas the subscripts *pc* and *o* stand for pseudo-cubic and orthorhombic, respectively.

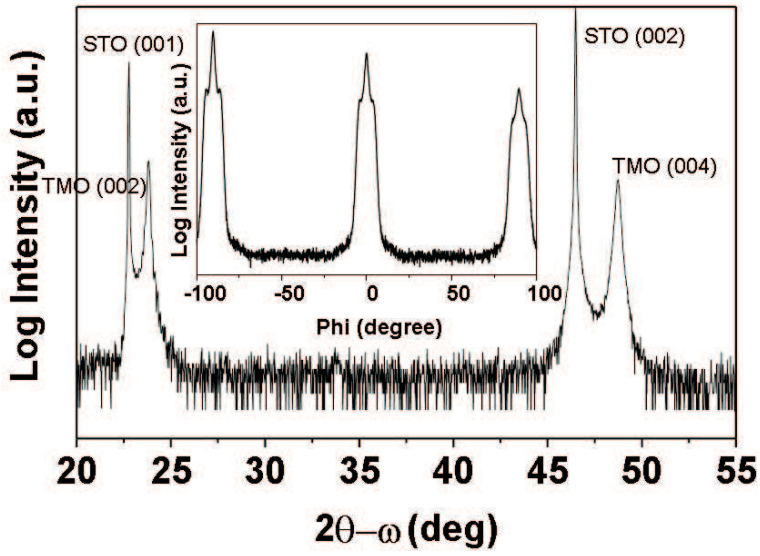

Figure 3.4: *2θ-ω for a 67nm thick film of $TbMnO_3$ grown on $SrTiO_3$ at 0.25mbar. Inset: Phi-scan around the $(2\bar{2}8)_o$ reflection.*

degrees from each other, confirming the four-fold symmetry of the film and the coherent growth. Moreover, shoulders can be seen around each peak in the phi-scan. For clarity, they will be explained later on this chapter. X-ray diffraction, thus, shows that the films are single phase and (001)-oriented (with the c-axis perpendicular to the surface). From the position of the film peaks of figure 3.4, an out-of-plane lattice spacing of 7.474 $\mathring{A}$, which is larger than the reported bulk value of 7.402 $\mathring{A}$, was found. This value is also larger than that expected for the compressively strained samples, as will be discussed later.

A larger out-of-plane lattice parameter than the expected one could be explained by a film whose strain is relaxed by means of oxygen vacancies, as they are known to expand the unit cell [100, 101]. To investigate this possibility, the oxygen pressure during deposition was increased up to 0.9 mbar (the maximum attained in our set-up). Increasing the oxygen pressure during growth reduced the growth rate, as expected from the decrease of the plume size, and hampered the initial layer-by-layer growth, leading to a 3D growth associated with a loss of RHEED oscillations. However, the RHEED patterns after annealing, as well as the optimal growth parameters, such as the

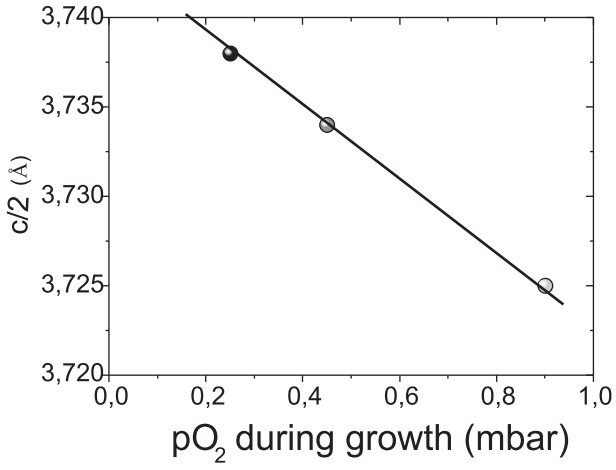

Figure 3.5: *Out-of-plane lattice parameters of $TbMnO_3$ films as a function of oxygen pressure during growth, for a substrate temperature of 750°C.*

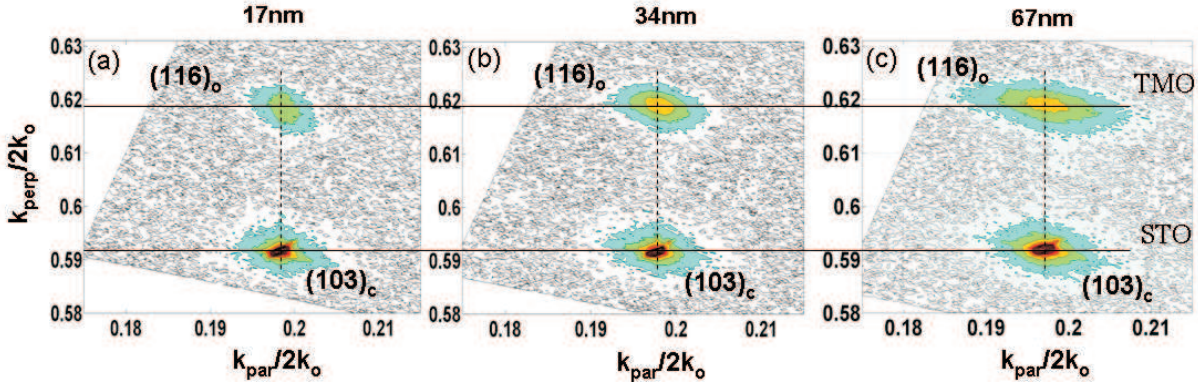

Figure 3.6: *Reciprocal space maps around the $(103)_c$ Bragg reflection of the $SrTiO_3$ substrate for 17nm, 34nm and 67nm films grown at 0.25 mbar. The vertical and horizontal lines are guides to the eyes. The abscissa (ordinate) represents the in-plane (out-of-plane) component of the scattering vector. Both axis are normalized by $2k_o=4\pi/\lambda$.*

repetition rate or temperature are similar to the ones related to figure 3.2 (b). Within the range of oxygen pressures investigated, the out-of-plane lattice parameter indeed decreases linearly with increasing oxygen pressure during deposition, consistent with the number of oxygen vacancies decreasing for increasing pressures, as shown in figure 3.5. Luckily, the maximum pressure of 0.9mbar seems to be large enough to produce stoichiometric films since the unit cell of the relaxed layers that are grown at large thicknesses is equal to the bulk one, as it will be shown later.

A detailed investigation of the film structure was performed using x-ray diffraction

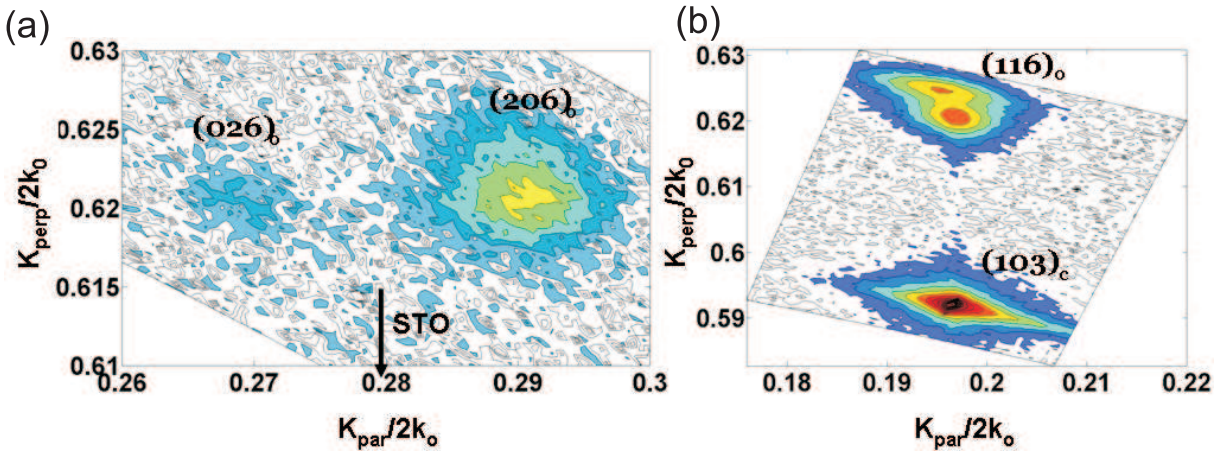

Figure 3.7: *(a)RSM around $(206)_o$ and $(026)_o$ for a 67nm thick $TbMnO_3$ film grown at 0.25 mbar. The arrow indicates the k_{par} of the $SrTiO_3$ substrate. (b)RSM around the $(103)_c$ $SrTiO_3$ Bragg reflection for a 80nm thick $TbMnO_3$ film grown at 0.9 mbar. The abscissa (ordinate) represents the in-plane (out-of-plane) component of the scattering vector, both normalized by $2k_o=4\pi/\lambda$.*

to map selected areas of the reciprocal space. Figures 3.6 (a)-(c) show reciprocal space maps (RSMs) around the $(103)_c$ Bragg reflections of a 17nm, 34nm and 67nm thick film, respectively, grown at 0.25mbar. The peaks originating from the films (substrate) are at larger (smaller) K_{perp} component (see horizontal lines in the figures). The in-plane and out-of plane components of the $(103)_c$ and $(013)_c$ $TbMnO_3$ peaks do not change as a function of thickness and the in-plane lattice parameter remains identical to that of $SrTiO_3$ for thicknesses up to 67nm, indicating that the films are coherent with the substrate along the pseudo-cubic [100] or [010] directions. As the thickness is increased, only a broadening of the rocking curve of the $TbMnO_3$ film can be seen. However, when the RSM is taken around the $(113)_c$, a different scenario is observed, as shown in figure 3.7 (a) for a 67nm thin film. Instead of a coherent peak, two peaks, corresponding to the film, are found that could be indexed as orthorhombic $(206)_o$ and $(026)_o$. The substrate peak cannot be seen in the scan as it lies in lower perpendicular component, but its parallel component is indicated by a black arrow in the figure. The data fit a structural model in which the films are orthorhombically distorted, similar to the bulk material, but keep coherence along the [100] or [010] directions of cubic substrate.

The orthorhombic a_o, b_o and c_o lattice parameters can be extracted from the $(116)_o$ and $(206)_o$ reflections shown above. Figure 3.8 shows the evolution of the lattice parameters as a function of thickness for the films grown with pO_2= 0.9 mbar and pO_2= 0.25 mbar. Both series display similar trend, showing that the oxygen vacancies, which are likely to be present in the films grown at the lowest pressure (giving rise to slightly larger c_o values), do not change the general behaviour. The orthorhombic distortion is the smallest for the thinnest films. With increasing thickness, c_o remains unchanged, while a_o decreases and b_o increases toward their respective bulk values. However, the bulk lattice parameters are not reached in a continuous way, and a_o and b_o saturate for a thickness of around 50 nm. Above about 70nm, a new spot appears in the diffraction maps, as shown in Figure 3.7 (b). This second spot corresponds to a relaxed unit cell with bulk lattice parameters (marked with stars in Figure 3.8). The fact that, in the films grown at 0.9mbar, this spot appears with lattice parameters almost identical to the bulk ones, strongly indicates that these films are stoichiometric, as discussed above. The lattice parameters for the thinnest film grown at 0.25mbar were extracted from grazing incidence diffraction, as shown in figure 3.9 (a). This figure shows that the film is fully coherent with the substrate and it is, thus, tetragonal.

We have shown that the films are orthorhombic (with the exception of the very thin tetragonal ones), but keep coherence with the cubic substrate along the $[010]_c$ or $[100]_c$ directions. Thus, the orthorhombic lattice parameters of the films fulfill $a_o^2 + b_o^2 = (2a_{STO})^2$ for all thicknesses of strained films. From the lattice parameters shown in figure 3.8, the orthorhombic distortion [102], defined by the angle γ (see figure 3.9 (b)), can be calculated using the relationship cos $((a_o{}^2\text{-}b_o{}^2)/(a_o{}^2\text{+}b_o{}^2))$. This is plotted along with the pseudo-cubic lattice parameters, obtained from the values of figure 3.8. As also seen in the reciprocal space maps, the pseudo-cubic lattice parameters for the strained films correspond to that of the $SrTiO_3$ substrate, whereas the orthorhombic distortion increases with increasing thickness, as seen by the decrease in the angle γ with increasing thickness. Moreover, in the relaxed part of the 80nm film, both the pseudo-cubic lattice parameters and the angle γ are relaxed to their

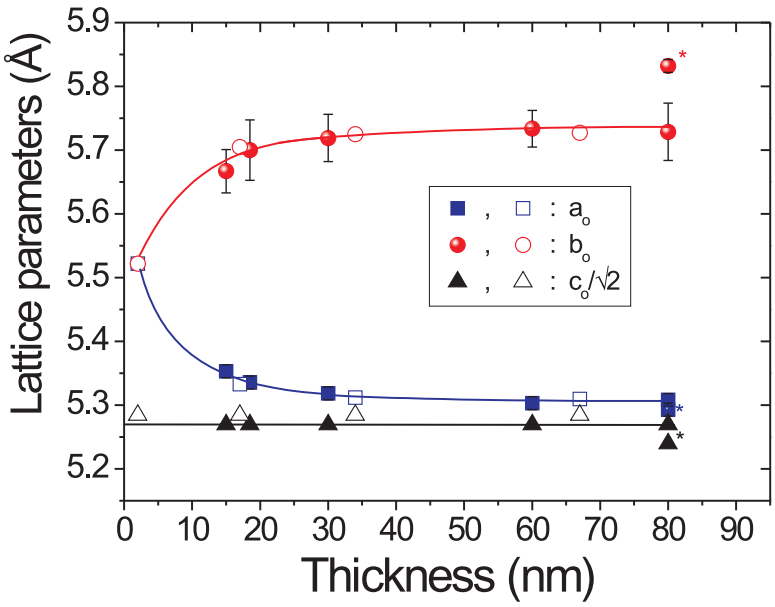

Figure 3.8: *Orthorhombic lattice parameters* (a_o,b_o,$c_o/\sqrt{2}$) *as a function of thickness for films grown with* pO_2*= 0.9 mbar (closed symbols) and 0.25mbar (open symbols). The symbols marked with a star are those of the relaxed part of the layers and correspond to the orthorhombic bulk lattice parameters [39].*

bulk values.

From the pseudo cubic lattice parameters of the films, we calculate a Poisson ratio of 0.397 and 0.316 for the films grown at 0.9mbar and 0.25 mbar, respectively. These values are comparable to those found for other manganites thin films: 0.35 for LSMO/STO [103] and 0.39 for LCMO/STO [104]. The lattice parameters of the films respect the relation $c_o/\sqrt{2}<a_o<b_o$, for a bulk Jahn-Teller system, suggesting that these distortions are also present in the films. It is worth noting that the orbital ordering takes place at 1500K, above the growth temperature.

In order to better understand the unusual in-plane coherence of the films with the substrate, observed by out-of-plane diffraction measurements and the domain structure of the film, GIXD experiments were performed using synchrotron radiation. Figure 3.10 (a)-(d) shows in-plane RSM's around selected reciprocal lattice points of the

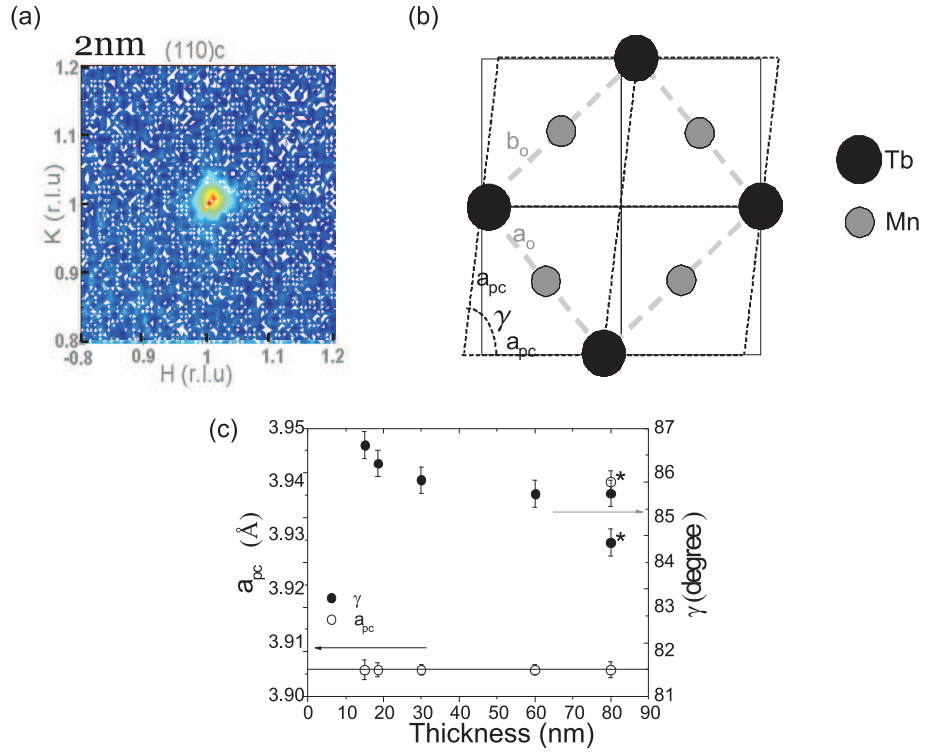

Figure 3.9: *(a) Grazing incidence x-ray diffraction for a 2nm $TbMnO_3$ thin film grown at 0.25mbar around the (110)c. The unit are normalized to the reciprocal lattice units of $SrTiO_3$. (b) Schematic drawing of the relationship between the orthorhombic and pseudo-cubic lattice parameters with the substrate lattice. (c) Pseudo-cubic angle (γ) and pseudo cubic lattice parameter (a_{pc}) as a function of thickness for the films grown at 0.9mbar. The bulk values are marked with a star.*

$SrTiO_3$ lattice for a 8 nm thin film grown at 0.25mbar.

In all the maps, the central sharp spot corresponds to the position of the $SrTiO_3$ Bragg peak and the other broader visible reflections around it are from the $TbMnO_3$ film. As shown in (a), four broad peaks can be seen around the (110) substrate spot. They correspond to the different equivalent orientations of the orthorhombic unit cell (see sketch in figure 3.12). The presence of these four domains maintains in the film the four-fold symmetry of the cubic substrate. Moreover, as shown in figure 3.10(b) and (c), a peak broadening in the perpendicular direction (along the [010] for the (100) reflection and along [100] for the (010) reflection), the so-called rocking curve, is seen around the central cubic position. This corresponds to the part of the film that is coherent with the substrate (with lattice spacing 3.905 Å). As seen in 3.10 (d), around the

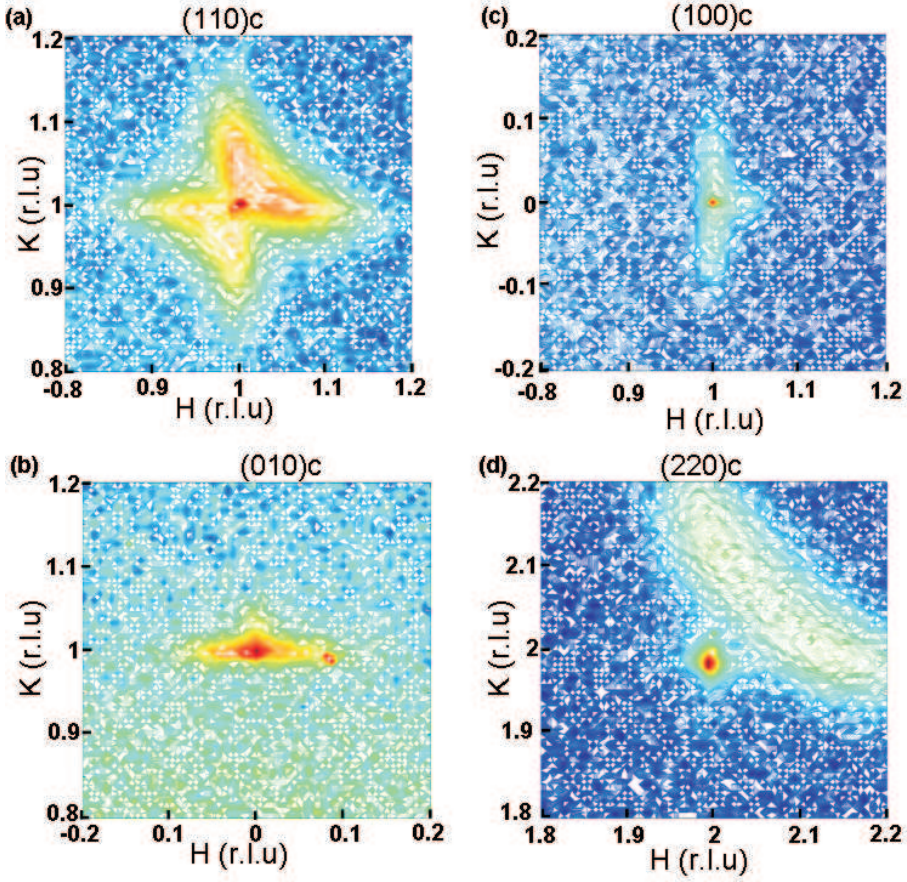

Figure 3.10: *RSMs of a 8nm $TbMnO_3$ film grown at 0.25mbar around: (a) the $(110)_c$; (b) the $(010)_c$; (c) the $(100)_c$ and (d) the $(220)_c$ $SrTiO_3$ Bragg reflections. The axes are in reciprocal lattice units of the substrate (1 r.l.u.= $2\pi/3.905$ Å)*

$(220)_c$, only two of the four peaks can be observed, those corresponding to the $(400)_o$ reflections. The absence of the $(040)_o$ peaks is due to the relative intensities of those reflections. Indeed, the intensity ratio $I(200)_o/I(020)_o$ is 1.4 in bulk, whereas a ratio of 77 is found for $I(400)_o/I(040)_o$. This makes the intensity of the $(040)_o$ too weak to be detected.

GIXD experiments were also performed for a 55nm film grown at 0.25mbar. Figure 3.11 (a)-(d) shows different in-plane RSMs for this thicker film. From (a), only two film reflections are observed around the substrate (110) peak (which in this case is not visible due to the grazing incidence geometry and the larger thickness of the film). The peaks correspond to the $(200)_o$ (higher H and K values) and the $(020)_o$ (at lower H

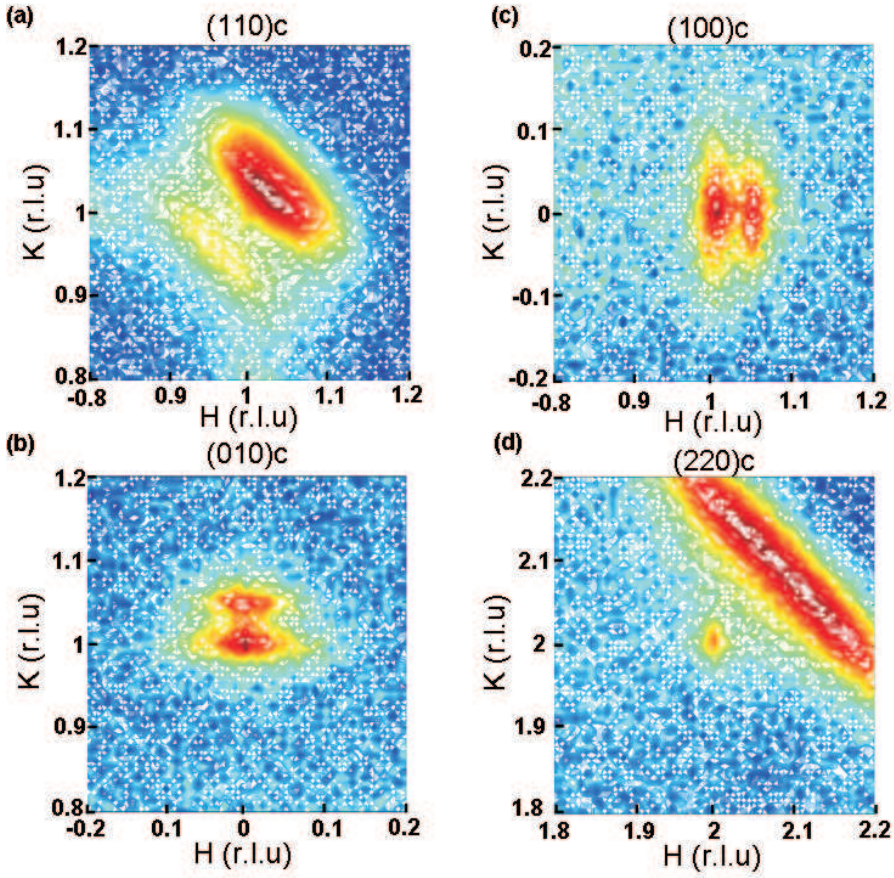

Figure 3.11: *RSMs for a 55nm $TbMnO_3$ film grown at 0.25mbar around (a) the $(110)_c$; (b) the $(010)_c$; (c) the $(100)_c$ and (d) the $(220)_c$ $SrTiO_3$ Bragg reflections. The axes are in reciprocal lattice units of the substrate (1 r.l.u.= $2\pi/3.905$ Å)*

and K values). Analysis of these diffraction maps indicates that, along with the change of a_o and b_o, a gradual rotation of the unit cell also occurs at larger thickness, so that the orthorhombic axes (a_o and b_o) align parallel to the [110] of $SrTiO_3$ (see figure 3.12). The extremely broad peak, in figures 3.11 (a) and (d), is due to domains existing at all orientations in between those sketched in figure 3.12 (a)-(b) and those in figure 3.12 (c).

The coherence with the substrate in the thinner films is then given by $[110]_o$ parallel to $[100]_c$ (or to $[010]_c$). By further increasing the thickness, the strain energy has increased such that the coherency along the $[100]_c$ cannot be kept and the films relax to their bulk structure, with the orthorhombic in-plane axis parallel to the $[110]_o$ of

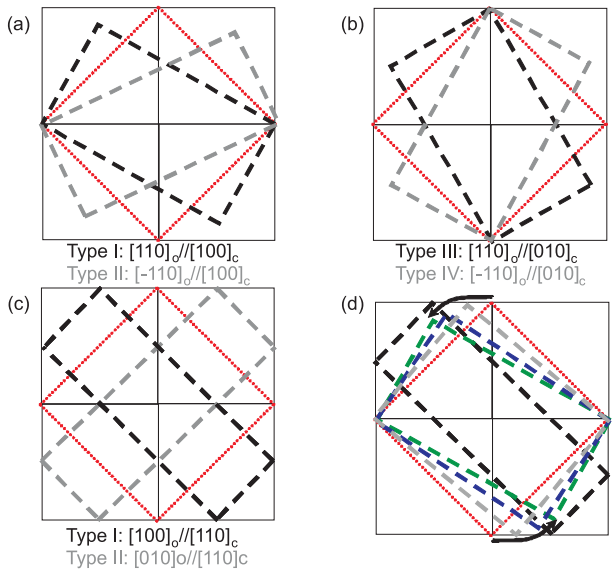

Figure 3.12: *(a) and (b)Sketch of the four types of orthorhombic domains present in the thinner films and their coherence with the substrate.(c) Sketch of the orthorhombic domains present in the thicker films and their coherence with the substrate. (d) Coexistence of different rotated domains with increasing thickness.*

$SrTiO_3$ (see figure 3.12 (c)). The superposition of (a) and (b) reproduces the shoulders seen in the phi scan of figure 3.4, around the peaks separated by 90°. In order to have more insight about the domain structure of the films and in an attempt to elucidate this observation, electron microscopy was utilized.

In figure 3.13, we show TEM plane view images recorded in different samples with thicknesses ranging from 17nm to 140nm, grown at 0.25mbar and with thicknesses of 30nm and 60nm, for films grown at 0.9mbar. In the plane view image of the 17nm $TbMnO_3$ film, two differently oriented types of domains can be seen, along with strain contrast within each orientation. This is consistent with the four types of domains seen via XRD. For the thicker film, two orientations can still be seen. Moreover, depending on the tilt angle (not shown here), strain contrast within a domain can be evidenced, confirming that the films are strained up to 67nm.

A comparative look at the samples grown at 0.25mbar shows that the size of the domains increases with increasing thickness. This means that the number of domain walls per unit area decreases with increasing thickness. The films grown at 0.9 mbar

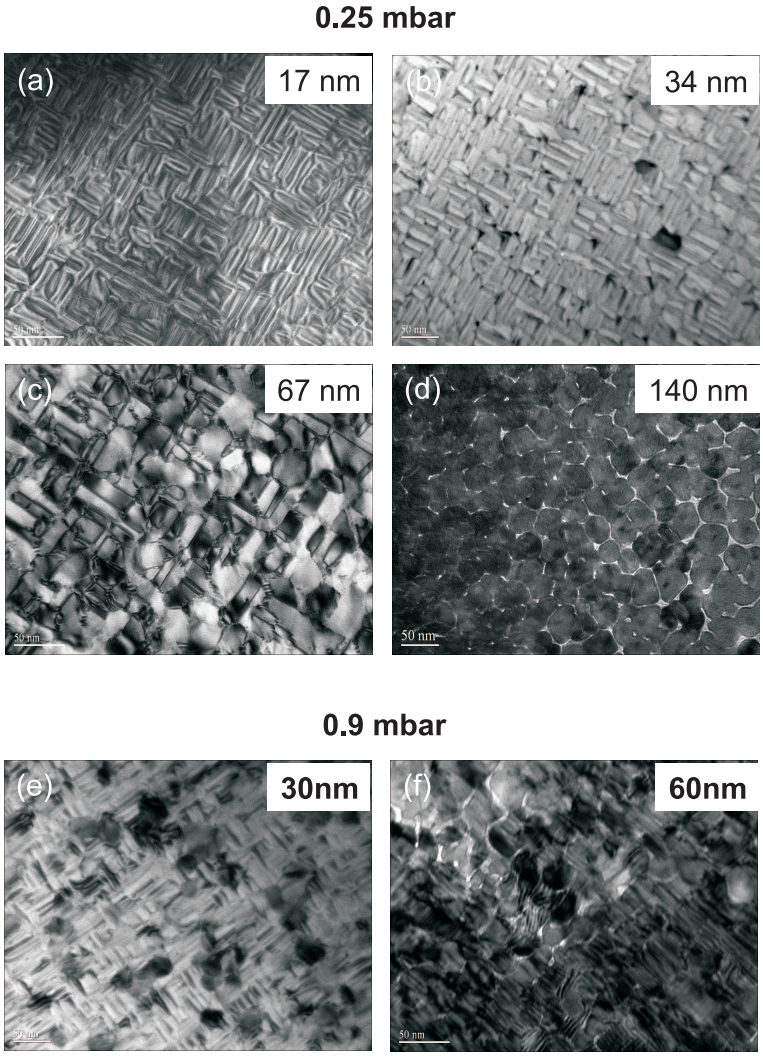

Figure 3.13: *Plane view TEM pictures of a 17nm (a), 34nm (b), 67nm (c) and 140nm (d) $TbMnO_3$ thin film grown at 0.25mbar. (e) and (f) Plane view TEM pictures of a 30nm and a 60nm $TbMnO_3$ thin films grown at 0.9mbar.*

show similar domain patterns but in this case the relaxation occurs at much smaller thicknesses, and already the 60nm thick film shows signs of relaxation, consistent with the x-ray diffraction data. This can be explained by the earlier 3D character of the growth that helps a faster relaxation for the films grown at 0.9mbar.

Figure 3.14 shows the electron diffraction patterns for a 17nm (a) and a 67nm (b) $TbMnO_3$ film grown at 0.25mbar, obtained in a plane-view geometry. The patterns confirm what has been seen in x-ray diffraction: for the thinner film the diffraction

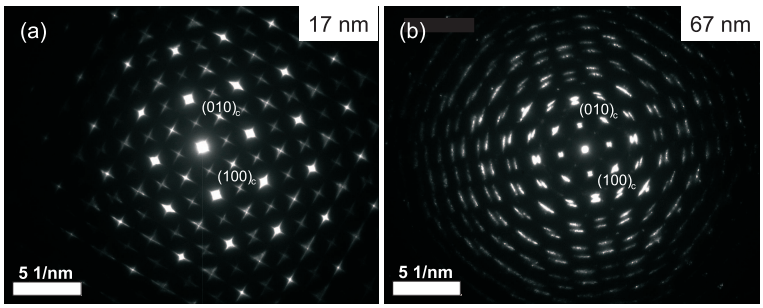

Figure 3.14: *Electron diffraction patterns for a 17nm $TbMnO_3$ film grown at 0.25mbar (a) and for a 67nm $TbMnO_3$ film grown at 0.25mbar (b).*

peaks are the superposition of four $TbMnO_3$ domains along with the contribution from the substrate; for the 67nm $TbMnO_3$ thin film, the electron diffraction pattern shows a gradual rotations of the domains, as discussed above. This confirms the gradual angular distortion occurring as the thickness is increased, concluded from x-ray diffraction experiments.

Cross-section TEM images for a film having a thickness of 67nm and for a film having a thickness of 140nm, both grown at 0.25mbar, are shown in figure 3.15 (a) and (b). The pictures evidence a dense structure with column-like shape for the 67nm film, whereas clear grain boundaries can be seen for the 140nm film. Moreover, strain contrast can clearly be seen on the 67nm film, at the interface with the substrate, which are absent for the relaxed 140nm film, showing the strained character of the films, despite the evolution of the lattice parameters with thickness.

In order to quantify the evolution of the domain walls with increasing thickness, the number of domains walls within an area of a chosen size were counted[2] for the samples grown at 0.25mbar. This quantitative analysis is shown in figure 3.16, where the number of domain walls per unit area is plotted as a function of the inverse of the thickness of the films and indicates a linear trend.

The number of domain walls per unit area for the 140nm thick film, which is relaxed and shows clear grain boundaries rather than a domain morphology, differs

[2]The statistical analysis of the TEM images, as well as the TEM images, and the results of figure 3.16 are performed by Sriram Venkatesan (Materials science research group, Zernike Institute for Advanced Materials).

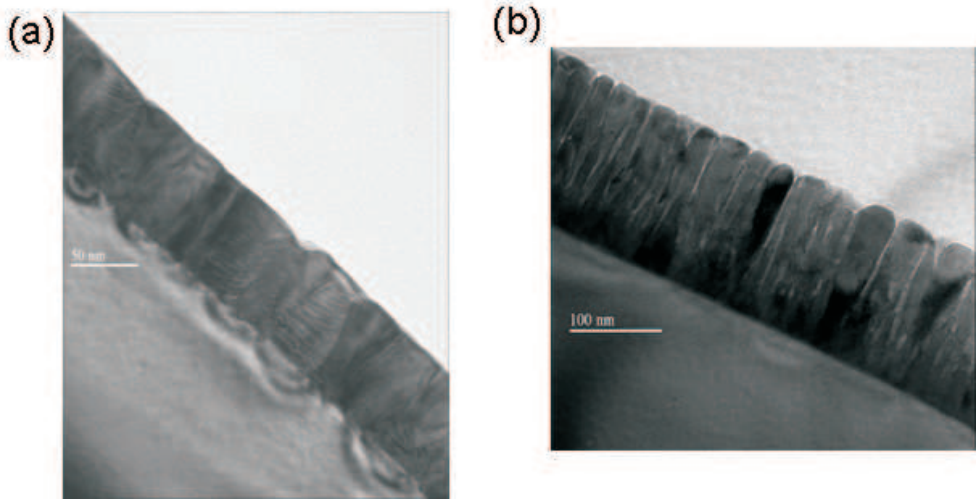

Figure 3.15: *(a) Cross-section TEM images for a $TbMnO_3$ thin film having a thickness of 67nm and grown at 0.25mbar. (b) Cross-section TEM images for a $TbMnO_3$ thin film having a thickness of 67nm and grown at 0.25mbar.*

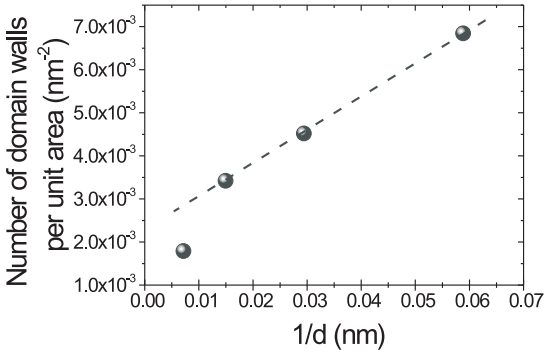

Figure 3.16: *Number of domains walls per unit area as a function of the inverse of the thickness.*

from the linear trend suggested for the range of investigated thicknesses.

3.5 Conclusions

We have successfully deposited epitaxial orthorhombic $TbMnO_3$ films on (001)-$SrTiO_3$, with thicknesses ranging from 8nm to 80nm. The crystal structure of the thin strained films has been identified as a less distorted orthorhombic unit cell compared to the

bulk one with $a_{film}>a_{bulk}$, $b_{film}<b_{bulk}$ and $c_{film}>c_{bulk}$. We found that the films grow with the c-axis out of plane and they orient themselves in the plane such that the $\langle 110\rangle_o$ directions align with the $\langle 100\rangle_c$ directions of the substrate. The orthorhombic lattice parameters a_o and b_o are constrained by epitaxy so that $a_o{}^2+b_o{}^2=(2a_{STO})^2$. This allows for four equivalent orientations and, therefore, four types of domains are observed, such that the in-plane diffraction patterns display four-fold symmetry. With increasing thickness, the in-plane orthorhombic axes gradually change toward their bulk values, increasing the orthorhombicity of the films, but still keeping the partial coherence and epitaxy relation $a_o{}^2+b_o{}^2=(2a_{STO})^2$. Due to this, the amount of strain is unchanged up to thicknesses of about 60nm for films grown at 0.9mbar and above 100nm for films grown at 0.25mbar, with the out-of-plane lattice parameter of the $TbMnO_3$ remaining constant. Above this thickness, the lattice relaxes to the bulk one. The possibility of decreasing the orthorhombic distortion via epitaxy, without involving composition changes, or of tuning the orthorhombicity by simply changing the thickness of the film, is of general interest, not only for manganites, but also for vanadates, nickelates and other perovskites, whose magnetic and orbital states are known to strongly depend on the degree of orthorhombic distortion. Finally, the number of domain walls per unit area could be quantified for the films grown at 0.25mbar, by an analysis of the TEM plane view images, and shows an increasing number of domain walls per unit area as the thickness is decreased. This (inverse) linear thickness dependence of the domain wall density is of crucial importance for the results presented later in this thesis.

Chapter 4

Magnetic and electronic properties of $TbMnO_3$ films on (001)-$SrTiO_3$

4.1 Abstract

In this chapter we show that, unlike the bulk material, the $TbMnO_3$ films display ferromagnetic interactions below the antiferromagnetic ordering temperature of $T_N \sim 40K$. Moreover, x-ray photoemission measurements in the films show that the Mn-3s splitting is 0.3 eV larger than that of the bulk. *Ab initio* embedded cluster calculations yield Mn-3s splittings that are in agreement with the experiment and reveal that the larger observed values are due to a larger ionicity of the strained films. The origin of the observed ferromagnetism is investigated. We have found strong indications that the ferromagnetism originates at the walls between crystallographic (antiferromagnetic) domains. However, induced ferromagnetism due to the decrease of orthorhombic distortion cannot be totally excluded.

4.2 Introduction

(001)-oriented $TbMnO_3$ thin films were deposited on atomically flat TiO_2-terminated (001)-$SrTiO_3$ cubic substrates by Pulsed Laser Deposition. The deposition was performed at a substrate temperature of 750^{o}C and at oxygen pressures of 0.25 and 0.9 mbar. Structural characterization, including high resolution synchrotron and lab diffrac-

tometer x-ray measurements, showed that the thin films grow under compressive strain and have a distorted orthorhombic perovskite structure with the [001] orientation and free from secondary phases. The thin films are clamped to the substrate along one of the in-plane [100]-directions, while they maintain an orthorhombic structure that evolves with thickness (with the orthorhombic distortion decreasing for decreasing thickness, reaching the tetragonal phase for ultra thin films of 2 nm). Four equivalent orientational crystallographic domains, all with the c-axis out of plane, are present so the films keep the four-fold macroscopic symmetry of the substrate.

4.3 Results

4.3.1 Magnetic properties of the $TbMnO_3$ thin films grown at 0.9mbar

Figure 4.1 shows the magnetic moment as a function of temperature for a 30nm TMO film grown at 0.9mbar, measured under zero-field-cooling (ZFC) and field-cooling (FC) conditions. The magnetization presents an up-turn at T*$\sim$40K, indicative of a magnetic phase transition. We notice that this transition is very close to the magnetic ordering temperature ($T_N \sim$40K), from the paramagnetic phase to the sinusoidal antiferromagnetic structure of the manganese spins, observed in the bulk compound. This transition is then likely to also be associated to the manganese spins ordering. Another transition is observed at around $\sim$10K, also present in bulk $TbMnO_3$, which can be associated to the terbium spin ordering.

Other features can be observed in this measurement: A splitting at low temperatures between FC and ZFC measurements can be seen below the manganese spin ordering temperature. This indicates that ferromagnetic interactions are present in the films. The films then behave differently from the bulk form of $TbMnO_3$, which does not display FC-ZFC hysteresis. The magnetic measurements did not reveal any feature related to the stabilization of the spiral antiferromagnetic ordering -concomitant with the onset of ferroelectricity- which occurs in bulk at $\sim$27K. However, due to the

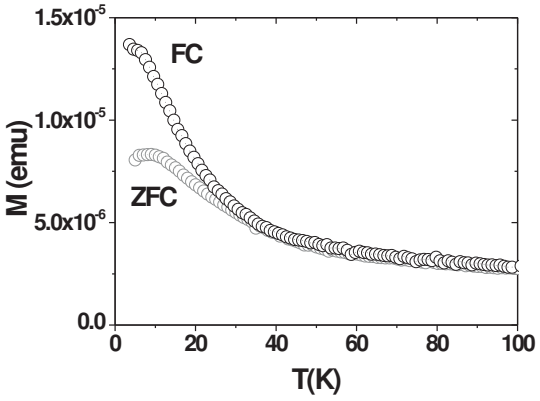

Figure 4.1: *Magnetic moment (M) as a function of temperature (T) for a 30nm TMO film grown at 0.9mbar. Data were recorded upon warming, with a 500 Oe field applied parallel to the film's surface. The diamagnetic contribution arising from the STO substrate was measured in a separate control experiment and subtracted from the raw magnetization.*

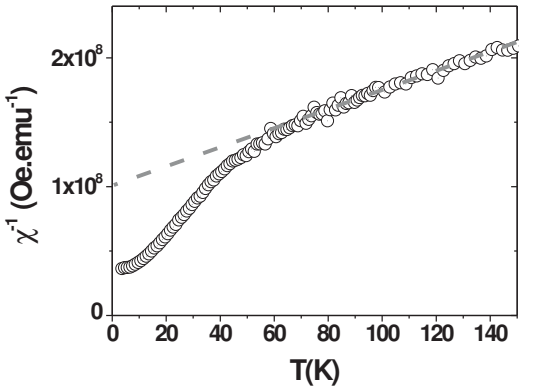

Figure 4.2: *Inverse susceptibility (χ^{-1}) as a function of temperature for a 30nm $TbMnO_3$ film grown at 0,9mbar.*

small sample volume and the substrate contributions, small anomalies in the magnetic susceptibility (as the one expected at the spin spiral transition) may be difficult to observe when measuring thin films. Moreover, one has to be very careful with the interpretation of magnetic measurements in thin films, where small amounts of magnetic impurity, often associated with the thick substrate, can provide a magnetization comparable to that of the films.

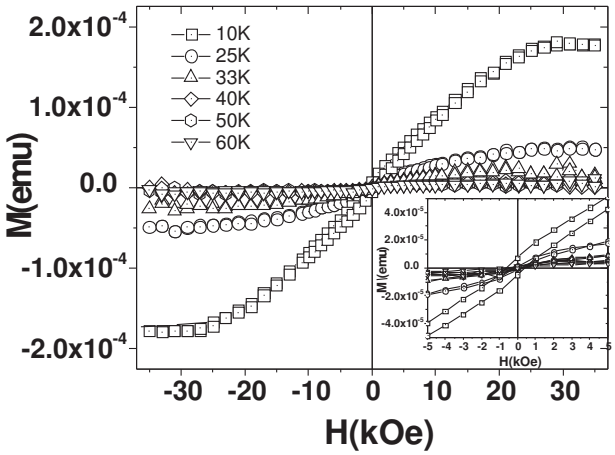

Figure 4.3: *Magnetic moment versus applied magnetic field at different temperatures ranging from 10K to 60K for a 30nm $TbMnO_3$ film grown at 0.9mbar. Both the diamagnetism of the substrate and the paramagnetism of Tb-ions have been deducted from the raw data.*

The deviation from the Curie-Weiss behaviour can be better appreciated in the evolution of the inverse susceptibility (χ^{-1}) with temperature (figure 4.2), where a change of slope can be seen at T*, consistent with a ferromagnetic contribution. The modeling of the high temperature tail of figure 4.2 by means of a Curie-Weiss law gives a negative extrapolated temperature ($\theta_{CW} \sim$ -150K), indicating that the dominant magnetic interactions are antiferromagnetic. Figure 4.3 shows magnetization loops measured at different temperatures from 10K to 60K and under applied magnetic fields ranging from -4T to 4T. From these loops, the saturation magnetization (M_S) is extracted. Figure 4.4 depicts the evolution of M_S with temperature, showing that ferromagnetic interactions develop below T*$\sim$40K. Since the maximum saturation magnetization is only 1.5 μ_B/fu, we can say that the character of the transition is ferrimagnetic-like. Similar effects have recently been observed in orthorhombic $YMnO_3$ and $YbMnO_3$ thin films [73, 75], as discussed in the introduction, which could suggest a general mechanism for induced ferromagnetism in manganite thin films.

Special attention should be paid to the possible existence of Mn_3O_4 impurities, which are ferrimagnetic with a T_C of 44K [105](even though we were unable to observe them by x-ray diffraction), and which could account for the presence of ferro-

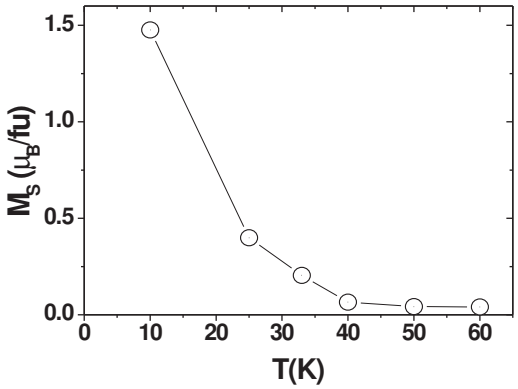

Figure 4.4: *Saturation magnetization (M_S) as a function of temperature for a 30nm $TbMnO_3$ film grown at 0.9mbar*

magnetism at low temperatures. However, that would imply a too large amount of Mn_3O_4 present in the films, which would have been detected by x-ray diffraction.

4.3.2 Effect of oxygen pressure during growth on the magnetic properties of $TbMnO_3$

The magnetic characterization corresponding to films grown at very different oxygen pressures (and different thicknesses, as will be discussed later) displayed qualitatively analogous results, as shown for a 100nm film grown at 0.25mbar and measured under the same conditions as the film grown at 0.9mbar, in figure 4.5. This indicates that the induced ferromagnetic moment in the films is not due to oxygen vacancies giving rise to a mixed-valence state. Indeed, a mixed valence state in the films can give rise to ferromagnetism mediated via the double exchange mechanism, common in doped manganites. According to our results, the oxygen pressure during deposition does not have a crucial role on the qualitative magnetic behavior of the thin films, for the investigated pressures.

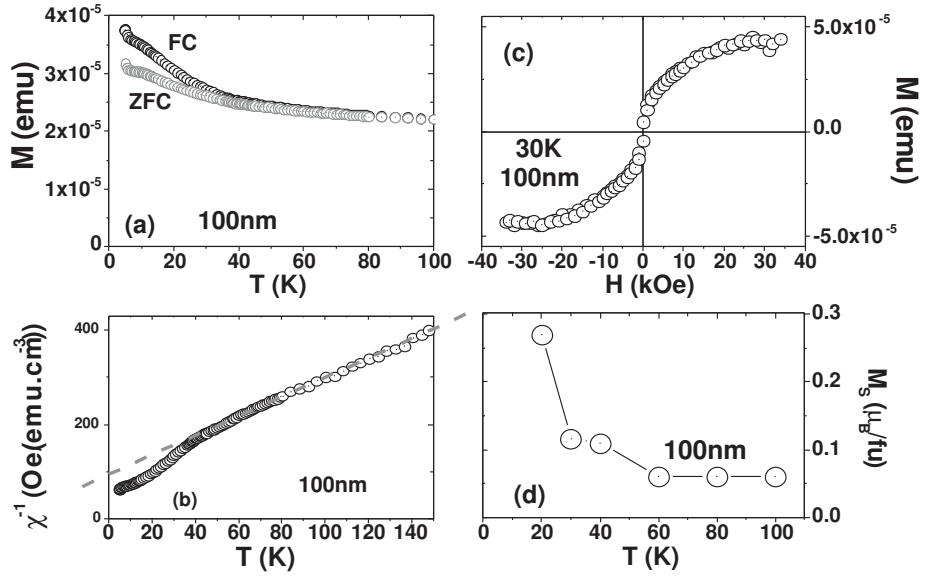

Figure 4.5: *(a) Magnetization (M) as a function of temperature (T) for a 100nm $TbMnO_3$ film grown at 0.25mbar. (b) Inverse susceptibility (χ^{-1}) as a function of temperature for the same film. (c) Magnetization versus magnetic field (H) at a temperature of 30K. (d) Saturation magnetization (M_S) as a function of temperature.*

4.3.3 Electronic properties of the $TbMnO_3$ thin films

In order to learn about the stoichiometry of the films, the oxidation state of manganese has been investigated. It is generally expected that oxygen content variations lead to a mixed valence state of the manganese in the system (Mn^{2+}/Mn^{3+} for oxygen vacancies [106, 107] and Mn^{3+}/Mn^{4+} for oxygen excess [106, 108]). XPS is a powerful tool to investigate the surface chemistry [109, 110]. The manganese Mn3s core level exhibits an exchange splitting characterized by two peaks in the XPS spectra. These peaks originate from the exchange coupling between the 3s hole and the 3d electrons [109]. A splitting of the manganese Mn3s core level of ΔE_{ex}=5-5.3 eV is expected for a nominal +3 valence. A decrease in the splitting is associated to a mixed +3/+4 valence state, whereas an increase of the splitting typically implies a mixed +2/+3 valence state. Even though the study of the Mn2p core level is not an easy task, due to the deconvolution of this core level into multiplets [111–113], the manganese Mn2p level exhibits also typical features depending on the valence state of the manganese. For +2 valence , a clear shake-up satellite can be seen at a binding energy of 647 eV, with a position of the

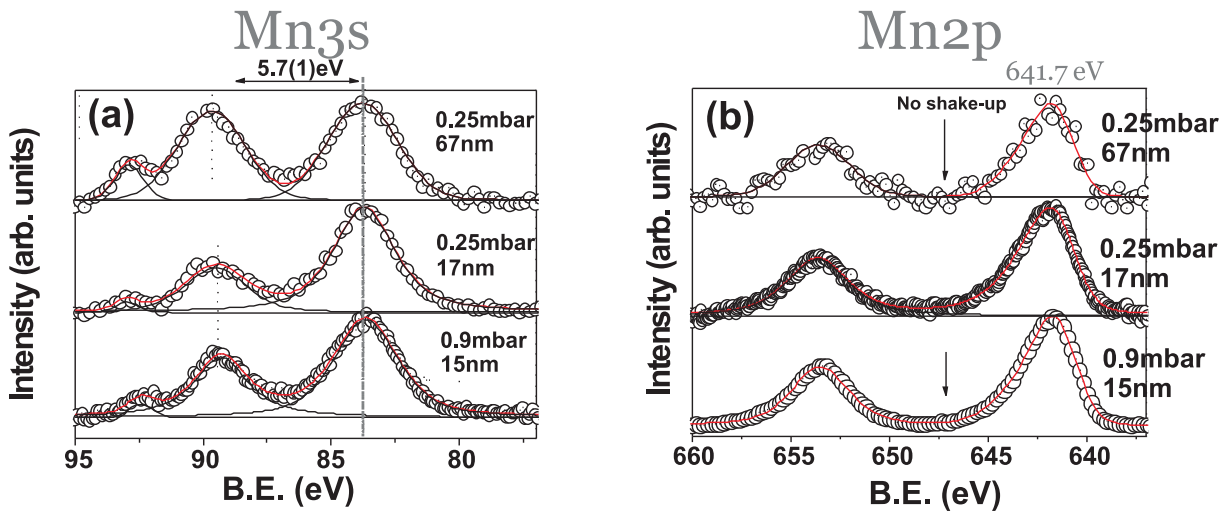

Figure 4.6: *(a) and (b) XPS spectra at the Mn3s and Mn2p core shells, respectively, $TbMnO_3$ films grown at pO_2= 0.25mbar and 0.9mbar for two different thicknesses. The lines are the fit to the peaks with gaussian profiles (two for the peak at 641.7 eV) after background subtraction (using the Shirley function).*

main peak around 640.8 eV. A valence of +3 exhibits a peak at a binding energy of 641.7 eV. Finally, a valence of +4 exhibits a peak at a binding energy of 642.8 eV. Moreover, the Mn2p peaks present a constant splitting of around 11.8eV [106, 114–116].

Figure 4.6 (a) shows the XPS spectra around the Mn3s core shell for films grown at 0.25mbar and 0.9mbar, for two different thickness. A splitting of the Mn3s core level of ΔE_{ex}=5.7(1)eV is found in our films, whose position does not change with thickness or oxygen pressure during growth. A third small peak can be seen at binding energies of around 93 eV, whose origin remains unclear. At first inspection, the splitting of 5.7 eV seems to indicate that the manganese in our films has a mixed +2/+3 valence and possibly oxygen vacancies. However, the splitting between the two Mn2p peaks, shown in Figure 4.6 (b), is Δ= 11.7eV, consistent with that expected for Mn^{3+}. Post annealing at very high oxygen pressures was done and no change in the splitting could be found. In addition, the Mn2p core level shows no shake-up satellites typical for the presence of Mn^{2+}. The low binding energy peak is found to be at 641.8 eV, also consistent with a nominal Mn valence of +3. No significant changes in the splitting are observed in the XPS spectra of the films grown with an oxygen pressure of 0.9mbar, and shown in

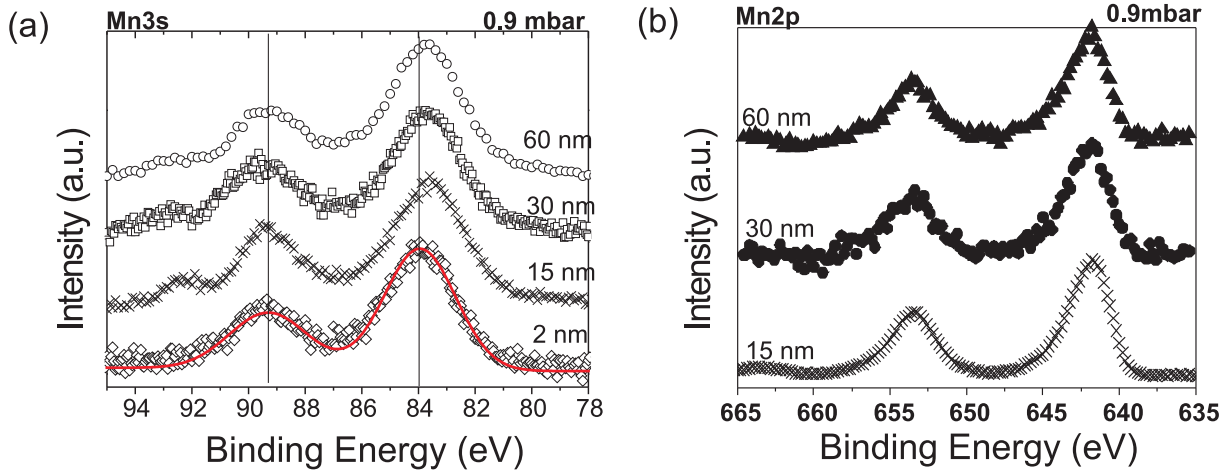

Figure 4.7: *XPS spectra at the Mn3s (a) and Mn2p (b) core shells, respectively, for $TbMnO_3$ films grown at pO_2=0.9mbar for different thicknesses. The line is a fit to the data after substraction of the background using the Shirley function. For clarity, only the Mn3s spectra is shown for the 2nm TMO film.*

Figure 4.6.

Thus, the comparison of the different XPS spectra leads to what appears to be contradictory conclusions: Irrespective of the oxygen pressure during growth or the thickness of the films, the relative large splitting in the Mn3s spectra indicate a mixed +2/+3 valence state of the manganese. However, looking at the Mn2p core levels of the same samples we find no indication of the shake-up peak associated with the Mn^{2+} valence. Moreover, the position of the low energy peak of this region agrees perfectly with the position of the manganese in a +3 valence state. In the next section, we will show that the increase in the splitting is due to a larger ionicity in the films. This strongly suggests that our films are stoichiometric and that the observed magnetization is not arising from a mixed valence that leads to the double-exchange mechanism [117].

The intensity of the peak with a binding energy of 93 eV, observed in our films, (see also figure 4.6 (a)) seems to be associated with the asymmetry and the intensity change observed for the peak at ≈89eV. The origin of this effect is unclear. It is worth to mention that the extra peak is absent in the fully strained and tetragonal (domain free) 2nm film (figure 4.7 (a)).

In order to shed light into the origin of the increased Mn3s splitting, configuration

interaction (CI) calculations[1] were performed, within the embedded cluster approach [118].

4.3.4 Cluster calculations

The electronic structure of an MnO_6 cluster is calculated with accurate quantum chemical schemes that ensure a precise and unbiased treatment of the strong electron correlation effects present in this type of materials. This MnO_6 cluster is embedded in a set of point charges that reproduce the Madelung potential in the cluster region due to the rest of the crystal. To avoid an artificial delocalization of the cluster electrons to the point charges, the centers nearest to the cluster are represented with model potentials [119] that account for the Coulomb and exchange interactions between the electrons in the cluster and the surroundings. This local approach has been successfully applied in the past to interpret XPS spectra of various ionic TM oxides [120, 121].

The final states responsible for the two peaks in the Mn3s XPS spectrum are characterized by a $3s^1 3p^6 3d^5$ electronic configuration. Only taking into account this configuration, very large exchange splittings are obtained in the calculations. However, it was shown by Bagus and collaborators [122] in the analysis of the exchange splitting in MnO that important contributions to the wave function arise from $3s^2 3p^4 3d^6$ electronic configurations. Semi-quantitative agreement with experiment can be obtained by also including the $3s^2 3p^5 3d^4 4f^1$ configurations. Applying this strategy to embedded MnO_6 clusters representing MnO, $LaMnO_3$ and $CaMnO_3$ give exchange splittings of 6.38, 5.72 and 3.95 eV, respectively. These calculated values are in good agreement with the experimental numbers: 6.2 eV for MnO; 5.3 eV for $LaMnO_3$ and 4.0 eV for $CaMnO_3$.

The embedded cluster for bulk $TbMnO_3$ was constructed using the experimental structure [39]. For the thin film cluster, we applied the lattice parameters of a 8nm film.

[1] These calculations, detailed in the next subsection, were performed by our collaborators Coen de Graaf (Department of Physical and Inorganic Chemistry, Tarragona, Spain) and Ria Broer (Theoretical Chemistry group, Zernike Institute for Advanced Materials, University of Groningen).

The CI calculations give an exchange splitting of 5.18 eV for bulk $TbMnO_3$ and 5.46 eV for the thin film. The slight underestimation in comparison to the experimental value of 5.7 eV reported in Fig. 4(a) is to be expected because in the calculations the 4f type expansion functions were not optimized. The increase of +0.3 eV in comparison to bulk is precisely what is observed in the experiment.

The steady increase of the exchange splitting from $CaMnO_3$ to $LaMnO_3$ to MnO suggests that the exchange splitting is determined by the formal ionic Mn charge as reported by Galakhov [123]. However, this relationship cannot be used to explain the different exchange splitting in bulk and thin film $TbMnO_3$, since in both cases the formal Mn charge is the same. Actually the calculated Mn charge is slightly smaller in the bulk than in the thin film contradicting the suggested relationship between Mn charge and exchange splitting. Serious doubts have been raised on the usefulness of the concept of the formal charge and/or oxidation state to interpret the electronic structure of transition metal compounds [124, 125]. Instead, we analyze the relation between the exchange splitting and the screening of the core hole by the oxygen ligands. For this purpose, the N-electron wave function is expressed in localized orbitals [118] and configurations are grouped by non charge transfer (Mn-$3d^5$), charge transfer (Mn-$3d^6L^{-1}$) and configurations with two or more electrons transferred from oxygen to Mn. This analysis shows that the screening of the core hole by the oxygens is more effective in the bulk than in the film; the charge transfer (CT) configurations have a larger weight in the wave function of the bulk cluster (44%) than in the film (38%). Hence, instead of the formal Mn charge, the exchange splitting is determined by the degree of oxygen screening. It is well known that MnO is highly ionic with almost no charge transfer in the wave function, while $CaMnO_3$ has a more covalent character with a much larger degree of screening, in line with the observed exchange splittings.

The reduced degree of core hole screening by the oxygens in the films is related to the shorter Mn-O distances in the ab-plane (Note that the Mn-O distance were extracted considering bulk atomic positions for the atoms considered). These shorter distances make that the oxygen-to-metal charge transfer configuration lies higher in

energy and contributes less to the wave function. In a one-electron reasoning this can be explained by the fact that shorter Mn-O distances lead to enhanced anti-bonding interactions, which increase the Mn-3d orbital energies. This causes a higher charge transfer energy, and hence, less effective ligand screening.

4.4 Discussion: Possible origins of ferromagnetism

With the previous study we rule out the double exchange mechanism between different Mn ions as the origin of the observed ferromagnetism. It is tempting to say that the decreased charge transfer in the films established previously, reduces the efficiency of the superexchange mechanism and enhances ferromagnetism with respect to the bulk case, in agreement with our experimental observations. However, given the subtle competition between ferromagnetic and antiferromagnetic exchange constants in this material [67] and the likely influence of the Tb ions, a more complex analysis of the magnetic structure of the films is needed. Strain can also have tremendous effects on orbital ordering [126], which determines the magnetic properties of $TbMnO_3$. To elucidate these possibilities, the full structure determination of the films, including the oxygen atomic positions, is compulsory but not technically possible at the present time.

Another possible origin of the observed ferromagnetism is the direct coupling between magnetization and strain. In this respect, there is an analogy between the induction of ferromagnetism in epitaxial antiferromagnets and the well-known induced ferroelectricity in incipient ferroelectrics [127, 128]. The strong coupling of the magnetic structure of $TbMnO_3$ to the lattice has been recently demonstrated [129]. The epitaxial stress in the films is estimated to be $2x10^8$ N/m^2, using a value of the Young modulus of 20 GPa [130] and, thus, the magnetization values observed are compatible with an effective piezomagnetic coefficient (linear part of the magnetostriction) of 10^{-10} m/A. This value is substantially smaller than the reported magnetostriction val-

ues in the bulk [129]. However, the presence of in-plane domains in the films makes it difficult to extract any final conclusions.

Finally, the origin of ferromagnetism could be in the microstructure. The TEM images shown in the previous chapter reveal that the size of the orthorhombic domains decreases for decreasing thickness and, thus, that the thinner the films, the larger the volume ratio of domain walls present. This is most relevant in order to understand the physical properties observed in the films, that is the induced ferromagnetism, and the absence of a lock-in transition. Although the orthorhombic domains of the bulk material are known to be antiferromagnetic in character, also in agreement with the negative Curie-Weiss temperature measured in the films, the interactions at the crystallographic domain walls could give rise to the observed ferromagnetic component. Moreover, the long range order of the spin cycloid that gives rise to the lock-in and ferroelectric transition, is disturbed by the presence of crystallographic domain walls/boundaries, which precludes the appearance of long range order and macroscopic polarization, consistent with our observations.

4.5 Thickness dependence of induced ferromagnetism

As stated above, the domain structure, characterized by XRD and clearly imaged by TEM (see Chapter 3) might be at the origin of the induced ferromagnetism. However, magnetostriction or another (indirect) effect of strain cannot be ruled out completely. Fortunately, as shown in Chapter 3, the strain state in the films is constant up to a thickness of about 70nm, while the density of domain walls increases linearly with decreasing thickness. So the evolution of the magnitude of the FC-ZFC splitting in the magnetization with thickness can help us narrow down the causes of ferromagnetism in our films.

Figure 4.8 shows the evolution of the magnetization of $TbMnO_3$ thin films with thicknesses ranging from 15nm to 80nm under zero-field-cooled (full symbols) and

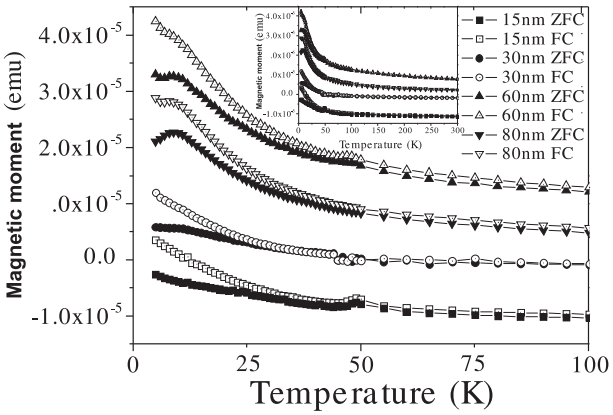

Figure 4.8: *Evolution of the magnetic moment, under zero-field-cooled (full symbols) and field-cooled (open symbols) conditions, as a function of thickness for the films grown at 0.9mbar. The inset shows the data up to 300K.*

field-cooled (open symbols) for temperatures ranging from 5K to 100K (the inset shows the data up to 300K).

For clarity, the raw data are presented. An unexpected small splitting at all the temperatures for all the samples can be observed (see inset of figure 4.8). This can be due to the shift of the sample during the field cooling due to the applied field or to ferromagnetic impurities with $T_c \geq 300$K, not relevant for the discussion. Due to the small response of the thin films, we are sensitive to small motion of the samples (same measurements repeated with a different sample mounting, resulting in a different splitting). This splitting at high temperatures is taken into account as the error bars in figure 4.10. This can not be explained by the substrate contribution, as it was measured to be negative ($SrTiO_3$ is diamagnetic) under this applied magnetic field (see figure 4.9).

To correctly take into account the substrate contribution is, indeed, a serious problem, since the $SrTiO_3$ substrates are known to contain impurities and different substrates show slightly different temperature dependence characteristics, specially at low temperatures. This small differences are critical in the case of the very thin films. The diffusion of silver paint (used to glue the substrate during growth and polished away after growth) into the $SrTiO_3$ cannot explain the extra magnetization at high tem-

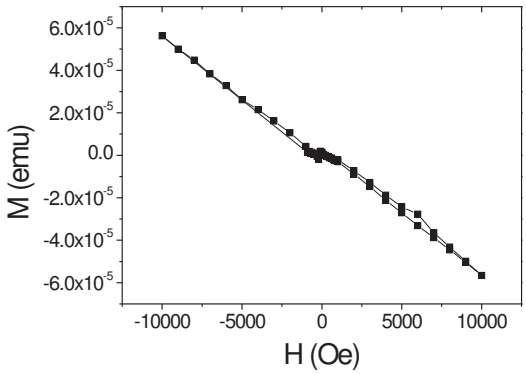

Figure 4.9: *Magnetic moment as a function of applied field for a bare $SrTiO_3$ substrate. The data were taken at 15K. $SrTiO_3$ is diamagnetic.*

peratures as it is also diamagnetic [131]. However, it can explain why the thinner films display a negative magnetization due to the bigger effect of the diamagnetic contribution from the substrate.

In order to extract the value of the FC-ZFC splitting, all the films were measured under an applied field of 1 kOe. The splitting was not measured at the minimum temperature but at 15 K instead, since at lower temperatures there is a change in behaviour with thickness, as the flattening due to the Tb ordering transition seems to be absent for the thinner films. Moreover, the paramagnetic contributions due to substrate impurities are smaller at higher temperatures. Figure 4.10 shows the evolution of the splitting between the ZFC and FC magnetization taken at 15K, normalized to the volume of the films. A decrease in the splitting with increasing thickness can be seen, from around 9 emu/cm^3, for the 15nm film, down to around 3 emu/cm^3 at 60nm. As shown in figure 4.10, there is a linear dependence of the splitting between the ZFC and FC curves with the inverse of the thickness for the films thinner than 80nm, those that are strained.

The induced magnetism shows the same thickness dependence as that of the density of domain walls, described in the previous chapter (see figure 3.16 in Chapter 3). For the thinner films, the crystallographic domains are found to be very small.

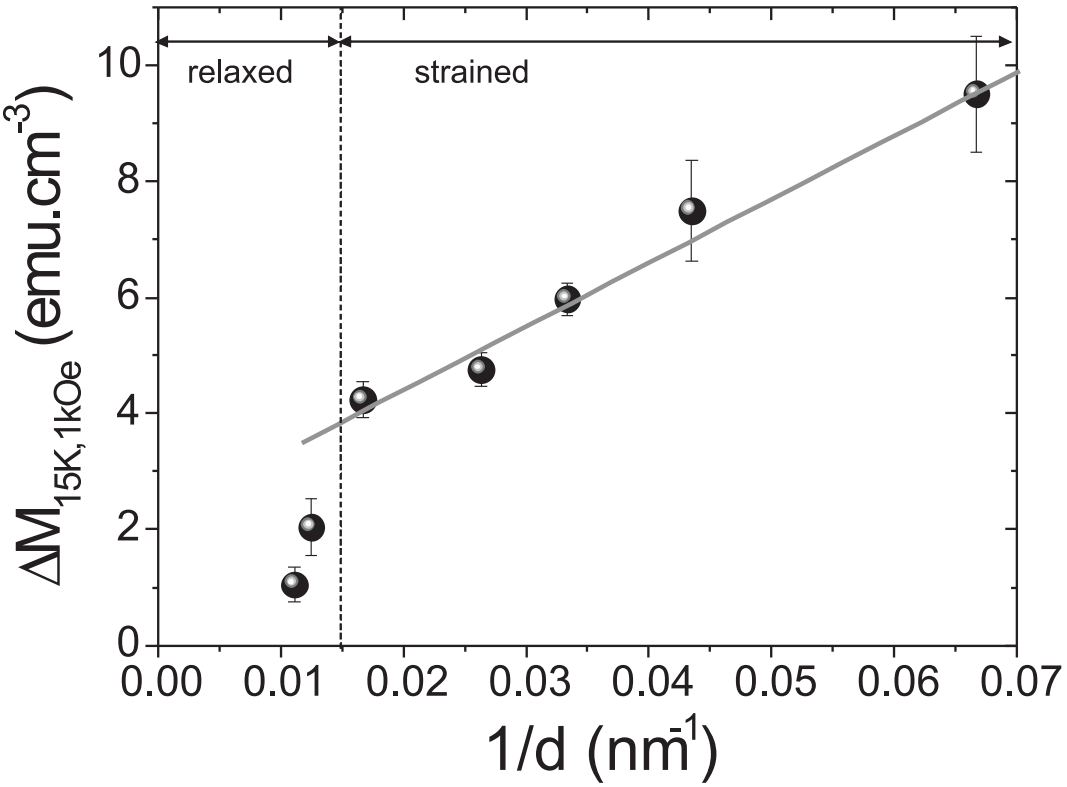

Figure 4.10: *Evolution of the splitting, between the zero-field-cooled and field-cooled magnetization, as a function of the inverse thickness, for the films grown at 0.9mbar. The error bars represent the value of the high-temperature splitting. The data have been normalized to the volume.*

This means that in the thin films the volume fraction of domain walls is very significant, and therefore the properties of the domain walls are likely to affect the overall magnetic properties. As the thickness is increased, the number of domain walls decreases, and therefore, also the magnetic response associated to them. The fact that the number of domain walls per unit area follows the same trend as the ZFC-FC splitting strongly suggests that the ferromagnetic interactions present in the film originate at the domain walls.

We turn now to check the effect of the orthorhombic distortion. As shown in Chapter 3, this can be measured by means of the pseudo-cubic angle, γ. Figure 4.11 plots γ as a function of the inverse of the thickness, also showing a linear behavior for the strained films. The orthorhombic distortion for the relaxed part of the thickest film,

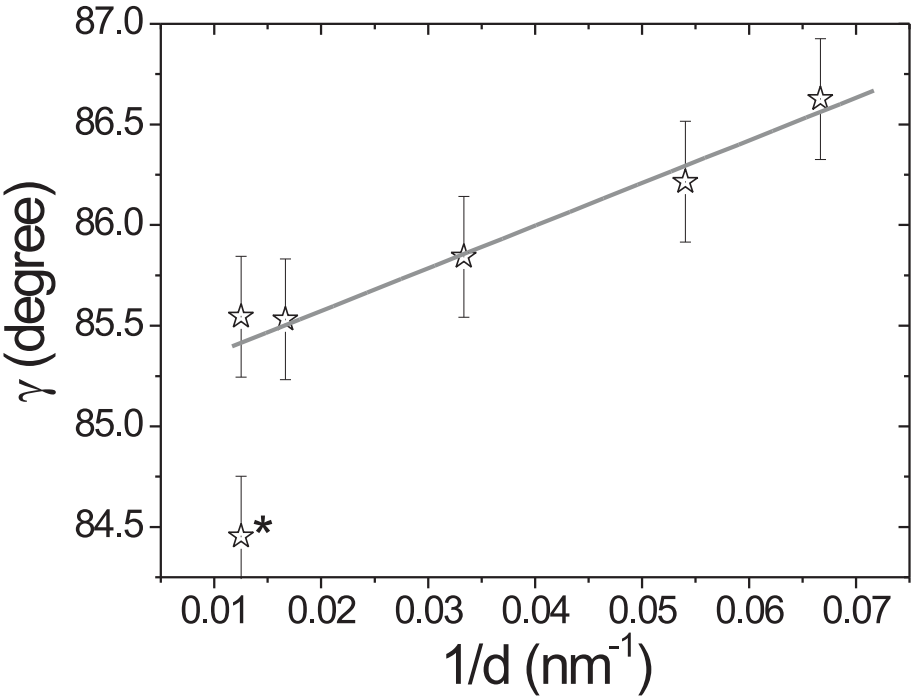

Figure 4.11: *Evolution of the orthorhombic distortion angle, γ, as a function of the inverse thickness for the samples grown at 0.9mbar. The black star indicates the value corresponding to the relaxed part of the film, which agrees with the bulk value.*

γ=84.4^o coincides with the reported bulk value. For the strained part present in the thickest film, the orthorhombic distortion saturates at a value of 85.5^o.

According to a very recent theoretical work, a decrease of orthorhombic distortion would modify the balance between the different competing exchange constants, increasing the ferromagnetic interactions [132]. This theoretical work of Dong $et\ al.$, which is a sequel of the microscopic model reproducing the cycloid phase in $TbMnO_3$ and $DyMnO_3$, discusses the possible ferromagnetism in manganites [132]. The calculations reproduce the different phases in manganites, including $TbMnO_3$. The hamiltonian used follows their previous work on manganites, and is expressed as:

$$H = H_{DE} + H_{AF} + H_{J2} + H_{JT} \tag{4.1}$$

where H_{DE} is the standard hamiltonian for double-exchange between e_g electrons, H_{AF} is the hamiltonian of the antiferromagnetic superexchange coupling between

nearest neighbours, H_{J2} is the nearest-next neighbour superexchange along the a and b axes and H_{JT} is sum of the hamiltonians of the electron-phonon coupling associated with the Jahn-Teller distortion and the energy of the Jahn-Teller distortion [132]. Although the standard double exchange associated to the hopping of e_g electrons between mixed valence ions is discarded (see previous section), Dong *et al.* can successfully reproduce the experimental phases by considering double exchange in undoped manganites. Using this model, the transition from an A-AFM to an E-AFM type magnetic structure has been reproduced as well as the intermediate cycloid state. The key point in the calculation is the appearance of a ferromagnetic phase when the model is extended to a three-dimensional infinite cubic lattice and the Jahn-Teller distortion is 'switched off'. As the Mn-O-Mn bond angle gets closer to 180^o degrees, the ratio between the double exchange and superexchange terms, will be enhanced, increasing the ferromagnetic tendency [132]. Moreover, the orthorhombic distortion stabilizes the $d_{3x^2-r^2}/d_{3y^2-r^2}$ type of orbital ordering, which would be suppressed in the nearly cubic lattice [132]. The effect of 'switching on' the Jahn-Teller distortion in the calculation decreases the ferromagnetic region but still cannot account for a reasonable value for the wavevector of $DyMnO_3$ [132]. It seems, thus, that the decrease of the distortion due to strain can, in principle, not be discarded as the possible cause of the ferromagnetism in the films. We will investigate now this possibility.

However, measuring the out-of-plane magnetic moment of strained films also reveals a ZFC-FC splitting below around 40K, as shown in figure 4.12 for a 60nm (a) and for a 20nm (b) $TbMnO_3$ film grown both at 0.9mbar. Both films show the same qualitative behaviour and ferromagnetic interactions are also evidenced out-of-plane. This is again different from the bulk behaviour, where the planes are antiferromagnetically coupled along the c-direction (see Introduction).

This is also not expected according to Dong's model previously discussed, since along this direction, the distortion is unchanged and therefore an antiferromagnetic response is expected. The induced ferromagnetism in the films is, therefore, not constrained to the ab plane, strongly suggesting that the ferromagnetic interactions ob-

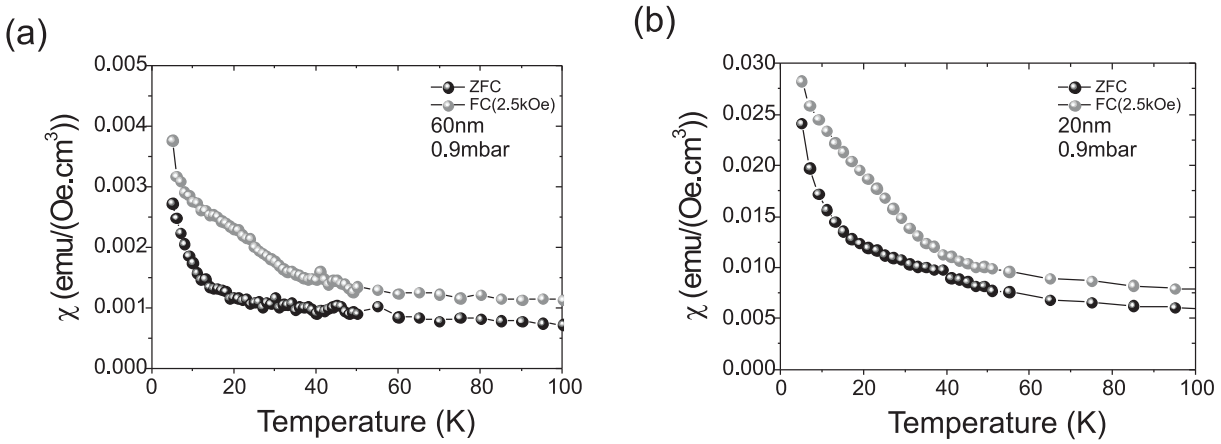

Figure 4.12: *(a) Zero-field-cooled (black circles) and field-cooled (grey circles) measurements of the magnetic susceptibility as a function of temperature for a 60nm $TbMnO_3$ film grown at 0.9mbar. (b) Zero-field-cooled (black circles) and field-cooled (grey circles) measurements of the magnetic susceptibility as a function of temperature for a 20nm $TbMnO_3$ film grown at 0.9mbar. The raw data are presented for clarity. In both measurements, the magnetic field was applied perpendicular to the surface of the films.*

served in the films are not directly related to the epitaxial strain, but instead to the presence of domain walls. The linear dependence of the orthorhombic distortion with the domain wall density is not coincidental since the size of the domains is directly related to the structural distortion [133]. Moreover, the fact that the observed splitting between the zero-field-cooled and field-cooled curves occurs at the bulk temperature of 40K, suggests that the bond angles are bulk-like and are not modified in the thin film form of $TbMnO_3$. However, the unfeasibility to refine the atomic positions and thus the bond distances and angles, makes any direct conclusion impossible at this stage.

If we assume that the crystallographic (and antiferromagnetic) domain walls are also ferroelectric (at least locally), that is they are multiferroic, we could naturally explain the ferromagnetic component: Symmetry arguments show that magnetoelectric coupling can induce ferromagnetism in the domain walls of ferroelectric antiferromagnets [134–136], and works by Fiebig and co-workers have also shown that the ferroelectric domain walls of multiferroic hexagonal manganites can have a net magnetization at their center [137] as well as enhanced magnetoelectric coupling [138, 139].

Recently, interesting properties have been observed in multiferroic domain walls in $BiFeO_3$ thin films, where conduction at the multiferroic domain wall was evidenced, pointing out the possible integration of such properties in devices at small scales [140, 141], as well as the peculiar properties of domain walls in magnetoelectric multiferroics. Knowing that the behaviour of the dielectric constant can also be affected by magnetic ordering, the measure of the dielectric constant is relevant in order to elucidate the origin of the induced ferromagentism and will be discussed in the next chapter.

4.6 Conclusions

In summary, $TbMnO_3$ films grown epitaxially on $SrTiO_3$ substrates display a strained orthorhombic perovskite structure less distorted than that of the bulk. This structural modification gives rise to an increased ionicity in the films with respect to the bulk. It has also been shown that the physical properties of these films are very different from those of the bulk: The films show ZFC-FC hysteresis below the N$\acute{e}$el temperature of $\sim 40K$, which is absent in the bulk. This can be of interest due to the scarcity of ferromagnetic insulators. Our data point towards the physical properties of the films being directly associated to the crystallographic domain walls, present in large quantities in the films: The investigation of the magnetic properties of the films as a function of thickness shows a linear increase of the splitting between the ZFC and FC, with decreasing thickness. The domain wall density follows the same trend, strongly indicating that the ferromagnetism originates at the walls. The fact that the orthorhombic distortion (pseudo-cubic angle) follows the same trend with thickness arises from the direct relationship betwen the domain size and the crystallographic distortion. The appearence of the induced ferromagnetism, both in the in-plane as well as in out-of-plane directions, strongly indicates that the induced ferromagnetism originates at the domain walls and is not directly caused by the epitaxial strain.

Chapter 5

Dielectric properties of the $TbMnO_3$ films

5.1 Abstract

In an effort to confirm or exclude the presence of ferroelectricity in the films and to characterize the magnetoelectric behaviour of the films, measurements of the dielectric constant and magnetocapacitance were performed. We show that the dielectric anomaly that indicates the paraelectric-ferroelectric phase transition is absent for films having a thickness below 70nm and is recovered for thicker films with a bulk-like relaxed part. A relaxation mechanism, involving polaron hopping, could be observed at around and below 1kHz. A second relaxation mechanism occurs at higher frequencies in the 40nm film and is attributed to the relaxation of domain walls. The data of the partially relaxed 90nm film suggests that the relaxation of domain walls is shifted to higher frequencies, pointing to a clamping effect of domain walls for the thinner films. Moreover, at high frequencies, the 90nm film shows a small magnetocapacitance effect of around 1%, whereas a magnetoresistance effect as high as $\approx 150\%$ could be measured under an applied in-plane field of 60 kOe, at 15K. These results indicate an interface-dominated positive magnetoresistance, possibly associated with the domain walls or grain boundaries. At lower frequencies, a core-dominated positive magnetoresistance is observed. We show here the crucial role of domain walls and grain boundaries on the dielectric properties of the films.

5.2 Introduction

The structure and magnetic properties of $TbMnO_3$ thin films on $SrTiO_3$ have been studied in the previous chapters and have shown that the films have a tetragonal structure for very low thicknesses (≈2nm) and, for increasing thickness, they gradually change into an orthorhombic structure, less distorted than the bulk one, by modifying the in-plane lattice parameters, a_o and b_o. However, with increasing the thickness of the films, the out-of-plane lattice parameter remains constant, indicating that the strain is maintained for thicknesses up to about 70nm (for films grown under 0.9mbar of oxygen). For thicker films, a coexistence of a strained and a relaxed part (with bulk-like lattice parameters) is found. Varying the oxygen pressure during growth (from 0.9mbar to 0.25mbar) did not seem to affect the magnetic properties of the films: dominant antiferromagnetic response with the signature of ferromagnetic interactions and an increase of the field-cooled induced magnetic moment with decreasing thickness. In addition, no anomaly could be detected in the magnetization curve corresponding to the transition to the spin cycloidal state (which induces the ferroelectric phase), as in bulk. Considering that the overall strain state is constant and looking at the TEM images shown in Chapter 3, which show a linear increase in the domain wall density with decreasing thickness, we have proposed that the ferromagnetic interactions originate at the domain walls.

In the past few years, many new multiferroics and magnetoelectric materials have been discovered and intensively studied. However, unreasonable dielectric and ferroelectric properties have been often reported due to a lack of knowledge of both the material investigated and the measurement technique. It has been shown that extrinsic contributions can give rise to a false large and frequency-dependent dielectric constant and can even give rise to magnetocapacitance effects. Moreover, leaky samples can display hysteresis effects in polarization measurements that can be mistaken for intrinsic ferroelectric properties of the material under study [142–144].

In the following experiments we investigate the dielectric properties of the $TbMnO_3$

films to confirm or exclude the presence of a ferroelectric transition. Indeed, a dielectric anomaly is found in the bulk material at the lock-in/ferroelectric ordering temperature ($T_f \approx 27K$). To find out if the ferroelectric ordering is suppressed by the strain, a film showing only a strained part (40nm) and a film showing strained and relaxed parts (90nm) were chosen. Moreover, performing an impedance spectroscopy study of the thin films, we can correlate the measurement of the capacitance and the dielectric loss with relaxation processes occurring in the films and separate the intrinsic and extrinsic effects. Dielectric measurements under magnetic field will give insight into the magnetoelectric behaviour of the films.

5.3 Experimental

$TbMnO_3$ thin films were deposited on conductive Nb-$SrTiO_3$(001) (1% doped) using RHEED-assisted Pulsed Laser Deposition (PLD). Nb-$SrTiO_3$ was used as a bottom electrode because the films grown on $SrRuO_3$//$SrTiO_3$ were (110)-oriented, different from those grown on bare $SrTiO_3$ (which show a (001) orientation) discussed earlier. This can be seen in figure 5.1, where an AFM image (a) and a x-ray 2θ-ω scan (b) around the (001) reflection of the $SrTiO_3$ substrate are shown. Although the topography of the surface is comparable to that of the films grown on a bare substrate, the x-ray diffraction data show a different diffractogram. Indeed, the peak corresponding to the film is seen on the left-hand side of the substrate peak, whereas films on a bare substrate had a peak on the right-hand side of the substrate. The evaluation of the out-of-plane lattice parameter for the $TbMnO_3$ layer reveals that the film is (110)-oriented.

A 40nm and a 90nm film were grown on Nb-$SrTiO_3$ under the same optimized conditions as those used for the growth on undoped $SrTiO_3$. The morphology of the films was studied using Atomic Force Microscopy (AFM), whereas the structure of the films was studied using x-ray diffraction. After structural characterization, $SrRuO_3$ top electrodes were deposited (600°C, 8.10^{-3}mbar, 2Hz) by using PLD and a mask. The elec-

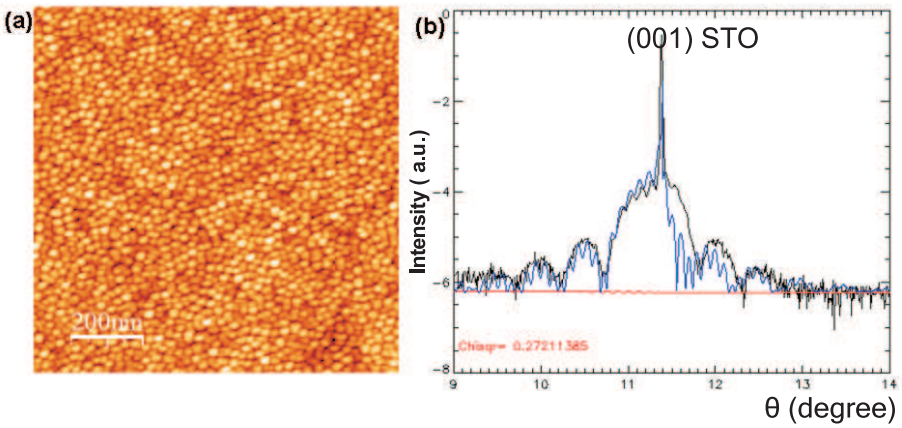

Figure 5.1: *(a) AFM picture for a 40nm $TbMnO_3$ film on a 10nm $SrRuO_3$ bottom electrode on (001)$SrTiO_3$ substrate. (b) 2θ-ω diffractogram of the corresponding film. The experimental data are shown as black line whereas the fit to the data is shown as a grey line.*

trodes were post-annealed in-situ at 600 ^{o}C under pO_2= 200mbar for 2hours. The top electrodes were then cooled down to room temperature at a rate of 3^{o}C.min^{-1}. The magnetization of these films was also measured. The dielectric measurements of the films were performed using a LCR Meter (see chapter 2). Temperature dependence of the capacitance and dielectric loss were recorded upon cooling, from 250K to 5K, as a function of frequency in the 40Hz-1MHz range. Measurements under applied magnetic field were performed under a maximum applied field of 6 Tesla.

5.4 Structure of the films grown on Nb-$SrTiO_3$

Figure 5.2 (a) shows the morphology images of the 40nm $TbMnO_3$ thin film grown on Nb-$SrTiO_3$. The steps of the substrate are not clearly visible, but the Fourier transform of the 5x5μm^2 image shows the periodicity of the steps (see right-top inset). The RMS roughness is estimated to be 1.1nm, comparable to that of the 40nm film grown on insulating $SrTiO_3$ under the same conditions. Figure 5.2 (b) shows the XRD pattern of the films, in which no signs of impurity or secondary phases are present. An out-of-plane lattice parameter of c=3.717Å was determined, which is smaller than that of the samples grown under the same oxygen pressure on an undoped substrate (c=3.726

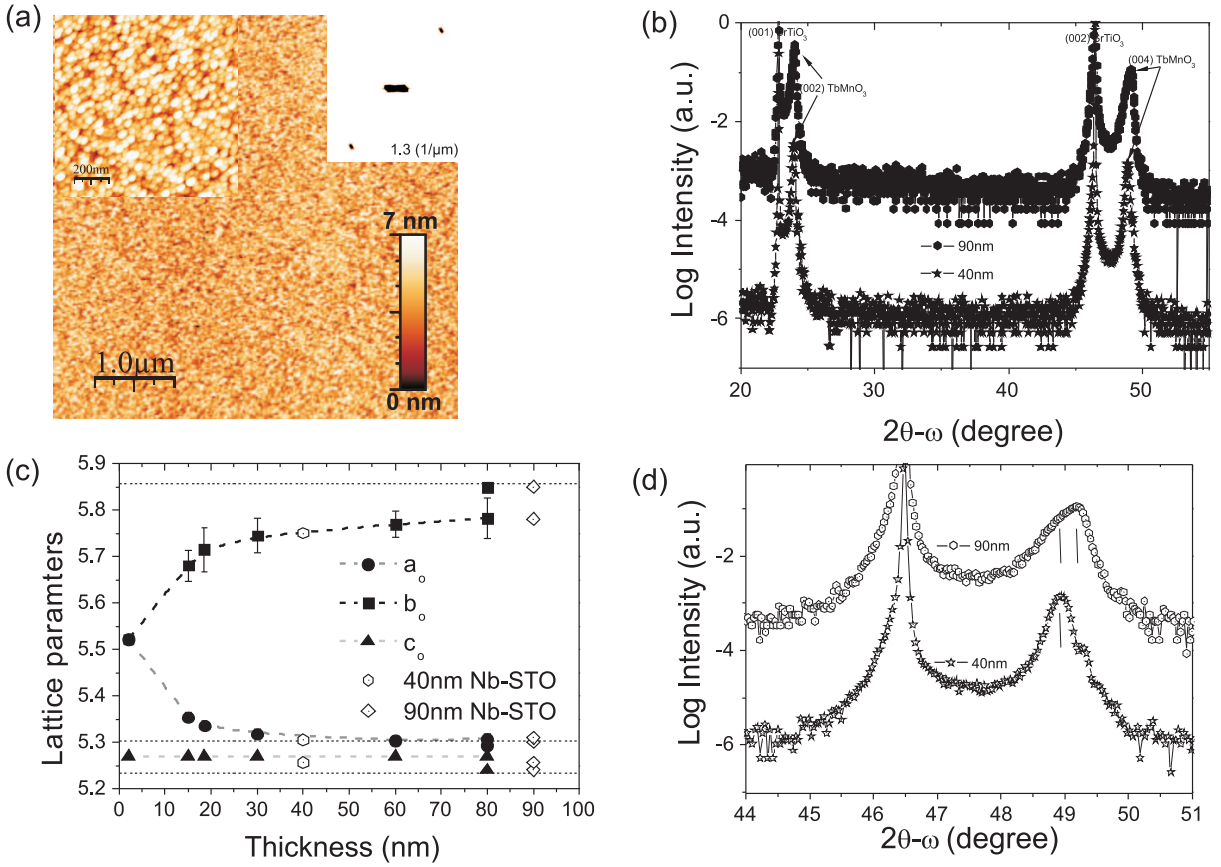

Figure 5.2: *(a) AFM picture for a 40nm $TbMnO_3$ film on Nb-(001)$SrTiO_3$. The inset in the left corner shows the AFM images at a smaller scale. The inset on the right corner shows the FFT of the image. (b) 2θ-ω diffractogram showing the epitaxy of the films. The stars correspond to the 40nm film whereas the circles correspond to the 90nm film. (c) Orthorhombic lattice parameter of the films grown on Nb-STO as compared with those of the films grown on an undoped substrate. Horizontal lines signal the bulk values. (d) Blow-up of (b) around the (002) reflection of $SrTiO_3$. The same symbols as in (b) are used.*

Å). This may be due to the very different electronic characteristics of the 2 substrates ($SrTiO_3$ is an insulator whereas Nb-$SrTiO_3$ is a n-type semiconductor). Figure 5.2 (c) shows the lattice parameters of the films compared with those of the other films grown at 0.9mbar on $SrTiO_3$, as determined by reciprocal space mappings around the (103) and (113) of the substrate. Figure 5.2 (d) shows that the 90nm film reflection consists of two peaks, corresponding to the relaxed and strained parts.

The films grown on Nb-$SrTiO_3$ showed the same general magnetic features as the other samples, namely dominant antiferromagnetic interactions with an induced mag-

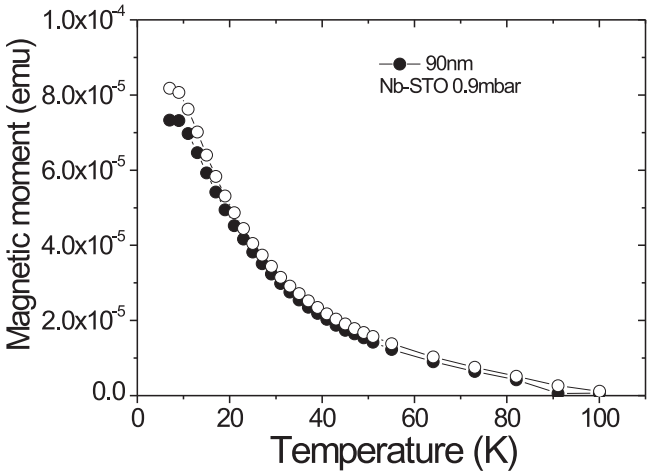

Figure 5.3: *Zero-field-cooled (full symbol) and field-cooled (open symbol) of the magnetic moment as a function of temperature for a 90nm $TbMnO_3$ film grown on Nb-$SrTiO_3$.*

netic moment , as shown in figure 5.3 (the value of the splitting is included in figure 4.10.)

5.5 Results and discussion

5.5.1 Dielectric behaviour

Figures 5.4 show the evolution of the real and imaginary parts of the dielectric constant as a function of temperature for a 40nm (left panel) and a 90nm (right panel) thick films, respectively, for different frequencies, ranging from 100Hz to 1MHz. As explained before, the 90nm film consists of a strained part and a bulk-like relaxed part (see figure 5.2 (c)-(d)).

Both thicknesses show similar behaviour with temperature: A step-like increase of the dielectric constant at T$\geq$100K, for frequencies below 100kHz, associated to a peak in the dielectric loss. However, the 90nm film shows a small anomaly in the dielectric constant at the bulk ferroelectric ordering temperature, consistent with the recovery of the cycloidal state in the bulk-like part of the films (figure 5.5 (b)). The anomaly cannot

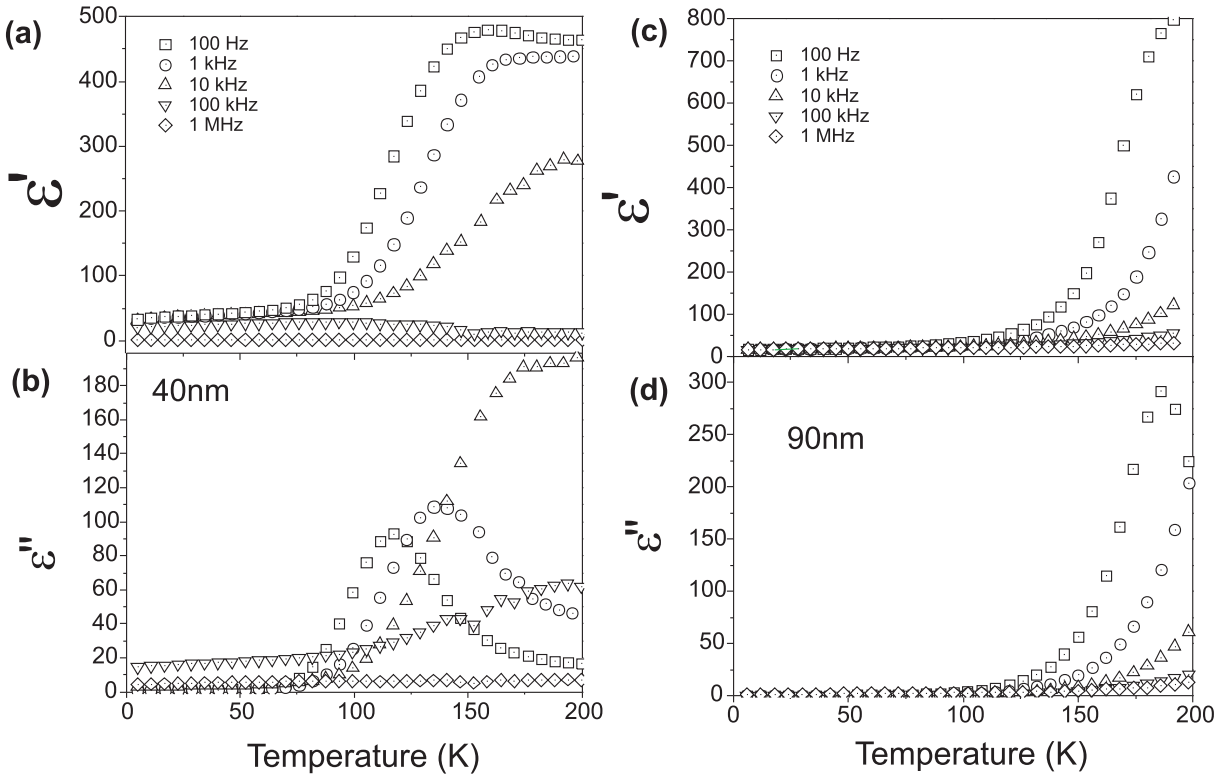

Figure 5.4: *Left panel: Temperature dependence of the real (a) and imaginary (b) parts of the dielectric constant under different frequencies of the applied voltage for a 40nm $TbMnO_3$ film grown on Nb-doped $SrTiO_3$ substrate. Right panel: Temperature dependence of the real (c) and imaginary (d) parts of the dielectric constant under different frequencies of the applied voltage for a 90nm $TbMnO_3$ film grown on Nb-doped $SrTiO_3$ substrate.*

be seen in the 40nm film (figure 5.5 (a)), indicating that the macroscopic ferroelectric state in $TbMnO_3$ is suppressed in the strained films . Above a frequency of 100kHz, the real and imaginary parts of the dielectric constant show very little variations with temperature.

For both thicknesses, the room temperature dielectric constant is as high as 500-1000. In the 40nm film, the low frequency dielectric constant at low temperatures (measured with the field along c), is about 30 [145], which agrees well with the bulk values [28, 54, 146]. The smaller value of the 90nm film is consistent with a two-layer model (strained and relaxed layers), or two capacitors in series for which the total capacitance is smaller than the individual capacitances. At room temperature, the dielectric constant is higher for the 90nm than for the 40nm film. This can be attributed

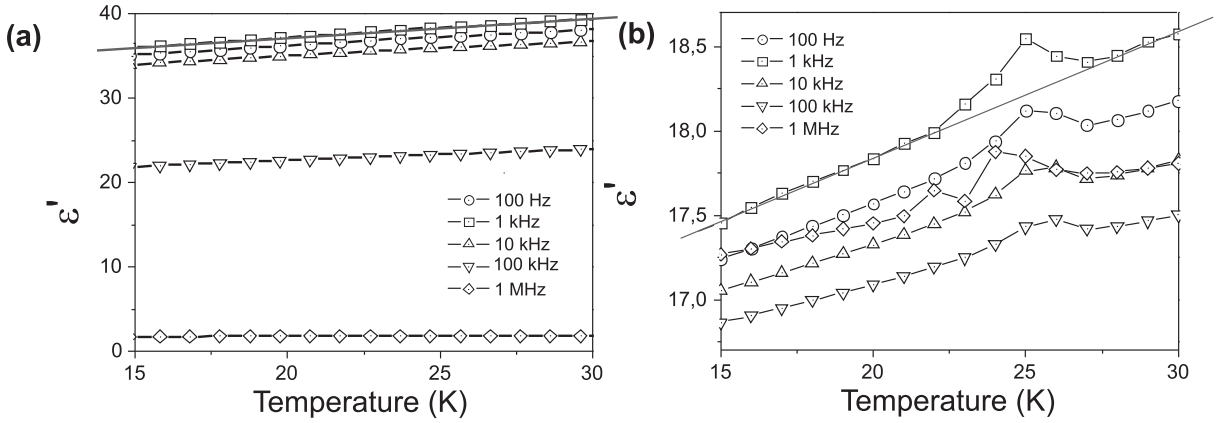

Figure 5.5: *Low temperature region of figure* 5.4*, of the real part of the complex dielectric constant for the 40nm (a) and 90nm (b) $TbMnO_3$ film for different frequencies, ranging from 100Hz to 1Mhz. The straight lines are a guide to the eyes.*

to the contribution of the grain boundaries, seen in TEM for a relaxed film (see chapter3).

Figure 5.6 shows the frequency dependence of the real and imaginary part of the complex dielectric constant and the ac conductivity at various temperatures ranging from 10K to 255K for both the 40nm (left panels) and the 90nm films (right panels). In the 40 nm film, two different relaxations are clearly observed for all temperatures. The dielectric constant shows an step-like decrease at about 10^5 Hz, associated with a peak in the imaginary part (figure 5.6 (a) and (b)). Above 40K, an indication of a second low-frequency relaxation is seen as an increase of the real part and an incipient peak in the imaginary part of the dielectric constant. For the 90nm film, the two mechanisms can also be inferred: the high frequency peak is shifted to higher frequencies and only a tail can be seen in the imaginary part, due to our limited frequency range (figure 5.6 (b), right panel). The relaxation at low frequencies can be observed only at the highest temperatures, and it shifts to lower frequencies, out of our measurable range, for temperatures lower than 175K.

This frequency dispersion is also observed in bulk samples [50, 146] and is discussed in terms of polaron hopping (dynamical localized charge carriers) [35, 50]. Indeed, in the presence of the Jahn-Teller effect, as soon as an electron hops into an

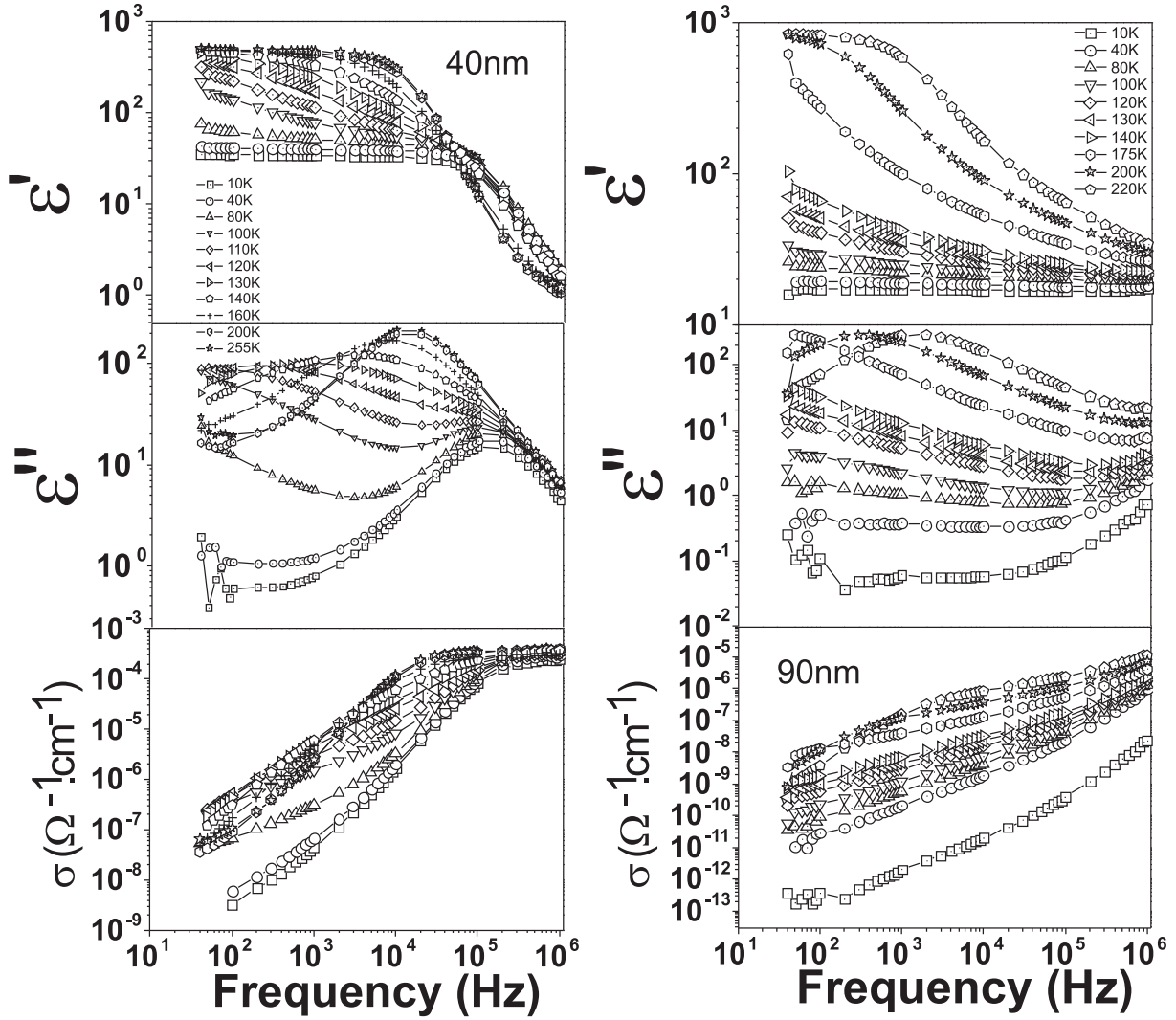

Figure 5.6: *Frequency dependence of (a) the real part of the dielectric constant, (b) imaginary part of the dielectric constant and (c) conductivity of a 40nm (left panels) and 90 nm (right panels) thick films of $TbMnO_3$ on Nb-$SrTiO_3$ substrates.*

empty e_g orbital, a distortion of the oxygen octahedral cage lowers the symmetry and further splits the e_g and t_{2g} levels. The electron is then more tightly bound, forming a so-called lattice polaron. Similar mechanism is reported for the conduction in other bulk rare earth manganites (orthorhombic or hexagonal) [28, 147, 148]. As it will be described below, our low frequency data is also consistent with polaron hopping.

With respect to the high frequency relaxation, a very recent work from Tokura's group found a similar peak in the dielectric loss for $DyMnO_3$ [149]. The onset of a

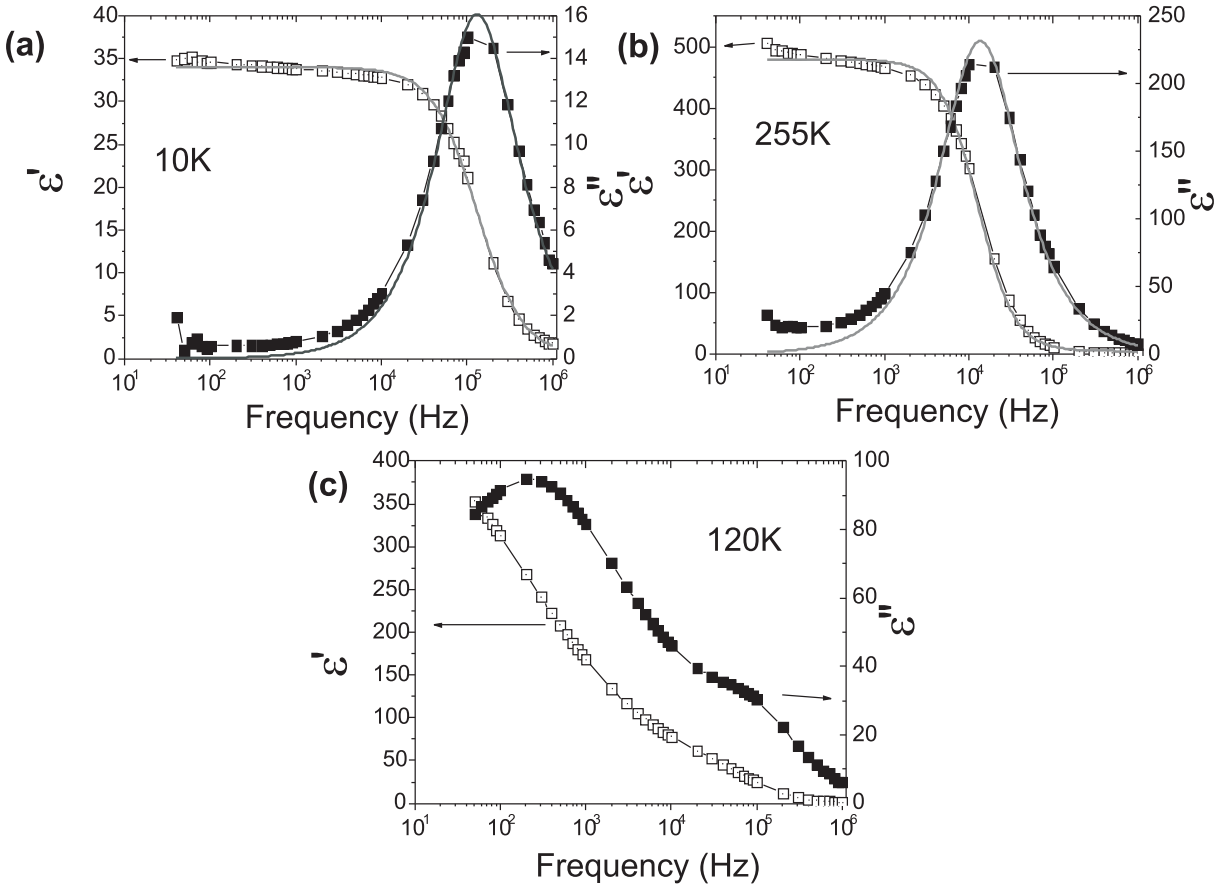

Figure 5.7: *Frequency dependence of the real and imaginary part of the complex dielectric constant as a function of frequency at a temperature of 10K (a) and 255K (b), for a 40nm $TbMnO_3$. The grey lines are the fit to the data using a Debye model. (c) Frequency dependence of the real and imaginary part of the complex dielectric constant at 120K.*

peak in the dielectric loss can also be detected in the work of Adem *et al.* on undoped $TbMnO_3$, although not discussed [28]. Kagawa *et al.* [149] have attributed the peak to relaxation of domain walls between domains presenting bc spin cycloids and those of the ac spin cycloids [149]. In the bulk $DyMnO_3$ compound, the frequency at which the relaxation appears is reported to be 10^7Hz [149], two orders of magnitude higher than that *observed for the* 40nm film but closer to the frequency suggested by the tail in the imaginary part for the 90nm film. This indicates that the clamping effect from the substrate decreases the relaxation frequency of the domain walls.

By fitting the data at different temperatures, the activations energies associated with the relaxations could be calculated using the relationship $\tau=\tau_o \exp(E_a/kT)$, where

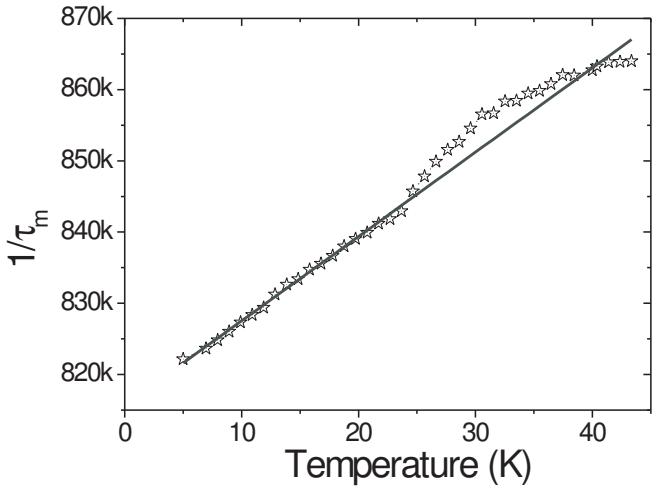

Figure 5.8: *$1/\tau$ versus temperature, for the high frequency relaxation of the 40nm film, demonstrating the absence of Arrhenius behaviour. The fit to the data are shown as a line.*

E_a is the activation energy, k is the Boltzmann constant and τ_o is the Arrhenius prefactor. The relaxation time (τ) was taken as the inverse of the frequency at the maximum of the imaginary permittivity. Figure 5.7 shows the frequency dependence of the real part and imaginary part of the dielectric permittivity at a temperature of 10K (a) and 255K (b) for the 40nm film. The lines, which are the fit to the data using a Debye model with a single relaxation time (see Chapter), show that the high frequency region could be well fitted with a relaxation time of the order of 10^{-5}s at 10K and of the order of 10^{-4}s at 255K. The intermediate region of temperatures shows the coexistence of the two relaxation mechanisms (see figure 5.7 (c)).

Concerning the high-frequency part, figure 5.8 shows the inverse of the relaxation time as a function of temperature. A weak temperature dependence and non-Arrhenius behaviour is found. At low temperatures, a linear increase with increasing temperature can be seen. However, above ∼25K the behaviour departs from linearity. So, even though the sinusoidal-to-cycloid transition is not observed in the magnetization data, the signature of this transition seems to appear in the dielectric data, affecting the behaviour of the domain wall relaxation. We can then suggest, consistently with our

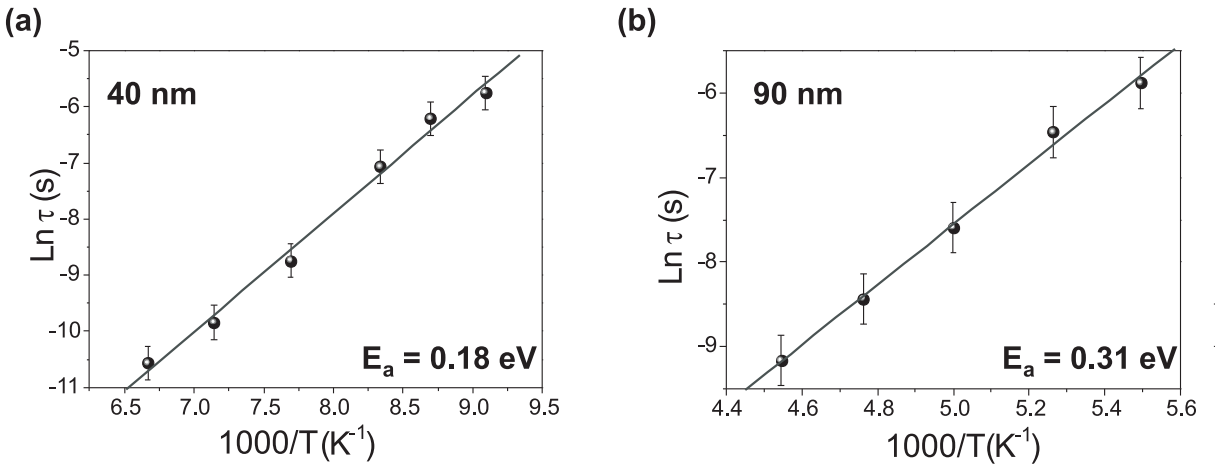

Figure 5.9: *ln (τ) vs. 1/T demonstrating the Arrhenius behaviour for the low frequency relaxation associated to the 40nm film (a) and the 90nm (b). The fits to the data are shown as lines in each case.*

findings in Chapter 4, that although long-range order (and, therefore, also ferroelectricity) is precluded by the presence of domain walls, the cycloid structure may be present in the domains at the local scale.

Figure 5.9 shows the Arrhenius plot for the low frequency relaxation in the 40nm (a) and the 90nm (b) films. From the slope of the fits, the activation energy of 0.18eV (τ_o=2.45x10^{-11}s) was obtained for the low frequency relaxation, for the 40nm film. For the 90nm film, an activation energy of 0.31eV (τ_o=9.59^{-12}s) could be obtained from the data. The values are comparable to those of single crystals of $TbMnO_3$ (0.269eV) and for $Tb_{1-x}Ca_xMnO_3$, with x=0.1 (0.107eV) [28]. For other manganites, these are found to be 0.215eV ($LaMnO_3$), 0.245eV ($NdMnO_3$) and 0.373eV ($HoMnO_3$) [147], and have been attributed to polaron hopping, as discussed above. Interestingly, these activation energies in manganites have been related to the degree of Jahn-Teller distortion and show an increase with increasing Jahn-Teller distortion [147]. This suggests that the degree of Jahn-Teller distortion is reduced in thin films of $TbMnO_3$, in agreement with a less distorted crystal lattice.

Ionic conduction should also be considered as a plausible mechanism for the low frequency relaxation. In the case of perovskites, in which no interstitial sites are available for hopping of ions, the ionic conduction would likely be due to oxygen vacancies.

However, the activation energy of oxygen diffusion is found to be around 1-1.1eV [150], suggesting that the activation energies found in the films cannot be attributed to ionic conduction.

Dielectrics having localized charge carriers show an ac conductivity, following the equation $\sigma=\sigma_{dc}+\sigma_o\omega^n$, where ω is the angular frequency, σ_o and n being temperature dependent constants and n ranging between 0.6 and 1 (there are exceptions of materials having a n exponent much lower than 0.6 or higher than [96,151,152]). By plotting log (σ) versus log(ω), a dielectric following the "Jonscher's power law" (or the so-called universal dielectric response) shows then a linear behaviour, from whose fit the n exponent can be obtained. As shown in figure 5.6 (c), this is the case in a wide range of frequencies for the 40nm film (left panels) and the 90nm film (right panels) grown at 0.9mbar. This is clearer in the 90nm film due to the absence of the high frequency relaxation mechanism in the measured range of temperatures and frequencies. Similar results for the low frequency mechanism have also been reported in single crystals [28] and ceramics [153] of $TbMnO_3$. The *n* exponent obtained from these data vary between 0.4 and 1 (see also chapter 6).

5.5.2 Impedance analysis

An impedance analysis was performed, for the first time, for thin films of $TbMnO_3$. Figure 5.10 shows the evolution of ϵ" vs ϵ' at different temperatures ranging from 10K to 255K for the 40nm film (a) and 90nm (b). By comparing the plots at 10K and 255K, and as suspected by the fits of the real part and imaginary part of the dielectric constants, both temperatures display a semi-circle, typical for a Debye-like relaxation associated to a model of capacitance and a resistance in series. For the 90nm films, only one semi-circle is obtained for the measured range. For this sample, the high asymmetry of the circles can be attributed to a Debye exponent different that one (see chapter 1), indicating a spread of the relaxation times, due to the presence of a larger amount of disorder in the thicker films. However, the intermediate range of temperature shows

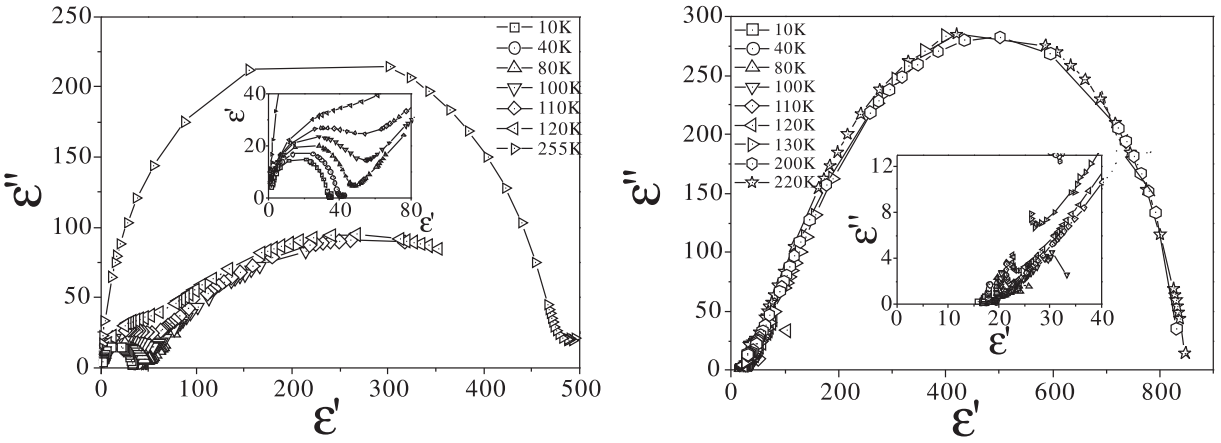

Figure 5.10: *ϵ" vs ϵ' at different temperatures ranging from 10K to 255K for a 40nm (a) and a 90nm (b) $TbMnO_3$ film*

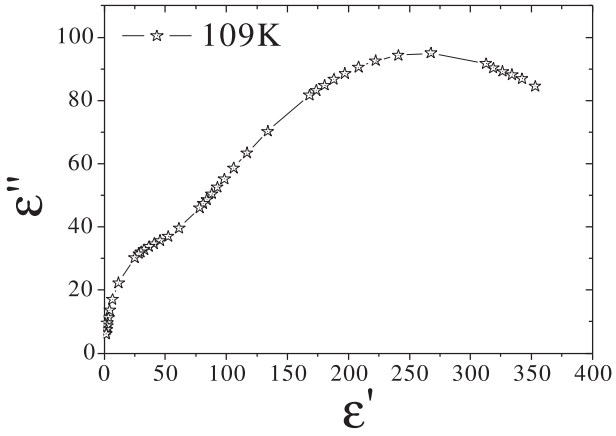

Figure 5.11: *Cole-cole plot for the 40nm $TbMnO_3$ film, taken at 109K, where the low and high frequencies relaxations can be clearly seen.*

the coexistence of the two relaxations (see figure 5.11) for the 40nm film. As the temperature is decreased, the second semi-circle starts being revealed.

Then, the high dielectric constant observed at room temperature and low frequencies, found to be in the order of 500 for the 40nm film, could be due to the confinement of polarons at the domain walls, causing a kind of depletion layer at the walls or due to the depletion layers at the electrodes/film interfaces (Schottky barrier). In figure 5.12, the frequency dependence of the dielectric constant is plotted for different amplitude of the ac field for a 40nm $TbMnO_3$ film. A clear voltage dependence of the real part of the dielectric constant can be seen, at low frequencies, consistent with the presence

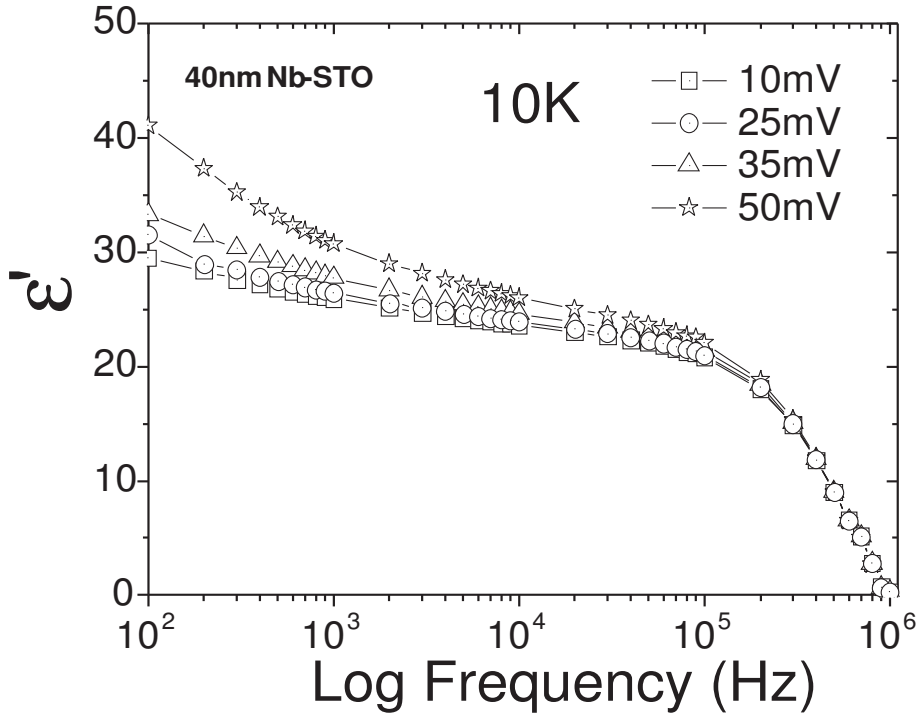

Figure 5.12: *dielectric constant versus frequency for different applied ac field ranging from 10mV to 50mV. The data were taken at 10K.*

of depletion layers.

Indeed, the ac behaviour of a Schottky contact is dependent on the depletion width for a given voltage [154]. The depletion width can be expressed as W=$\sqrt{[2\epsilon_s(V_{bi}\text{-}V_A)/qN]}$, where V_{bi} is the built-in voltage in the Schottky contact, V_A is the applied voltage and ϵ_s is the permittivity of the semiconductor. In turn, the capacitance of the junction (C_j) can then obtained by ϵ_s/W and it follows that the depletion width being dependent on the applied bias, the capacitance of the junction will be modified and thus will be the permittivity of the sample.

5.5.3 Magnetoelectric properties of the $TbMnO_3$ films.

Figure 5.13 shows the temperature dependence of the real part of the dielectric constant as a function of temperature under different applied magnetic fields ranging from 0Oe to 60kOe, and measured at 1kHz for the 90nm film.

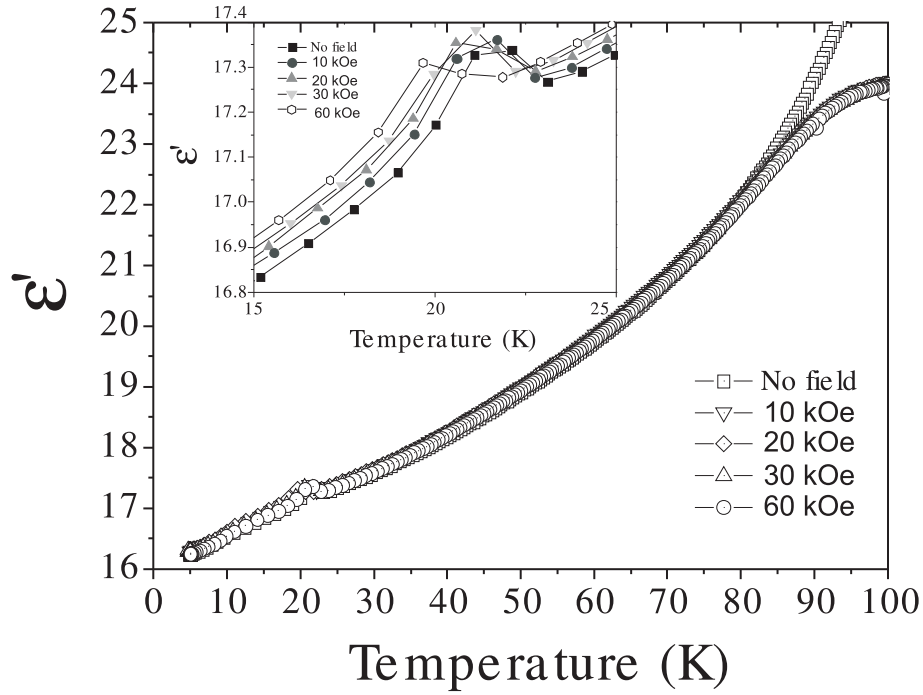

Figure 5.13: *Temperature dependence of the real part of the dielectric constant under different applied magnetic field, from 0 kOe to 60kOe, measured at 1kHz for the 90nm film. The inset shows a zoom around the ferroelectric transition temperature.*

From the graph, no influence of the applied field on the behaviour of the real part of the dielectric constant can be observed up to 80K, where the behaviour of the curves under applied magnetic fields starts differing from that of the curved measured without applied field. This can be attributed to the effect of the applied magnetic field on the polaron hopping. The temperature of the ferroelectric anomaly is lower than the one depicted in figure 5.5, but this may be explained by the use of different set-ups and heating rates. The inset of figure 5.13 shows a blow-up around the ferroelectric transition. The amplitude of the anomaly, related to the onset of local ferroelectricity, is not affected by magnetic fields up to 60 kOe. A small increase of the real part of the dielectric constant with increasing magnetic field can be seen. The temperature of the transition is not affected by fields up to 30kOe, but is shifted to lower temperature under an applied field of 60 kOe. This suggests that high enough magnetic fields tend to preclude the onset of ferroelectricity in the films.

A frequency dependence of the dielectric constant for different field and temper-

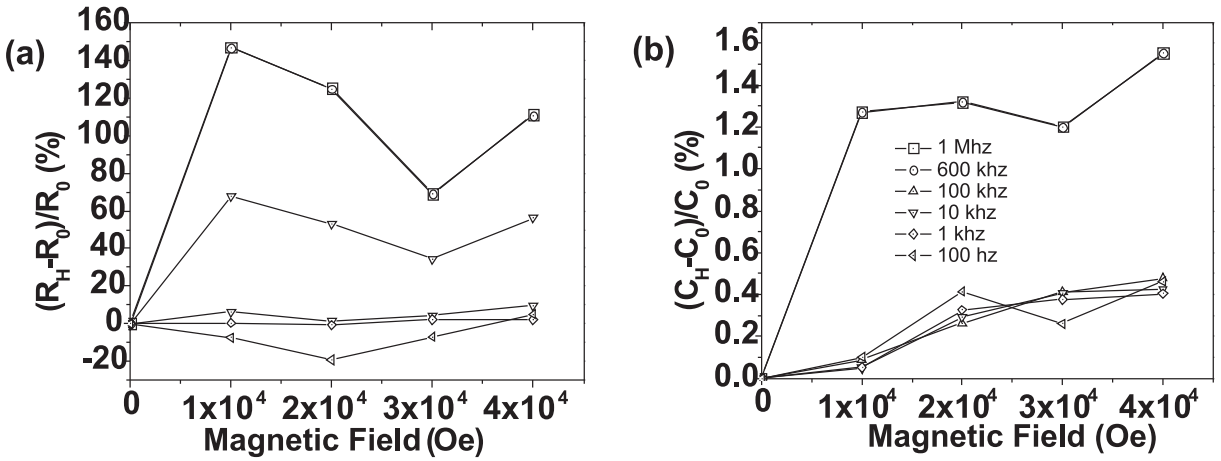

Figure 5.14: *(a): Resistance versus applied magnetic field for a 90nm $TbMnO_3$ thin film grown at 0.9mbar at different frequencies. (b): Capacitance versus applied magnetic field under different frequencies for a 90nm $TbMnO_3$ thin film grown at 0.9mbar. The data were taken at 5K*

atures was performed. Figure 5.14 shows the magnetoresistance (a) and magnetocapacitance (b) measurements for the 90nm film, as a function of frequency, ranging from 100Hz to 1MHz, measured at 5K, to reduce the influence high temperature relaxation. It can be seen that the magnetocapacitance is a small effect in the film and it is significant only for frequencies above 100kHz, with a magnetocapacitance effect of only 1.6%. However, the magnetoresistance effect is much larger: A small negative magnetoresistance of -20% for an applied field of 20 kOe can be observed at a frequency of 100Hz. By increasing the frequency to 1kHz, no magnetoresistance effect can be seen at any applied magnetic field. By further increasing the frequency, a positive magnetoresistance effect of more than 100% can be observed. The magnetoresistance and magnetocapacitance effects seem to saturate for frequencies above a couple of 100kHz, when the relaxation, attibuted to the domain walls starts occuring.

One has to be careful with the interpretation of magnetic field dependence of the dielectric properties. Catalan showed that a magnetocapacitance effect can be observed without a magnetoelectric coupling, due to heterogeneity in the material (Maxwell-Wagner effect) [144]. The magnetocapacitance can be due to colossal magnetoresistance at interfaces (between grains or at domain walls, for example). In the case of

	MR+	MR-
MC+	ID	CD
MC-	CD	ID

Table 5.1: *Core-dominated (CD) and interface-dominated (ID) magnetocapacitance (MC) corresponding to the sign of magnetoresistance (MR) effect as a function of their signs.*

a core-dominated negative magnetoresistance, a positive sign of the magnetocapacitance should be observed, whereas an interface-dominated negative magnetoresistance effect is expected to induce a negative magnetocapacitance [144]. The opposite should be true for a positive magnetoresistance (see table 5.1).

In our data, a positive magetoresistance effect is observed over a wide range of frequencies, associated to a positive magnetocapacitance, indicating an interface dominated magnetoresistance. The most likely candidates are the grain boundaries and/or the presence of domain walls

As discussed above, with decreasing frequency, the magnetoresistance decreases and becomes negative for frequencies below 1kHz, but is still associated with a positive magnetocapacitance, suggesting an core-mediated negative magnetoresistance (see table 5.1). That could arise from the effect of the magnetic field on the polaron hopping. The magnetoresistance and the magnetocapacitance of the 90nm film was measured under different temperatures under a frequency of 1kHz, as shown in figure 5.15 (a) and (b). Under those conditions, the contribution to the magnetocapacitance from the relaxation of the domain walls is minimized to emphasize the core mechanism. The small positive magnetocapacitance (see figure 5.14) decreases with increasing temperature and becomes negative around the ferroelectric transition temperature (T_f 25K). This is still associated to a positive magnetoresistance. From table 5.1, this implies that the magnetoresistance is core-dominated. The change of sign of the magnetocapacitance from positive to negative as also been observed in $TbMnO_3$ with 2% calcium doping on the rare-earth site, at the ferroelectric transition of 20.5K [146].

In short, in $TbMnO_3$ thin films, a strong influence of domain walls on the dielec-

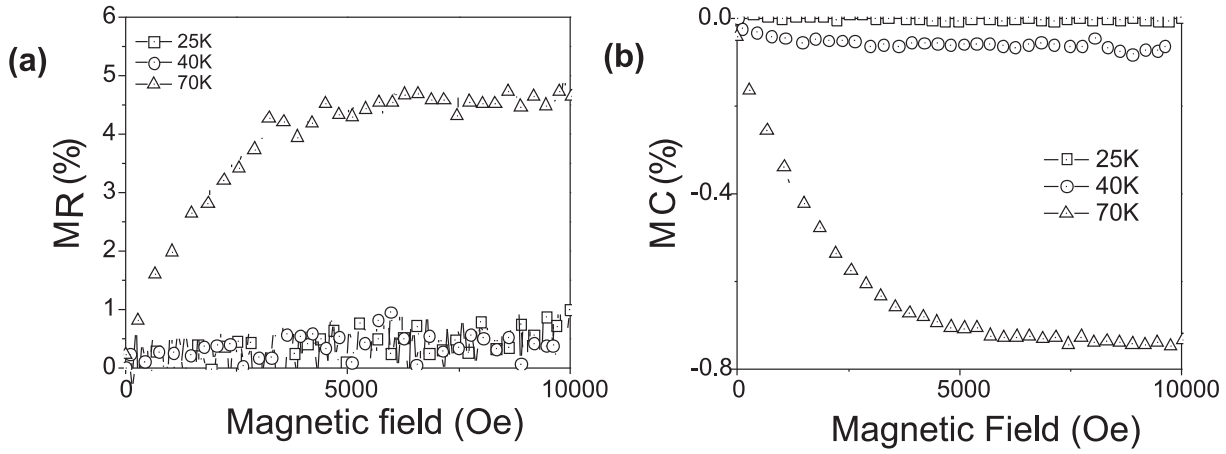

Figure 5.15: *Magnetoresistance (a) and magnetocapacitance (b) dependence under applied magnetic field up to 10 kOe, measured at different temperature from 25K to 70K under an applied frequency of 1kHz.*

tric properties of the films has been evidenced. As suggested by Catalan, for undoped manganites, the intrinsic magnetocapacitance is likely to originate from the magnetoresistance effect and seems to be a small effect. The magnetoresistance in our films has been found to be as large as 150%, at the high frequency relaxation, and to originate at the interfaces (grain boundaries or domain walls).

5.6 Conclusions

A detailed analysis of the dielectric permittivity in the films has allowed the distinction between the different contributions to the dielectric constant. In the strained films, the low frequency dielectric constant at low temperatures is found to be ∼30 at low temperatures, similar to the reported bulk value. This suggests that, despite the absence of long-range ferroelectricity (which would show as an anomaly in the dielectric constant at ≈25K), the strained films seem to contist of polar domains, with polarization at the local scale. The main extrinsic contribution to the low frequency response can be attributed to polaron hopping probably induced by charges in depletion layers at the different interfaces present in the films.

The domain walls largely contribute to the dielectric constant and relax at about

10^5-10^6 Hz. The relaxation of domain walls is shifted to higher frequencies in the case of the partially-relaxed film. This is most likely due to a release of the clamping effect of the substrate. Moreover, the domain relaxation mechanism does not follow an Arrhenius law. However, the inverse of the relaxation times follows a linear behaviour versus temperature up to around 25K, where the behaviour departs from the linear one, suggesting the presence of the sinusoidal to cycloid transition in the films (at the local scale) and consistent with the presence of ferroelectricity.

The 90nm film shows a small magnetocapacitance effect of 1%, whereas a magnetoresistance effect as high as 150% could be measured under an applied field of 60 kOe along the in-plane direction, at 5K, at frequencies at which the relaxation of domain wall starts appearing. Under such an applied field, we find that the ferroelectric transition is shifted to slightly lower temperatures, confirming an intrinsic magnetoelectric coupling, even if the effect is small.

Chapter 6

$TbMnO_3$ films grown on $SrRuO_3$-buffered (001)-$DyScO_3$ substrates

6.1 Abstract

In this chapter, we present the structure and properties of $TbMnO_3$ perovskite thin films on single crystals of (001)-oriented $DyScO_3$. (001)-$DyScO_3$ was chosen because it has the same space group and similar lattice parameters as $TbMnO_3$, it is commercially available and it can be prepared to have atomically flat surfaces. Because this substrate's orientation has been used in this thesis for the first time, we dedicate a section to explain the treatment procedure to lead to atomically-flat surfaces. The $TbMnO_3$ films were grown with a buffer layer of $SrRuO_3$ in order to perform the dielectric characterization of the films. By using different growth conditions and thicknesses of the buffer layer, the relaxation of $SrRuO_3$ could not be prevented, and the $TbMnO_3$ films were found to be under compressive strain determined by the $SrRuO_3$ layer. Under these conditions, epitaxial $TbMnO_3$ films were successfully deposited with the (001)-orientation with different buffer layers grown under different conditions and with different morphology. Unlike for the growth on $SrTiO_3$ substrates, the films follow a typical strain relaxation characterized by the gradual evolution of the out-of-plane lattice parameter toward the bulk value. The dielectric characterization of the films shows no clear influence of the relaxation mechanisms associated to the domain walls that were so prevalent in the case of the films grown on $SrTiO_3$ sub-

strates.

6.2 Introduction

The structure and properties of orthorhombic $TbMnO_3$ films grown on $SrTiO_3$ were studied in the previous chapters. We have found that the orthorhombicity of the $TbMnO_3$ films can be tuned by changing the thickness of the layers. The films contain four domain variants with the same out-of-plane (001)-orientation. The strain relaxes suddenly at a thickness that depends on the oxygen pressure during deposition. The films show predominant antiferromagnetic interactions, but a net magnetic moment arises below the antiferromagnetic transition temperature, which is observed as a split between the field-cooled (FC) and zero-field-cooled (ZFC) magnetization versus temperature curves. Other recent works in antiferromagnetic manganite thin films have also reported ZFC-FC splitting in the magnetization curves, but the origin is still unknown. Motivated by the possibility of a general mechanism for the observed ferromagnetism in antiferromagnetic thin films, we have dedicated considerable effort to elucidate the origin of the ferromagnetism in our $TbMnO_3$ films.

In bulk samples, there is an anomaly in the dielectric constant related to the onset of ferroelectricity, which is in turn related to the transition from the sinusoidal to the spiral spin state. In the fully strained $TbMnO_3$ films grown on $SrTiO_3$, no anomaly in the dielectric constant was found. This points to the disappearance of the macroscopic ferroelectric order and the long range spiral ordering, and may be explained by the small size of the crystallographic domains present in the films. Since we have observed a change in the slope of the temperature dependence of the relaxation time at the bulk ferroelectric temperature, $T_C \approx 27$K, we postulate that short-range order, with similar local structure to the one of the bulk structure, is present.

Despite the interest of the previously studied films, it would also be desirable to obtain domain-free films with macroscopic properties resembling those of multiferroic

$TbMnO_3$ single crystals. Thus, in order to have a better control on the orthorhombic structure of $TbMnO_3$, and to investigate its intrinsic properties, a different substrate was chosen: Orthorhombic (001)-oriented $DyScO_3$. This material has been recently synthesized in single crystal form and its (110)-orientation has already been used for thin film growth of ferroelectric materials because it provides a pseudo-cubic lattice with lattice parameter of 3.95 Å. In our case, the motivation for choosing (001)-$DyScO_3$, among all commercially available substrates, is different and three-fold: First, the lattice parameters of $DyScO_3$ are close to those of $TbMnO_3$, as shown in figure 6.1 (a)-(b); second, because film and substrate are both orthorhombic, the presence of crystallographic domains is not foreseen; and third, atomically flat surfaces with terrace-step morphology can also be obtained, as in the case of $SrTiO_3$, leading to a high quality interface and a better control of the growth. This makes the (001)-oriented $DyScO_3$ a very interesting substrate for epitaxial stabilization of $TbMnO_3$ and a promising candidate for the manipulation of the spiral state of $TbMnO_3$.

From the lattice parameters of both $DyScO_3$ and $TbMnO_3$, the mismatch strain along the $[100]_o$ direction, given by $u_m = (a_{substrate} - a_{bulk})/a_{substrate}$, is around 2.9%, compared to 4% along the same direction, $[110]_c$, of $SrTiO_3$. The mismatch in the $[010]_o$ direction is -1.9% in the case of $TbMnO_3$ on $DyScO_3$, compared to -5.7% in the case of $TbMnO_3$ on $SrTiO_3$. This means that in both cases, the a-direction of $TbMnO_3$ is under tensile strain whereas the b-direction of $TbMnO_3$ is under compressive strain, although the epitaxial strain is substantially smaller in the case of $DyScO_3$ substrates. Looking at the overall epitaxial strain, $TbMnO_3$ should be under overall tensile strain on $DyScO_3$ and under overall compressive strain on $SrTiO_3$.

In this final chapter, we will describe the first attempts to growth $TbMnO_3$ films on (001)-$DyScO_3$. We will describe the growth and the structure of the films and their dielectric behavior. Although sample optimization is still needed, the results show that the microstructure of the film and the associated properties, which highly determine the dielectric relaxation processes, can be controlled to a very high extent by the choice of substrate.

(a)

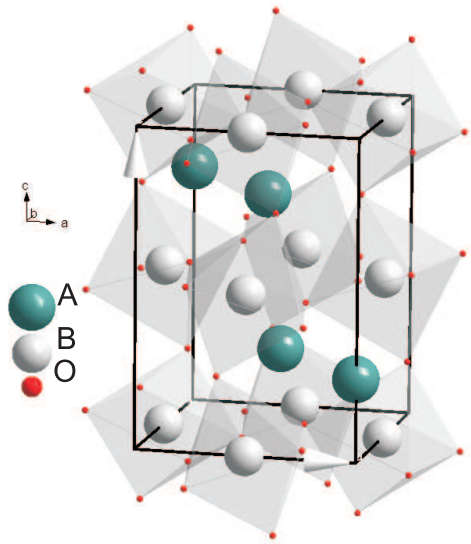

(b)

$DyScO_3$: Pbnm
a = 5.554 Å
b = 5.7263 Å
c = 7.9132 Å

Atom	x/a	y/b	z/c
A=Dy	0.9828	0.06070	0.25
B=Sc	0.5	0	0
O1	0.11960	0.44500	0.25
O2	0.69260	0.30400	0.06080

$SrRuO_3$: Pbnm
a = 5.5328 Å
b = 5.5693 Å
c = 7.8471 Å

Atom	x/a	y/b	z/c
A=Sr	0.981	0.017	0.25
B=Ru	0.5	0	0
O1	0.046	0.498	0.25
O2	0.723	0.276	0.029

$TbMnO_3$: Pbnm
a = 5.2931 Å
b = 5.8384 Å
c = 7.4025 Å

Atom	x/a	y/b	z/c
A=Tb	0.9836	0.0810	0.25
B=Mn	0.5	0	0
O1	0.1083	0.4694	0.25
O2	0.7085	0.3267	0.05230

Figure 6.1: *Sketch of one unit cell of $DyScO_3$, $TbMnO_3$ and $SrRuO_3$ (a), along with their lattice parameters and atomic positions.*

6.3 Growth and structural characterization

6.3.1 Substrate treatment

There are, as far as we know, no previous reports using this orientation of $DyScO_3$ substrates for thin film deposition. Therefore, we will report the substrate treatment in detail.

The (001)-oriented $DyScO_3$ substrates were provided by CrysTec GmbH (Berlin, Germany). Prior to deposition, they were thermally treated after cleaning with acetone and ethanol. The optimized thermal treatment consisted of heating the substrates to 1020^{o}C with a rate of around 20^{o}C/min for 12.5h under and oxygen flow of around 300mm^3/min. The duration of the thermal treatment is a crucial parameter. Figure 6.2 shows AFM images of 3 different $DyScO_3$ substrates which were heated during 11h

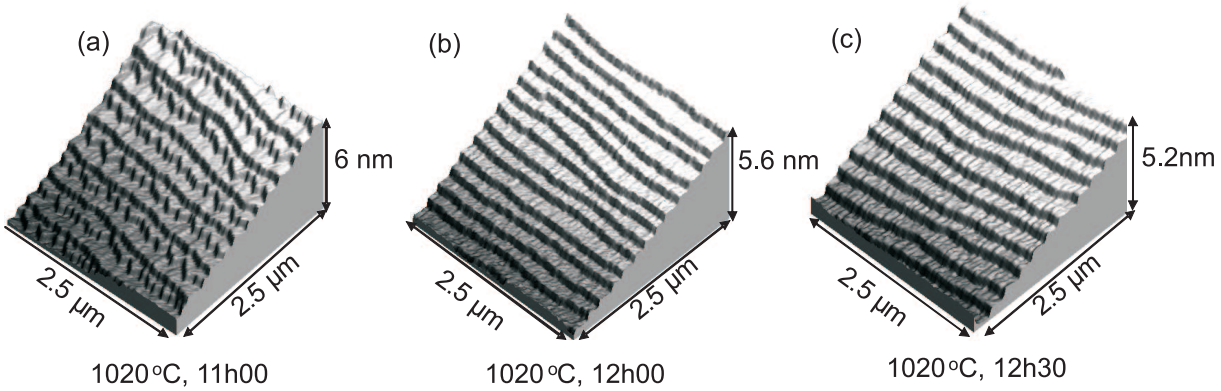

Figure 6.2: *AFM images of (001)-oriented $DyScO_3$ substrates treated for 11h (a), 12h (b) and 12.5h (c). In order to better appreciate the morphology, a 3D view of the measured AFM images, using the WSXM software [155], is presented. The 2D images corresponding to a) and c) are shown in figures* 6.3*(a) and (b), respectively.*

(a), 12h (b) and 12.5h (c). Figure 6.2 (a) shows terraces with a specific pattern: only one step out of two shows a straight edge. However, substrates treated during 12h and 12.5h show straight steps. A more careful look reveals that the steps for the substrates treated for 12.5h are more regularly spaced than the steps of the substrates treated for 12h.

By taking a line profile, as shown in figure 6.3 (c), it becomes clear that the substrate showing the irregular terraces (a), has alternating steps of $\sim 4\mathring{A}$ and $\sim 8\mathring{A}$, corresponding to a half unit cell and a full unit cell of $DyScO_3$, respectively. However, for the substrate treated for 12.5h and showing terraces with parallel edges (figure 6.3 (b) and (d)), only steps of 1/2 unit cell are observed. This shows that, indeed, the (0 0 1) and (0 0 2) planes of $DyScO_3$ are not structurally identical and that diffusion is somewhat easier for one of them. However, because the two planes have the same chemical composition (they correspond to the (0 0 1) planes of a simple perovskite unit cell), a longer thermal treatment is likely to provide steps having equally a height of one unit cell.

It is important to note that this optimized time is only valid for $DyScO_3$ substrates having a similar miscut to the one used in this thesis ($\sim 0.1^o$), which corresponds to a terrace length of about 200nm. The effect of the miscut on the heat treatment of the

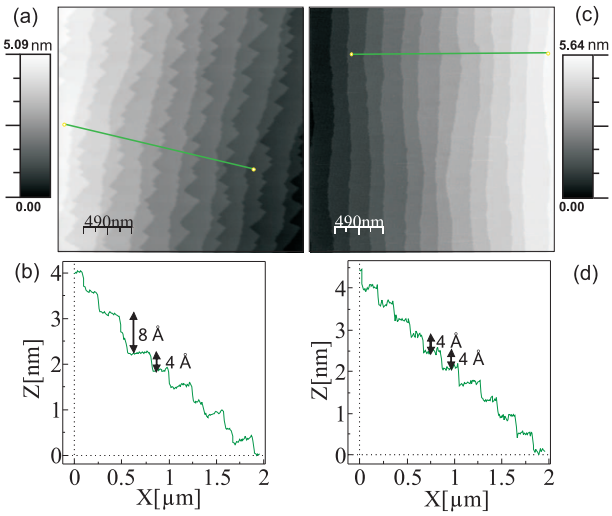

Figure 6.3: *(a) AFM image of a (001)-oriented $DyScO_3$ substrate treated for 11h. (b) Profile along a line taken perpendicular to the steps of (a). (c) AFM image of a (001)-oriented $DyScO_3$ substrate treated for 12.5h. (d) Profile along a line taken perpendicular to the steps of (b).*

substrate is not the scope of this thesis and will not be discussed here.

6.3.2 Growth conditions

In this section, the growth of $TbMnO_3$ films on (001)-oriented $DyScO_3$ substrates will be shortly described. Prior to the deposition of $TbMnO_3$, a buffer layer of $SrRuO_3$ was grown to be used as a bottom electrode for the dielectric characterization. The $SrRuO_3$ thin films were grown at two different temperatures, 600^{o}C and 700^{o}C, under an oxygen pressure of 0.13mbar. The frequency of the laser pulses was set to 1Hz with a laser energy density at the target of 2Jcm^{-2} per pulse. The distance between target and substrate was 58mm. $TbMnO_3$ was subsequently deposited under the same conditions as those used for the films on $SrTiO_3$: At a temperature of 750^{o}C, under an oxygen pressure of 0.9mbar, with a laser frequency and energy density of 1 Hz and 2J.cm^{-2}, respectively, and a target-substrate distance of 55mm. The deposition was stopped after one hour of growth, aiming to a $TbMnO_3$ film thickness of $\sim$40nm, estimated from the growth rate of the samples on $SrTiO_3$. After the growth of $TbMnO_3$, 100mbar of oxygen was inserted in the deposition chamber and the sample was then cooled

down to room temperature at a rate of 3^{o}C.min^{-1}.

6.3.3 $SrRuO_3$ growth

Figure 6.4 (a) shows the RHEED image of a (001)-oriented $DyScO_3$ substrate, showing the excellent quality of the surface of the substrate. By using a deposition temperature of 700^{o}C, atomically flat $SrRuO_3$ with a thickness of around 6nm was deposited, as shown in figure 6.4(b), where the RHEED pattern exactly resembles that of the substrate, indicating that 2D growth takes place at this temperature. This thickness of 6 nm is thick enough to be above the metal-insulator transition observed for $SrRuO_3$ films of about 6 monolayers (slightly thinner than 5nm) and thin enough to display a decreased magnetic moment, which saturates at 15 monolayers (around 11nm) [156].

For a growth temperature of 600^{o}C, the growth of $SrRuO_3$ on (001)-oriented $DyScO_3$ is similar to that reported for the growth of $SrRuO_3$ on (111)-$SrTiO_3$ [157]: The initial stage of growth is 3D (island-like) and the films flatten after a certain thickness of the $SrRuO_3$ layer of about 30 nm. Under these growth conditions, the deposition was stopped at the beginning of the 3D-to-2D transition, in order to have a $SrRuO_3$ layer as thin as possible. The deposition was stopped after a time estimated to give a thickness of around 30nm. After the growth of such layer, the RHEED pattern consists of a mixed pattern of weak streaks at the positions of the substrate spots, indicating a 2D morphology with certain disorder, along with extra spots, characteristics of 3D islands, as shown in figure 6.4 (c).

The growth of $TbMnO_3$ at an oxygen pressure of 0.9mbar after the $SrRuO_3$ growth cannot be followed by RHEED due to a very low signal-to-noise ratio, but the effect of the electrode layer on the morphology of the $TbMnO_3$ films will be discussed in the next section.

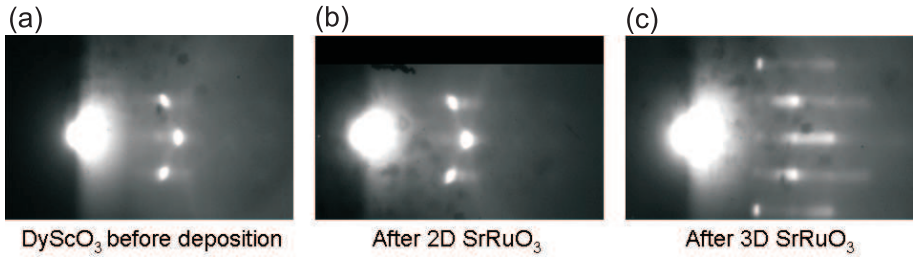

Figure 6.4: *RHEED images of a treated (001)-oriented $DyScO_3$ substrate before deposition (a), after the deposition of $SrRuO_3$ with an initial 2D growth (b), and after the deposition of $SrRuO_3$ with an initial 3D growth (c).*

6.3.4 Morphology and structure of the films

Figure 6.5 (a) shows an AFM image for the sample grown on a 6nm 2D $SrRuO_3$ layer. The image shows deep ridges between groups of columns or grains. This could be a consequence of the morphology of the underlying $SrRuO_3$, which most likely has a mound-like (or wedding-cake-like) morphology [158]. The total RMS roughness of the image in 6.5(a) is 3.5nm, but the roughness of an area without ridges is $\sim$1nm, close to 1 unit cell. Figures 6.5 (b) and (c) show the profiles along a line that does not cross a ridge and a line that crosses a ridge, respectively. Figure 6.5 (c) shows that the ridges can be as wide as 100nm at the surface. However, the ridge depth is not comparable to the thickness of the film, so the ridges do not seem to reach the $SrRuO_3$ layer, which would create a conduction path. As displayed in figure 6.5(d)-(e), the sample in which the $SrRuO_3$ electrode is thicker and had an initial 3D growth (from now on called 3D $SrRuO_3$) shows a more uniform morphology at the surface but still a high RMS roughness of 3.9nm.

The lattice parameters of a bulk $SrRuO_3$ are shown in figure 6.1. The mismatch strain with the substrates along [100] is 1.5% compressive, while along [010] it is 3.3% tensile. It is reasonable to assume that the 30nm 3D-$SrRuO_3$ layers are completely relaxed. On such template, the $TbMnO_3$ films would grow under compressive strain (see figure 6.1) and the out-of-plane lattice parameter of a fully strained $TbMnO_3$ film is estimated to be around 7.44$\mathring{A}$ (simply using volume conservation considerations). This value agrees very well with the one we find for a 10nm thin film of $TbMnO_3$ grown

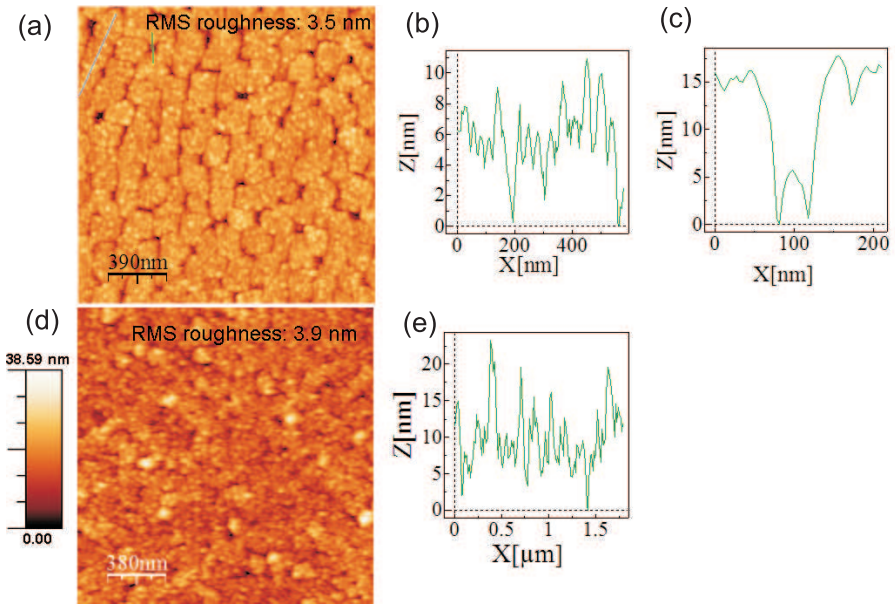

Figure 6.5: *(a) AFM image of the $TbMnO_3$ sample with a 6nm buffer layer of $SrRuO_3$. (b) Profile along a line in (a) that does not cross a ridge. (c) Profile along a line in (a) that crosses a ridge. (d) AFM image of the $TbMnO_3$ sample with a 30nm buffer $SrRuO_3$ layer. (e) Profile along a line randomly chosen in (d).*

on the 30nm 3D-$SrRuO_3$ layer, as shown by the (002) diffraction peaks of figure 6.6. A 40nm thick film grown on a similar $SrRuO_3$ layer is also plotted in the same graph. The slightly smaller lattice parameter of the 40nm film (c= 7.42$\mathring{A}$) indicates that strain relaxation of the film has began at this thickness and that, indeed, the strain is compressive. In order to confirm this, a reciprocal space map around the (116) reflection of $DyScO_3$ is shown in figure 6.7. It is evidenced that the 40nm film is not fully coherent with the substrate since they do not share the parallel component of the scattering vector (K_{par}), confirming the relaxing character of this $TbMnO_3$ layer.

Thus, our results are consistent with the $TbMnO_3$ films growing compressively strained on a relaxed $SrRuO_3$ layer. In order to confirm this possibility, reciprocal space mapping was used to detect the $SrRuO_3$ layer, which is difficult to observe in the 2θ-ω scans due to its proximity with the substrate peak. A reciprocal space map around the (002) of $DyScO_3$ is shown in figure 6.8 for a 40nm $TbMnO_3$ film grown on a 30nm 3D-$SrRuO_3$ layer. The peak associated with the $SrRuO_3$ layer can now clearly be seen thanks to

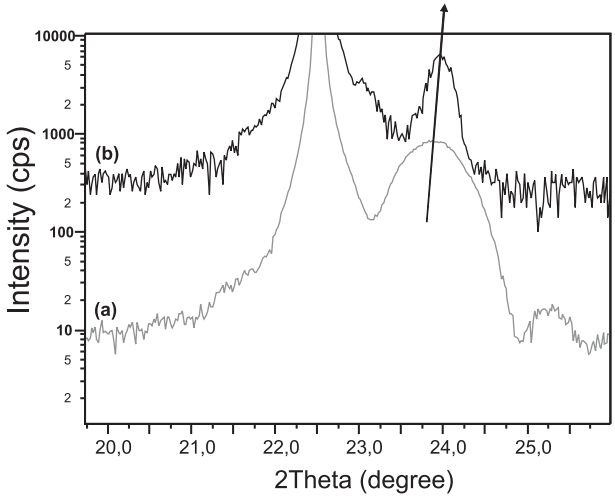

Figure 6.6: *X-ray diffraction 2θ-ω scans around the (002) reflections of a 10nm (a) and a 40nm (b) $TbMnO_3$ film. Both films were grown with a 30nm $SrRuO_3$ layer that initially grew in 3D mode and flattened during the growth.*

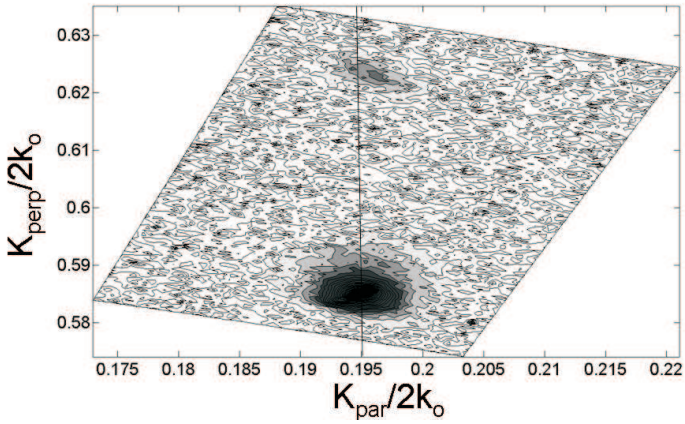

Figure 6.7: *Reciprocal space map taken around the (116) Bragg peak of $DyScO_3$. The film's peak corresponds to the peak at larger K_{perp} in the map, whereas the substrate's peak corresponds to the spot at smaller K_{perp}. The $SrRuO_3$ peak is too weak to be observed in this map*

the diffuse scattering. From its position, an out-of-plane lattice parameter of around 7.84$\mathring{A}$ was found, consistent with a relaxed $SrRuO_3$ layer at this thickness.

X-ray diffraction 2θ-ω scans around the (002) and (004) reflections are shown in figure 6.9 for the $TbMnO_3$ film grown with a thin 2D $SrRuO_3$ buffer layer. Although the quality of the patterns is not as good as those of the samples grown on $SrTiO_3$ (and without buffer layer) in chapter 3, Laue fringes are also present, indicating relatively good interfaces, better than those of the samples grown with 3D $SrRuO_3$ layers, as

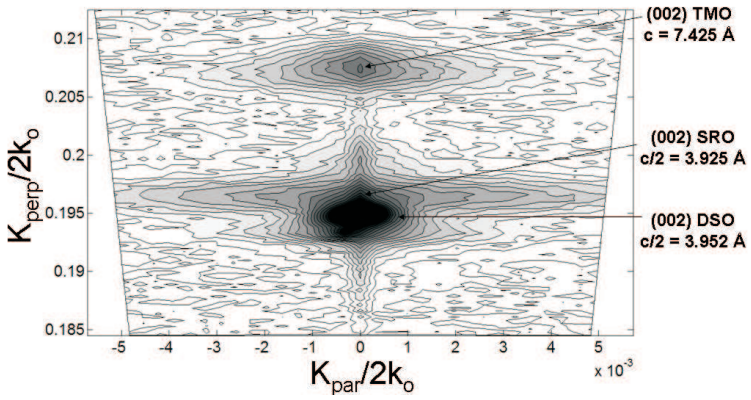

Figure 6.8: *Reciprocal space map around the (002) Bragg peak of the $DyScO_3$ substrate for a 40nm $TbMnO_3$ film grown on a $SrRuO_3$ layer that showed initial 3D growth.*

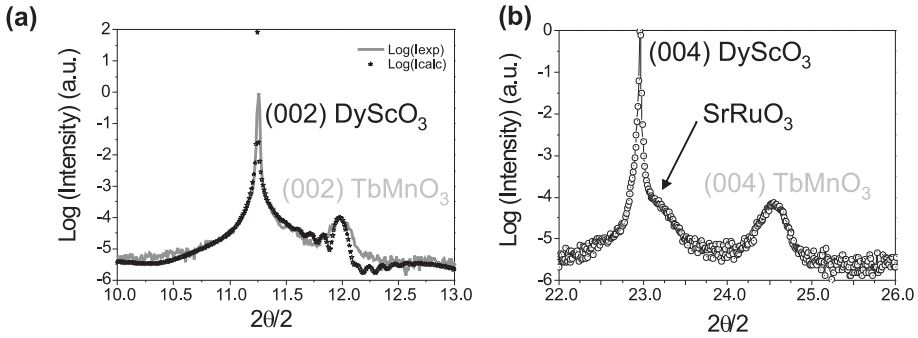

Figure 6.9: *Regions of the 2θ-ω x-ray diffraction patterns around the (002)(a) and (004)(b) reflections, for the 40nm $TbMnO_3$ film grown with a thin 2D $SrRuO_3$. The experimental data are shown as a grey line and the fit to the data is shown a black stars in (a). Only the experimental data are shown in (b).*

expected. The thickness of the $TbMnO_3$ film could be measured from the oscillations of the reflectivity curve (not shown here), and it was found to be 40nm, as expected from the growth time.

From the fit of the (002) reflection shown in 6.9(a), the substrate and the $SrRuO_3$ could be well matched (see black stars) but the fit deviates from the data on the right-hand side of the $TbMnO_3$ peak. This is probably due to some strain relaxation, not taken into account in the model. An out-of-plane lattice parameter of $\sim 7.42\mathring{A}$ was used for fitting the position of the $TbMnO_3$ peak. This value is not consistent with the smaller out-of-plane lattice parameter, compared with the bulk $\sim 7.40\mathring{A}$, expected for a film under overall tensile strain, but it is the same value found for a film of the same

thickness (40nm) grown on the 3D-$SrRuO_3$ buffer layer, as previously discussed. We therefore postulate that, unexpectedly, the 2D $SrRuO_3$ buffer layer is relaxed already at this very low thickness of 6nm.

Thus, although we have successfully stabilized $TbMnO_3$ on $SrRuO_3$ buffered (001)-oriented $DyScO_3$, we believe that the electrode layer does not grow coherent with the substrate and, therefore, the epitaxial strain could not be transferred from the substrate to the $TbMnO_3$ film, even in the films with a very thin and flat electrode layer.

6.4 Physical properties

6.4.1 Magnetic behaviour

The paramagnetic contribution of the $DyScO_3$ substrate dominates the signal and clear magnetic information cannot be obtained from the films. However, the inverse susceptibility of the ZFC curve seems to indicate different magnetic transitions reflected by the change of slope. The measure of the magnetic moment, under zero-field-cooled conditions, for a 40nm $TbMnO_3$ film grown on a 30nm $SrRuO_3$ (with an initial 3D growth) is shown in figure 6.10.

Looking at the low temperature region, as shown in figure 6.10, the data does not seem to depart from this linear behavior for this range of temperatures. This reflects the possible absence of magnetic transition (or too weak to be observed) in the film or the possibility that the transition has been shifted to higher temperatures. As shown in the inset of figure 6.10, where the inverse susceptibility for the full range of temperatures, from 5K to 300K, is shown for a 40nm thick film grown on a 3D $SrRuO_3$ layer, a change of slope of the inverse susceptibility (χ^{-1}) with respect to the high temperature linear fit can be seen for a temperature around 150K. This seems to indicate the onset of the ferromagnetic transition of $SrRuO_3$, which occurs at 150K with a magnetic moment of $\sim$1.5μ_B/Ru atom [159, 160]. However, the inverse susceptibility should evolve below the paramagnetic line, in the case of a ferromagnetic transition, instead

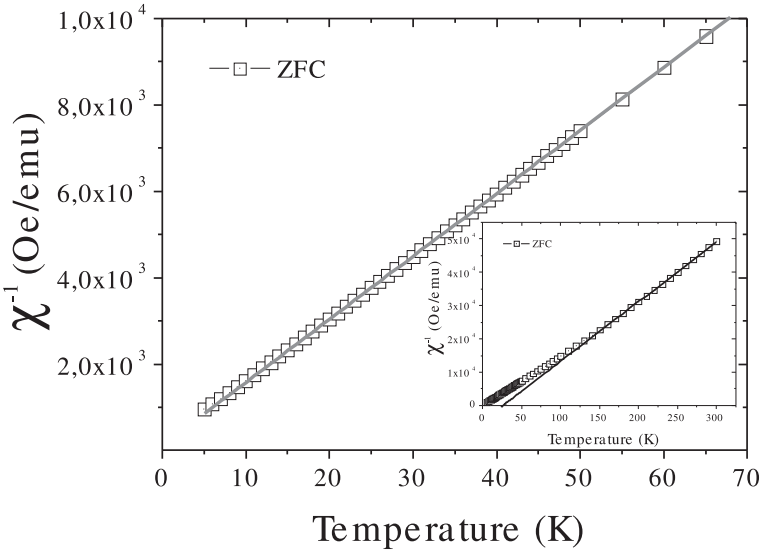

Figure 6.10: *Inverse magnetic susceptibility as a function of temperature, ranging from 5K to 70K, for a 40nm $TbMnO_3$ thin film grown on a $DyScO_3$ substrate buffered with a $SrRuO_3$ layer initially grown in 3D mode. The line is a guide to the eyes. The inset shows the full range of temperatures from 5K to 300K. The line shows a linear fit to the data in the high temperature range.*

of above the paramagnetic line, as observed in the inset. This suggests that the transition observed is antiferromagnetic-like and might be associated with the manganese ordering of $TbMnO_3$. However, the Curie-Weiss fir gives a positive Curie-Weiss temperature, suggesting dominant ferromagnetic interactions. Further experiments are required to clarify these observations.

6.4.2 Dielectric behaviour

The dielectric behaviour of the 40nm films grown on $DyScO_3$ with buffer layers of $SrRuO_3$ has been characterized. Figure 6.11 shows the frequency dependence of the capacitance for both 40nm thin samples grown with a 3D $SrRuO_3$ layer(a) and a 2D-$SrRuO_3$ layer (b), at different temperatures. The behavior is very different in both cases: A temperature-dependent dielectric relaxation, in the range of frequencies from 10^2-10^5 Hz occurs in the sample grown on 3D $SrRuO_3$, whereas a relaxation at lower frequencies about 10-100 Hz, which is independent of temperature, occurs in the film

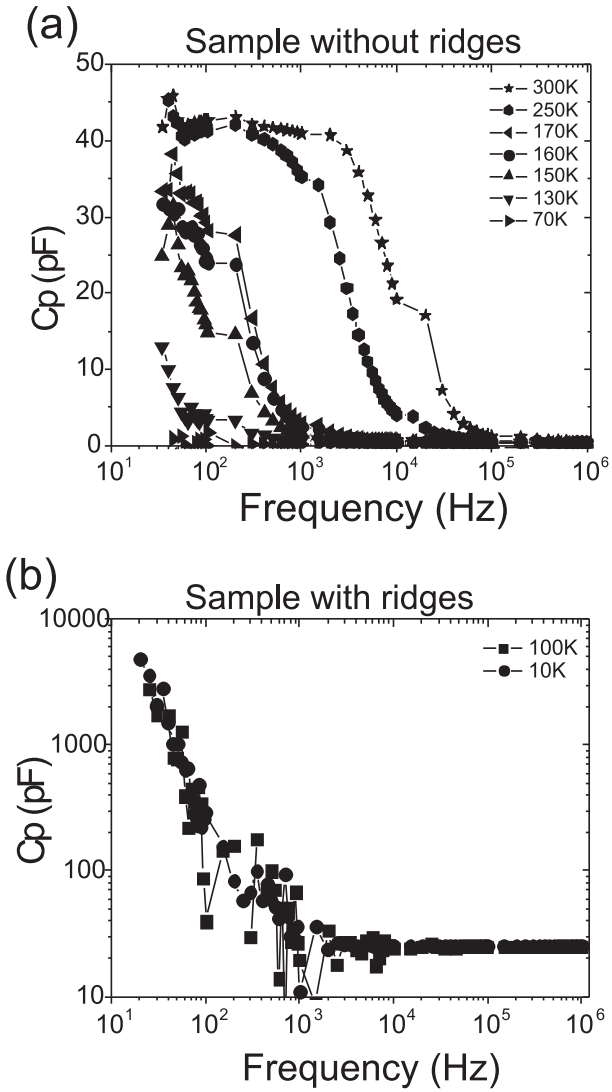

Figure 6.11: *(a) Frequency dependence of the capacitance, at different temperatures ranging from 70K to 300K, of a 40nm film grown on $DyScO_3$ with a buffer layer of 3D $SrRuO_3$. (b)Similar plot at temperatures of 10K and 100K for a 40nm $TbMnO_3$ film grown on $DyScO_3$ with a 2D $SrRuO_3$ buffer layer.*

grown on a 2D $SrRuO_3$ layer. Moreover, the film grown on 2D $SrRuO_3$ shows a very large low-frequency capacitance. This could be explained by an interface contribution at the sample ridges.

As explained in the previous chapter for the films on Nb-$SrTiO_3$, according to the universal dielectric response (UDR), localized charge carrier hopping not only contributes to the conductivity but also to the polarizability [152]. According to that model,

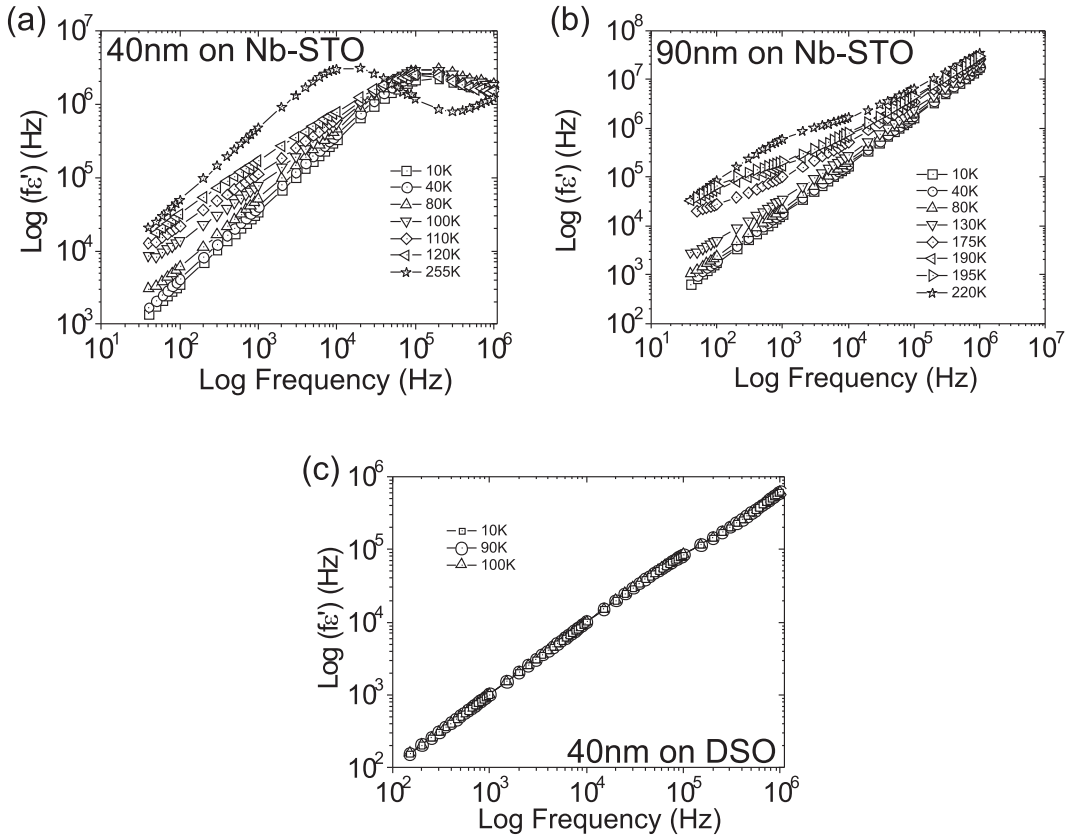

Figure 6.12: *log (fϵ') versus log f for different temperatures for a 40nm film grown on Nb-STO (a), a 90nm film grown on Nb-STO (b) and a 40nm film grown on 2D-$SrRuO_3$-buffered $DyScO_3$ (c).*

the real part of the dielectric constant can be calculated as ϵ'=tan(sπ/2)σ_of^{s-1}/ϵ_o, where σ_o (dc conductivity) and *s* are temperature dependent and ϵ_o is the permittivity of free space. This can be rewritten as fϵ'=A(T)f^s, where A(T)=tan(sπ/2)σ_o/ϵ_o [152]. Consequently, a plot of log(fϵ') versus log f, at a given temperature, is expected to give a linear behaviour if the material follows the UDR law. Such a plot is shown in figure 6.12 for three samples discussed in this and previous chapter.

We note that a nearly perfect linear dependence can be obtained for the sample on $DyScO_3$ at all temperatures, while in the samples grown on Nb-$SrTiO_3$, the behavior departs from a linear dependence with s= 1 at the intermediate temperatures, where the contribution from domain wall starts appearing.

The s-exponent for the low frequency region is shown in figure 6.13. A clear de-

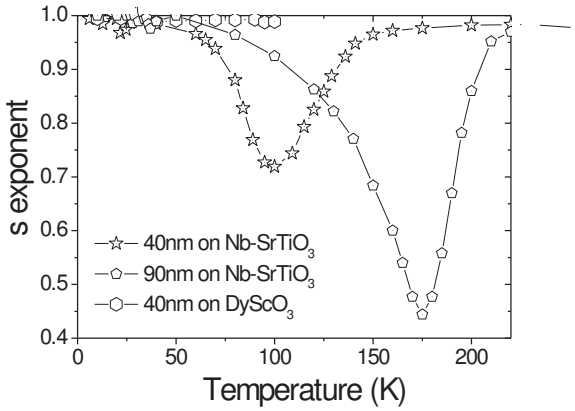

Figure 6.13: *s-exponent as a function of temperature for three different $TbMnO_3$ films discussed in these thesis.*

crease in the *s* exponent can be observed for the films grown on Nb-$SrTiO_3$ substrates. The values of the *s* exponent for the 40nm film vary from 0.7 to 1, in perfect agreement with the UDR law, and have the minimum at 100K. The 90nm film shows a minimum value as low as s= 0.45 at 175K. This s-value is smaller than typical UDR values ($0.6 < s < 1$) and can be explained by the more complex structure of this film, consisting of a strained part and a relaxed part. The *s* exponent in the case of the sample grown on 2D $SrRuO_3$-buffered $DyScO_3$ is very close to 1 and does not vary with temperature, within the range of temperatures measured for this sample.

In the case of the samples on Nb-$SrTiO_3$ substrates, the conduction was assigned to polaron hopping and the data shown here and in the previous chapter for these films are indeed consistent with a thermally-activated process. The film grown on $DyScO_3$, shows a very different behaviour with an exponent s equals to 1 (the conductivity is linearly dependent on the frequency), independent of temperature. Although the microstructure of the films on $DyScO_3$ has not been directly observed, the orthorhombic symmetry of the substrate, electrode and layer precludes the formation of domains and of a large numbers of domain walls, like those observed on the $SrTiO_3$ substrates. Therefore, the conduction processes associated to the domain walls that determined the dielectric properties of the films on Nb-$SrTiO_3$, are not expected in the films on

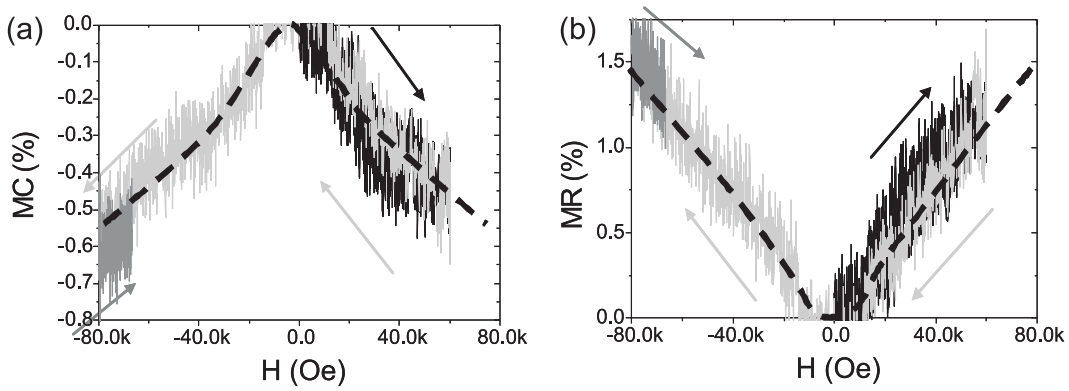

Figure 6.14: *Magnetocapacitance (a) and magnetoresistance (b) as a function of applied magnetic field, ranging from -80kOe to 60kOe, at 15K under an applied frequency of 1MHz for a 40nm $TbMnO_3$ film grown on a 2D $SrRuO_3$ layer on a (001)-oriented $DyScO_3$ substrate.*

$DyScO_3$.

We have also investigated the magnetocapacitance of the sample grown on $DyScO_3$ with a 2D $SrRuO_3$ layer. A frequency of 1MHz was applied to minimize the influence of the interface polarizability on the magnetoelectric properties of the films. Figure 6.14, shows the magnetocapacitance (left) and magnetoresistance (right), measured at 15K, as a function of applied magnetic field. A positive magnetoresistance associated with a negative magnetocapacitance effect have been observed, evidencing the small core-dominated magnetoresistance, similar to that observed for the films on Nb-$SrTiO_3$ below the domain wall relaxation frequency. Both magnetocapacitance and magnetoresistance are small, as already seen for the films on $SrTiO_3$.

6.4.3 Conclusions

We have grown single phase epitaxial films of $TbMnO_3$ on single crystals of (001)-oriented $DyScO_3$, used in this work for the first time, with $SrRuO_3$ electrode layers. However, contrary to our expectations, the $SrRuO_3$ layer is the one that determines the $TbMnO_3$ strain state. Because the substrate, the electrodes and the $TbMnO_3$ film belong to the same orthorhombic space group, domain formation is not expected. However, the high paramagnetic contribution from the substrate hides clear features

in the zero-field-cooled magnetic measurements, making difficult to observe transitions associated with small magnetic moment, as in the case of the antiferromagnetic $TbMnO_3$. This is confirmed by the dielectric measurements that, unlike those of the films on $SrTiO_3$, are not determined by the relaxation/conduction processes at the domain walls. Although thin films under tensile strain imposed by the $DyScO_3$ substrate have not been achieved yet and more work is needed. This study shows progress in that direction and clearly shows that microstructures and domain structures have tremendous effects in the physical properties of a material.

Summary

This dissertation presents the experimental investigation of the structure and physical properties of thin films of the multiferroic $TbMnO_3$ under compressive epitaxial strain. Multiferroic compounds are a class of material exhibiting both spontaneous electrical polarization and magnetization, within the same phase. These materials are rare in nature and efforts are devoted to the discovery/synthesis of new multiferroics. Multiferroics are good candidates to display high magnetoelectric response. This class of materials, in which the electrical and magnetic orders are coupled, has great potential in spintronics or non-volatile 4-state memories. However, the reported couplings are usually too weak to be implemented for applications. Possible ways to enhance the materials' response, are to use an appropriate dopant, to apply an external pressure or to apply epitaxial strain. While the understanding of the fundamental mechanisms related to the appearance of multiferroicity in some materials has greatly improved over the last few years, many theoreticians and experimentalists are working towards finding new systems with enhanced magneto(-di)electric response, or modifying an existing material in an attempt to enhance the magnetoelectric coupling or to create new multiferroics.

The scope of this thesis is to study the role of epitaxial strain on a multiferroic material. We focus on one of the most popular multiferroics, $TbMnO_3$, in which the spontaneous electrical polarization is due to a spiral spin ordering, giving rise to a large magnetoelectric coupling. Moreover, large strain effects can be expected in such system because of the subtle balance between the magnetic interactions and its large magnetic frustration. Despite its interest, no reports on $TbMnO_3$ under epitaxial strain were available at the beginning of our study. We have investigated the structure and

properties of compressively strained thin films of $TbMnO_3$, with thickness below 100nm.

In chapter 1, we introduce multiferroic and magnetoelectric materials and their interest from the fundamental and from the applications point of view, as well as the compound subject of this thesis, $TbMnO_3$, describing the crystallographic and magnetic structure of the bulk material. We motivate the interest of growing thin films of these materials, in general, and of $TbMnO_3$, in particular. Finally, we present several recent reports on epitaxially grown rare earth manganites, specially the manganites that show a splitting between the field-cooled and the zero-field-cooled magnetization curves, absent in the antiferromagnetic bulk materials. We point out that several explanations have been offered for these observations but no clear answer exist.

In chapter 2, we introduce the experimental tools used for the growth and study of the thin films. These include the growth of the films by pulsed laser deposition, high resolution x-ray diffraction from laboratory and synchrotron sources, x-ray photoelectron spectroscopy, atomic force microscopy and magnetic and dielectric characterization. Other techniques employed in this thesis but used by our collaborators, such as transmission electron microscopy (TEM) and embedded cluster calculations, are not included.

In chapter 3, we discuss the growth and the structure of the $TbMnO_3$ thin films under compressive strain on single crystals of atomically flat $SrTiO_3$ substrates. We show that the initial stage of the growth is 2D in the case of low oxygen pressures of 0.25mbar and 3D in the case of the films grown at 0.9mbar. However, in both cases, the structure of the films has been revealed to show the same evolution: A tetragonal unit cell is observed only for films as thin as 2nm ($\approx$ 3 unit cells). Above that thickness, the orthorhombic distortion starts appearing, increasing with increasing thickness but keeping the out-of-plane spacing constant. Above a critical thickness of about 60-80nm (depending on the oxygen pressure during growth), the films suddenly relax to

their bulk lattice parameters, showing a coexistence of a strained and a relaxed part. Moreover, we found that the four-fold symmetry of the cubic $SrTiO_3$ substrate leads to the formation of four equivalent orthorhombic domains, as confirmed by TEM experiments. The TEM images reveal a large density of domain walls and small domains, whose sizes increase with increasing thickness. The density of domain walls has been estimated from the images and it is found to scale with the inverse of the thickness for the fully-strained films, and to deviate from that behavior for the partially relaxed films. The main results in this chapter are: The successful stabilization, for the first time, of $TbMnO_3$ films under compressive strain on $SrTiO_3$ substrates; the tunability of the orthorhombicity with thickness; and the control of the size of the domains (or the density of domain walls) with thickness.

In chapter 4, we present the magnetic measurements performed on the films described in chapter 3, together with x-ray photoelectron spectroscopy (XPS) measurements and embedded cluster calculations. The XPS measurements showed an increase of the Mn_{3s} exchange splitting compared to the expected splitting for Mn^{3+}. The origin of the increase of the splitting has been investigated by means of embedded cluster calculations and it was attributed to an increase of ionicity in the thin film with respect to the bulk material. We show that the dominant magnetic interactions in the thin films are antiferromagnetic, similar to the bulk material, but that ferromagnetic interactions are present in the films below the Nèel temperature, evidenced by a splitting between the field-cooled (FC) and zero-field-cooled (ZFC) magnetization curves. The induced magnetization, or the magnitude of the FC-ZFC splitting, , has been investigated as a function of thickness (d) and it has been found to follow the same dependence than both the density of domain walls and the orthorhombic distortion (pseudo-cubic angle): $\propto d^{-1}$. In principle, both are good candidates to explain the origin of the induced ferromagnetism in the films. However, the out-of-plane magnetization also shows a splitting between the field-cooled and zero-field-cooled conditions, at around 40K, which is different from the expectation of an antiferromagnetic

coupling along this direction, strongly suggesting that it is not the structural distortion but, instead, the presence of domain walls, that causes the ferromagnetism.

In chapter 5, we present the dielectric characterization of the films. The anomaly in the dielectric constant that is observed in the bulk material at about 27 K, related to the onset of the electrical polarization and linked to the transition from a sinusoidal to an spiral spin state, was not observed in the fully-strained thin films. However, the anomaly was recovered for films showing coexistence of a strained and a relaxed part. We postulate that the small size of the domains and the large number of domain walls prevent the long-range spin order and, therefore, also the associated ferroelectric order. Impedance analysis allowed us to separate the different contributions to the dielectric response and revealed two Debye-like relaxation mechanisms. One of them is related to polaron hopping, while the other is attributed to relaxation of domain walls. Magnetocapacitance measurements showed that the films are magnetoelectric due to the large magnetoresistance of the domain walls. The domain wall relaxation times show a change of slope at the bulk ferroelectric transition temperature ($T_C \simeq 27$K), suggesting that there is local ferroelectric order, modifying the relaxation of the domain walls. The results in this chapter show the wealth of information extracted from the dielectric measurements in the films, which reveal that the functional properties of the films are determined by their domain walls. This opens the interesting possibility to utilize domain walls for applications (specially for applications requiring miniaturization).

In chapter 6, we present preliminary results on the growth and characterization of $TbMnO_3$ films grown on $SrRuO_3$-buffered (001)-$DyScO_3$ in an attempt to have a finer control of the structure of $TbMnO_3$. (001)-$DyScO_3$ has the same space group as $TbMnO_3$ and should impose tensile strain on $TbMnO_3$. The films are epitaxial, single-phase and have an orthorhombic structure. However, due to the relaxed $SrRuO_3$ layer, needed for the electrical characterization of the films, the strain state of the films is

not imposed by the substrate, but by the electrode. The dielectric behavior of the films show little influence of the domain walls, as expected, since the isomorphism of the substrate, electrodes and film should prevent the formation of domains.

In conclusion, we show that epitaxial growth on high-symmetry substrates offers a way to control the structure and properties of $TbMnO_3$ and other orthorhombic perovskites, allowing tuning the orthorhombic distortion with increasing thickness. We have shown that the films consist of fine domains and a large density of domain walls, which can be asymptotically increased with decreasing thickness, allowing domain engineering. Due to this microstructure, the properties of the films are very different from those of the bulk material. The magnitude of induced ZFC-FC hysteresis, or induced magnetic moment, absent in bulk, is found to have the same thickness dependence as the domain wall density and the orthorhombic distortion (these two being naturally linked). Although a direct effect of the epitaxial strain (decrease of the orthorhombic distortion) cannot be totally ruled out, this cannot explain the observed out-of-plane magnetization. Our results suggest that the observed ferromagnetism, below the spin ordering temperature, is due to the domain walls. The relaxation of the crystallographic domain walls could be evidenced in the dielectric investigation of the films. Magnetocapacitance and magnetoresistance effects were observed and also linked to the domain walls that are believed to pin the antiferromagnetic domain walls when the system orders magnetically.

This work shows the importance of domain walls in multiferroic and magnetoelectric materials and their potential for device implementation when the miniaturization becomes limited by materials' size effects. This idea of using domain walls as functional objects, is creating a new field of research associated with the study and manipulation of the properties of designed domain wall structures in multiferroics and other functional materials (see very recent works in references [141, 149, 161]). The present work represents significant advance in this direction.

Samenvatting

Dit proefschrift beschrijft het experimenteel onderzoek naar de fysische- en structuureigenschappen van dunne lagen multiferroisch $TbMnO_3$ onder epitaxiale spanning. Multiferroische verbindingen maken deel uit van een materiaalklasse waarin spontane elektrische polarisatie en magnetisatie binnen eenzelfde fase naast elkaar bestaan. Dergelijke multiferroische materialen komen slechts in beperkte mate voor in de natuur. Daarom richten onderzoeksinspanningen zich voornamelijk op het in synthetiseren en in kaart brengen van nieuwe multiferroische materialen. Met name binnen de groep multiferroica verwacht men materialen te vinden die beschikken over zeer goede magnetoelektrische respons. Het feit dat de magnetische ordening en elektrische ordening in een dergelijke materiaalklasse gekoppeld zijn, maakt ze interessant voor toepassing in zowel spintronica als in geheugen elementen met vier schakelbare toestanden. De tot dusver gevonden koppelingen zijn echter nog te zwak om van direct nut te zijn in alledaagse toepassingen. De mogelijkheden om de materiaalrespons te optimaliseren, omvatten het aanbrengen van een geschikte dotering, het toepassen van extern aangelegde druk of het teweeg brengen van epitaxiale spanning. De laatste jaren is het begrip van de mechanismen die ten grondslag liggen aan multiferroisch gedrag in een aantal materialen sterk gegroeid. Tegelijkertijd worden op experimenteel en theoretisch vlak de krachten gebundeld, niet alleen om nieuwe systemen te vinden met verbeterde magneto(di)elektrische respons, of om bestaande materialen aan te passen, waarbij beoogd wordt een verbeterde magnetoelektrische koppeling te bereiken , maar ook om totaal nieuwe multiferroica te ontwikkelen.

Dit proefschrift richt zich in het bijzonder op de invloed van epitaxiale spanning op een multiferroisch materiaal. Hierbij besteden we met name aandacht aan een van

de meest bestudeerde multiferroische materialen, $TbMnO_3$. In dit materiaal wordt de spontane elektrische polarisatie veroorzaakt door spin spiraal ordening waarmee tevens een sterke magnetoelektrische koppeling wordt gegenereerd. Bovendien kan in een dergelijk systeem een grote invloed worden verwacht van epitaxiale spanning die het resultaat is van een subtiel evenwicht van magnetische interacties en de daaraan inherente sterke magnetische frustratie. Er waren bij aanvang van dit onderzoek geen gerapporteerde resulaten beschikbaar die het gedrag van $TbMnO_3$ onder epitaxiale spanning beschrijven, ondanks hun onschatbare waarde. We hebben de structuur en eigenschappen van dunne lagen van $TbMnO_3$ onder drukspanning, met een laagdikte van minder dan 100nm, bestudeerd.

In hoofdstuk 1, maken we allereerst kennis met multiferroische- en magnetoelektrische materialen en het belang van deze materialen in een brede context. Dit zal worden belicht vanuit zowel een fundamenteel wetenschappelijk perspectief als ook vanuit de invalshoek van het toepassingsveld. We zullen in het bijzonder aandacht besteden aan $TbMnO_3$, het materiaal dat centraal staat in dit proefschrift. We beschrijven de kristalstructuur en de magnetische ordening van dit bulk materiaal. We brengen de algemene redenen naar voren om een dunne lagen van deze materialen te groeien en motiveren waarom wij in het bijzonder hebben gekozen voor de groei van dunne lagen $TbMnO_3$. Tot slot behandelen we recente experimentele resultaten van enkele epitaxiaal gegroeide zeldzame-aard manganaten, in het bijzonder van manganaten die een verschil vertonen tussen nul-veld gekoelde en veldgekoelde magnetisatie curves. Deze opsplitsing van magnetisatiecurves wordt doorgaans niet waargenomen in de antiferromagnetische bulk materialen. Verschillende verklaringen zijn hiervoor geopperd, maar een duidelijke verklaring is thans nog niet gevonden.

In hoofdstuk 2, behandelen we het instrumentarium om dunne lagen te groeien en ze vervolgens te bestuderen. Dit omvat het groeien van dunne lagen met behulp van gepulsde laser depositie, hoge resolutie R*ö*ntgen diffractie met zowel laboratorium als synchrotron stralingsbronnen , R*ö*ntgen fotoelektron spectroscopie (XPS), atoomkrachtmicroscopie (AFM) en magnetische en di*ë*lektrische karakterisatie. We

zullen niet dieper ingaan op de overige technieken die wel in dit proefschrift aan bod komen, maar door collega's werden toegepast zoals Transmissie Elektronen Microscopie (TEM) of embedded cluster berekeningen.

Hoofdstuk 3 start met een discussie over het groeien en de kristalstructuur van $TbMnO_3$ onder drukspanning op monokristallijne en atomair vlakke $SrTiO_3$ substraten. We tonen aan dat de groei twee dimensionaal aanvangt als lage zuurstofdrukken van 0.25mbar worden toegepast en dat het beginstadium van de kristalgroei driedimensionaal verloopt indien de films bij 0.9mbar gegroeid worden. In beide gevallen vertoont de structuur van de dunne lagen echter dezelfde ontwikkeling: Voor dunne lagen die slechts 2nm (ongeveer 3 eenheidcellen) dik zijn, wordt een tetragonale eenheidscel gevonden. Boven deze laagdikte verschijnt een orthorhombische vervorming die met laagdikte in omvang toeneeemt, maar de uit-het-vlak vlakafstand constant houdt. Boven een kritieke dikte van ongeveer 60-80nm (dit hangt af van de zuurstofdruk tijdens het groeien), relaxeren de films plotseling naar de bulk roosterparameters, waarbij gespannen en ontspannen gedeelten naast elkaar bestaan. Bovendien hebben we gevonden dat de viervoudige symmetrie van kubisch $SrTiO_3$ leidt tot de vorming van vier equivalente orthorhombische domeinen, zoals bevestigd met TEM experimenten. De TEM afbeeldingen onthullen een hoge domeinwanddichtheid en kleine domeinen waarvan de grootte toeneemt met toenemende laagdikte. Aan de hand van de afbeeldingen hebben we de de domeinwanddichtheid afgeschat, die geschaald kan worden aan de reciproke dikte van de dunne lagen onder volledige spanning, maar van dit gedrag wordt afgeweken in gedeeltelijk ontspannen films. De belangrijkste resultaten van dit hoofdstuk omvatten: Het -voor het eerst- succesvol stabiliseren van dunne lagen $TbMnO_3$ onder drukspanning op $SrTiO_3$ substraten; Het gecontroleerd beinvloeden van orthorhombiciteit met behulp van laagdikte; en beinvloeding van domeingrootte (of de domeinwanddichtheid) met behulp van dikte.

In hoofstuk 4 wordt de magnetische karakterisatie van de dunne lagen die in hoofdstuk 3 aan de orde zijn geweest, tesamen met de Röntgen fotoelektron spectroscopie (XPS) metingen en de embedded cluster berekeningen besproken. In de XPS metingen

komt een grotere toename van Mn_{3s} exchange opsplitsing naar voren dan op grond van de berekingen op voorhand voor Mn^{3+} verwacht mag worden. De oorzaak van de toegenomen exchange opsplitsing hebben we nader onderzocht aan de hand van embedded cluster berekeningen en kan worden toegeschreven aan de ioniciteit van de dunne laag ten opzichte van het substraat materiaal. We tonen aan dat de antiferromagnetische interacties het sterkst zijn, net zoals in het bulk materiaal. Daarentegen zijn beneden de N$\acute{e}$el temperatuur in dunne lagen ferromagnetische interacties actief die tot uitdrukking komen in een opsplitsing tussen veld gekoelde en nulveld gekoelde magnetisatie karakteristieken. De ge$\ddot{i}$nduceerde magnetisatie, ofwel de omvang van de veld gekoelde tegen nulveld opsplitsing, is bestudeerd voor vari$\ddot{e}$rende laagdikte en volgt dezelfde tendens die eerder naar voren kwam voor de domeinwanddichtheden en orthorhombische roostervervorming (pseudo kubische hoek) die aanwezig zijn in de dunne lagen: $\propto d^{-1}$. Beiden kunnen het geobserveerde ferromagnetisme dat optreedt in de dunne lagen in principe goed verklaren. Echter, de magnetisatie die loodrecht op het vlak staat, vertoont eveneens een opsplitsing tussen veldkoeling en nulveldkoeling bij ongeveer 40K. Dit verschilt wezenlijk van de verwachte antiferromagnetische koppeling langs deze richting en doet vermoeden dat niet de kristalroostervervorming, maar de aanwezigheid van domeinwanden het geobserveerde ferromagnetisme veroorzaakt.

In hoofdstuk 5 bespreken we de dielektrische karakterisatie van dunne lagen. De intrede van elektrische polarisatie in het bulk materiaal bij 27K wordt waargenomen als een dielektrische anomalie, die niet tot uitdrukking komt in dunne lagen onder volledige spanning en ontstaat ten gevolge van een overgang van een sinusoidale naar spiraal magnetische ordeningstoestand. De anomalie verschijnt echter wel weer in dunne lagen waarin een gespannen deel en een gerelaxeerd deel naast elkaar bestaan. We voeren aan dat de beperkte domeingrootte en het grote aantal domeinwanden, de magnetische ordening op uitgebreide lengteschalen en daarmee ook de daaraan inherente elektrische ordening verhindert. Impedantie analyse maakt het mogelijk om de verschillende bijdragen aan de dielektrische respons van elkaar te onderscheiden

en onthult twee Debye relaxatie mechanismen. Het ene mechanisme is gebaseerd op polaron hopping terwijl het andere mechanisme toegeschreven kan worden aan het relaxeren van domeinwanden. Magnetocapaciteitsmetingen tonen aan dat de dunne lagen magnetoelektrisch zijn door de grote magnetoweerstand van de domeinwanden. De relaxatie tijd van de domeinwanden vertoont een verandering van helling ter hoogte van de ferroelektrische faseovergang (T_c=27K) in het bulk materiaal. Dit doet vermoeden dat de lokale ferroelektrische ordening de relaxatie van domeinwanden verstoort. De resultaten die in dit hoofdstuk naar voren worden gebracht, tonen een schat aan informatie die gewonnen kan worden uit dielektrische metingen aan de dunne lagen. Deze informatie verschaft ons het inzicht dat de functionele eigenschappen van de dunne lagen worden bepaald door de domeinwanden. Dit biedt perspectieven voor vervolgonderzoek naar het gerichte gebruik van domeinwanden voor toepassingen (in het bijzonder in situaties waar schaalverkleinig vereist is).

In hoofdstuk 6, bespreken we de voorlopige resultaten van de groei en karakterisatie van dunne lagen $TbMnO_3$ op een $SrRuO_3$ gebufferd (001)-$DyScO_3$ substraat. Dit is een poging om een nog geraffineerdere controle te hebben op de $TbMnO_3$ structuur. (001)-$DyScO_3$ heeft dezelfde ruimtegroep als $TbMnO_3$ en zou een trekspanning moeten uitoefenen op $TbMnO_3$. De films zijn epitaxiaal gegroeid en bestaan uit een enkele kristalfase en hebben een orthorhombische structuur. Helaas wordt de opspanning van de dunne lagen in dit geval niet bepaald door het substraat, maar door de gerelaxeerde $SrRuO_3$ laag die van belang is voor de elektrische karakterisatie van de dunne lagen. Uit de karakterisatie van de dunne lagen blijkt dat de domeinwanden weinig invloed hebben op het dielektrisch gedrag. Dit sluit aan bij ons verwachtingspatroon, dat de gelijkvormigheid van het substraat, de elektrodes en dunne laag domeinvorming zouden moeten tegengaan.

We concluderen dat epitaxiale groei op hoog symmetrische substraten de mogelijkheid biedt om de structuur en eigenschappen van $TbMnO_3$ en andere orthorhombische perovskieten te beinvloeden. We hebben aangetoond dat de dunne lagen bestaan uit fijne domeinen met een hoge domeinwanddichtheid , die asymptotisch kan wor-

den verhoogd naarmate de laagdikte afneemt, waardoor domein ”engineering” mogelijk wordt. Door deze microstructuur verschillen de eigenschappen van de dunne lagen sterk van die van het bulk materiaal. De omvang van de geinduceerde nul veld gekoelde -veld gekoelde hysterese, ofwel het geinduceerd magnetisch moment, dat afwezig is in het bulk materiaal, vertoont de zelfde tendens met laagdikte als de domeinwanddichtheid en de orthorhombische roostervervorming (deze grootheden zijn staan gedeeltelijk met elkaar in verband). Dit doet vermoeden dat het waargenomen ferromagnetisme door de domeinwanden wordt veroorzaakt onder de cycloidale spin ordening, alhoewel een direct epitaxiaal spanningseffect (afname in orthorhombische roostervervorming) niet geheel veronachtzaamd kan worden. De relaxatie van kristallografische domeinwanden komt aan het licht in the dielektrische karakterisatie van de dunne lagen. De waargenomen magnetocapaciteit en magnetoweerstand effecten worden in verband gebracht met kristallografische domeinwanden die antiferromagnetische domeinwanden immobiliseren zodra het systeem zich magnetisch ordent.

Dit onderzoek onderstreept het belang van domeinwanden in multiferroische en magnetoelektrische materialen, maar schetst ook de mogelijkheden die domeinwanden bieden voor gebruik in devices. zodra mintiaturisering van belang is. Het concept om domeinwanden als functionele objecten te beschouwen kan een nieuw onderzoeksveld creeren dat zich bezighoudt met de manipulatie en de eigenschappen van ontworpen domeinwandstructuren in multiferroica en andere functionele materialen (zeer recent werk is te vinden in referenties [141, 149, 161])

Bibliography

[1] H. Schmid, Ferroelectrics **162**, 317 (1994).

[2] N. A. Hill, Journal of Physical Chemistry B **104**, 6694 (2000).

[3] S.-W. Cheong and M. Mostovoy, Nature Materials **6**, 23 (2007).

[4] D. I. Khomskii, J. of Magn. and Magn. Mat. **306**, 1 (2006).

[5] D. Khomskii, Physics **2**, 20 (2009).

[6] N. A. Spaldin and M. Fiebig, Science **309**, 391 (2005).

[7] W. Eerenstein, N. Mathur, and J. F. Scott, Nature **442**, 759 (2006).

[8] Y. Tokura, Science **312**, 1481 (2006).

[9] G. A. Smolenskii, A. I. Agranovskaia, S. N. Popov, and V. A. Isopov, Sov. Phys. Tech. **3**, (1981-1982).

[10] Y. Yang, J. Liu, H. Huang, W. Q. Zou, P. Bao, and Z. G. Liu, Phys. Rev. B **70**, 132101 (2004).

[11] V. R. Palkar and S. M. Malik, Solid State Communications **134**, 783 (2005).

[12] A. A. Belik, S. Likudo, K. Komada, N. Igawa, S.-I. Shamoto, M. Maie, T. Nagai, Y. Matsui, S. Stefanovich, I.-B. Lazoryak, and E. Takayama-Muromachi, J. American Chem. Soc. **128**, 3 (2006).

[13] R. Seshadri and N. A. Hill, Chem. Mater. **13**, 2892 (2001).

[14] T. Atou, H. Chiba, K. Ohoyama, Y. Yamaguchi, and Y. Syono, J. Solid State Chem. **145**, 639 (1999).

[15] A. M. dos Santos, A. K. Cheetham, T. Atou, Y. Syono, Y. Yamaguchi, K. Ohoyama, H. Chiba, and C. Rao, Phys. Rev. B **66**, 064425 (2002).

[16] A. M. dos Santos, S. Parashar, A. R. Raju, Y. S. Znao, A. K. Cheetman, and C. Rao, Solid State Communications **122**, 49 (2002).

[17] E. Montanari, G. Calestani, A. Migliori, M. Diapiaggi, F. Bolzoni, R. Cabassi, and Gilioli, Chem. Mater. **17**, 6457 (2005).

[18] E. Montanari, G. Calestani, L. Righi, E. Gilioli, F. Bolzoni, K. Knight, and P. Radaelli, Phys. Rev. B **75**, 220101 (2007).

[19] T. Kimura, S. Kawamoto, I. Yamada, M. .Azuma, M. Takano, and Y. Tokura, Phys. Rev. B **67**, 180041 (2003).

[20] T. Shishidou, N. Mikamo, Y. Uratani, F. Ishii, and T. Oguchi, J. Phys.: Condens. Mat. **16**, S5677 (2003).

[21] A. Sharan, J. Lettieri, Y. Jia, W. Tian, X. Pan, D. Schlom, and V. Gopalan, Phys. Rev. B **69**, 214109 (2004).

[22] T. Yokasawa, A. Belik, T. Asaka, K. Kimoto, E. Takayama-Muromachi, and Y. Matsui, Phys. Rev. B **77**, 024111 (2008).

[23] P. Baettig, R. Seshadri, and N. Spaldin, J. American Chem. Soc. **129**, 9854 (2007).

[24] J. B. Neaton, C. Ederer, U. V. Waghmare, N. A. Spaldin, and K. M. Rabe, Phys. Rev. B **71**, 014113 (2005).

[25] B. V. Aken, T. Palstra, A. Filippetti, and N. Spaldin, Nature Materials **3**, 164 (2004).

[26] G. Nénert, M. Pollet, S. Marinel, G. R. Blake, A. Meetsma, and T. Palstra, J. Phys.: Condens. Mat. **19**, 466212 (2007).

[27] C. Fennie and K. M. Rabe, Phys. Rev. B **72**, 100103(R) (2005).

[28] U. Adem, Ph.D. thesis, PhD Thesis, Rijskuniversiteit Groningen, http://irs.ub.rug.nl/ppn/314853448, 2008.

[29] D. A. Efremov, J. V. den Brink, and D. I. Khomskii, Nature Materials **3**, 853 (2004).

[30] M. Mostovoy, Phys. Rev. Lett. **96**, 067601 (2006).

[31] L. Landau and E. Lifshitz, in *Electrodynamics of continuous media*, edited by E. Butterworth-Heineman (Addison-Wesley Publishing Compagny, Inc., Massachusetts, USA, 1960).

[32] I. Dzyaloshinskii and L. Pitaevskii, Soviet Phys.- JETP **9**, 1281 (1959).

[33] D. N. Astrov, Soviet Phys.- JETP **11**, 708 (1960).

[34] D. N. Astrov, Soviet Phys.- JETP **13**, 729 (1961).

[35] L. W. Martin, S. P. Crane, Y.-H. Chu, M. B. Holcomb, M. Gajek, M. Huijben, C.-H. Yang, N. Balke, and R. Ramesh, J. Phys.: Condens. Mat. **20**, 434220 (2008).

[36] R. Ramesh and N. Spaldin, Nature Materials **6**, 21 (2007).

[37] W. Prellier, M. Singh, and P. Murugavel, J. Phys.: Condens. Mat. **17**, R803 (205).

[38] V. Goldsmidt, I. Mat.-Nat. Kl. (1926).

[39] J. A. Alonso, M. Martinez-Lope, M. Casais, and M. Fernandez-Diaz, Inorganic Chemistry **39**, 917 (2000).

[40] M. Kenzelmann, A. B. Harris, S. Jonas, C. Broholm, J. Schefer, S. B. Kim, C. L. Zhang, S.-W. Cheong, O. P. Vajk, and J. W. Lynn, Phys. Rev. Lett. **95**, 087206 (2005).

[41] J. Blasco, C. Ritter, J. García, J. de Teresa, J. Pérez-Cacho, and M. Ibarra, Phys. Rev. B **62**, 5609 (2000).

[42] N. Aliouane, D. N. Argyriou, J. Strempfer, I. Zegkinoglou, S. Landsgesell, and M. v. Zimmermann, Phys. Rev. B **73**, 020102 (2006).

[43] M. Hervieu, C. Martin, A. Maignan, G. Van-Tendeloo, and B. Raveau, Eur. Phys. J. B **10**, 397 (1999).

[44] A. Maignan, C. Martin, G. Van-Tendeloo, M. Hervieu, and B. Raveau, Phys. Rev. B **60**, 15214 (1999).

[45] A. Glazer, Acta Cryst. **B28**, 3384 (1972).

[46] H. Jahn and E. Teller, Proceedings of the Royal Society of London. Series A, Mathematical and Physical Sciences **161**, 220 (1934-1990).

[47] H. A. Kramers, Physica 1 182 (1934).

[48] P. W. Anderson, Phys. Rev. 350 (1950).

[49] J. Goodenough, in *Magnetism and chemical bonds*, edited by J. Wiley and Sons (Interscience publishers, New York, 1963).

[50] T. Goto, T. Kimura, G. Lawes, A. P. Ramirez, and Y. Tokura, Phys. Rev. Lett. **92**, 257201 (2004).

[51] G. Matsumoto, Journal of the Physical Society of Japan **29**, 606 (1970).

[52] A. Muñoz, M. Casáis, J. A. Alonso, M. J. Martínez-Lope, J. Martínez, and M. Fernández-Díaz, Inorganic Chemistry **40**, 1020 (2001).

[53] G. Maris, Ph.D. thesis, PhD Thesis, Rijskuniversiteit Groningen, http://irs.ub.rug.nl/ppn/261677454, 2004.

[54] T. Kimura, T. Goto, H. Shintani, K. Ishizaka, T. Arima, and Y. Tokura, Nature **426**, 55 (2003).

[55] T. Kimura, S. Ishihara, H. Shintani, T. Arima, K. Takahashi, K. Ishizaka, and Y. Tokura, Phys. Rev. B **68**, 060403 (2003).

[56] E. Lifshitz, JETP **11**, 253 (1941).

[57] J. L. Ribeiro, Phys. Rev. B **76**, 144417 (2007).

[58] N. Kida, Y. Yamasak, R. Shimano, T.-H. Arima, and Y. Tokura, Jour. Phys. Soc. Japan **77**, 12 (2008).

[59] Y. Yamasaki, H. Sagayama, N. Abe, T. Arima, K. Sasai, M. Matsuura, K. Hirota, D. Okuyama, Y. Noda, and Y. Tokura, Phys. Rev. Lett. **101**, 097204 (2008).

[60] H. Katsura, N. Nagaosa, and A. Balatsky, Phys. Rev. Lett. **95**, 057205 (2005).

[61] C. Jia, S. Omoda, N. Nagaosa, and J. Han, Phys. Rev. B **74**, 224444 (2006).

[62] I. A. Sergienko and E. Dagotto, Phys. Rev. B **73**, 094434 (2006).

[63] Q. C. Li, S. Dong, and J.-M. Liu, Phys. Rev. B **77**, 054442 (2008).

[64] I. E. Dzyaloshinskii, Soviet Phys.- JETP **19**, 960 (1964).

[65] T. Moriya, Phys. Rev. **120**, 91 (1960).

[66] C. Jia, S. Onoda, N. Nagaosa, and J. H. Han, Phys. Rev. B **76**, 144424 (2007).

[67] H. J. Xiang, S.-H. Wei, M.-H. Whangbo, and J. L. F. D. Silva, Phys. Rev. Lett. **101**, 037209 (2008).

[68] A. Malashevich and D. Vanderbilt, Phys. Rev. Lett. **101**, 037210 (2008).

[69] T. Kimura, Annu. Rev. Matter. Res. **37**, 387 (2007).

[70] N. Abe, K. Taniguchi, S. Ohtani, T. Takenobu, Y. Iwasa, and T. Arima, Phys. Rev. Lett. **99**, 227206 (2007).

[71] T. H. Lin, H. C. Shih, C. C. Hsieh, C. W. Luo, J.-Y. Lin, J. L. Her, H. D. Yang, C.-H. Hsu, T. M. Uen, and J. Y. Juang, J. Phys.: Condens. Mat. **21**, 026013 (2009).

[72] J. Lin, T. Han, C. Wu, M.-W. Chu, and C. Chen, Journal of Crystal Growth **310**, 3878 (2008).

[73] X. Martí, V. Skumryev, A. Cattoni, A. Bertaco, V. Laukhin, C. Ferrater, M. García-Cuenca, M. Varela, F. Sánchez, and J. Fontcuberta, J. of Magn. and Magn. Mat. **321**, 1719 (2009).

[74] C. C. Hsieh, T. H. Lin, H. C. Shih, C.-H. Hsu, C. W. Luo, J.-Y. Lin, K. H. Wu, T. M. Uen, and J. Y. Juang, Journal of Applied Physics 103912 (2008).

[75] D. Rubi, S. Venkatesan, B. J. Kooi, J. T. M. D. Hosson, T. T. M. Palstra, and B. Noheda, Phys. Rev. B **78**, 020408 (2008).

[76] M. Fujimura, N. Shigemitsu, T. Takahashi, A. Ashida, T. Yoshimura, H. Fukumura, and D. Harima, Philosophical Magazine Letters **87**, 193 (2007).

[77] P. Murugavel, J.-H. Lee, D. Lee, T. W. Noh, Y. Jo, M.-H. Jung, Y. S. Oh, and K. H. Kim, Appl. Phys. Lett. **90**, 142902 (2007).

[78] J.-H. Lee, P. Murugavel, H. Ryu, D. Lee, J. Y. Jo, W.Kim, H. J. Kim, K. H. Kim, Y. Jo, M.-H. Jung, Y. H. Oh, Y.-W. Kim, J.-G. Y. J.-S. Chung, and T. Noh, Advanced Materials **18**, 3125 (2006).

[79] D. Lee, J.-H. Lee, P. Murugavel, S. Y. Jang, T. W. Noh, Y. Jo, M.-H. Jung, Y.-D. Ko, and J.-S. Chung, Appl. Phys. Lett. **90**, 182504 (2007).

[80] A. Bosak, A. A. Kamenev, I. Graboy, S. Antonov, O. Y. Gorbenko, A. Kaul, C. Dubourdieu, J. Senateur, V. L. Svechnikov, and H. Zandbergen, Thin Solid Films **400**, 149 (2001).

[81] S. Morup, D. E. Madsen, C. Frandsen, C. R. H. Bahl, and M. F. Hansen, J. Phys.: Condens. Mat. 213202 (2007).

[82] C. Dubourdieu, G. Huot, I. Gelard, H. Roussel, O. I. Lebedev, and G. V. Tendeloo, Philosophical Magazine Letters **87**, 203 (2007).

[83] C. W. Y. cui and B. Cao, Solid State Communications **133**, 641 (2005).

[84] Y. Cui, W. Cai, Y. Li, J. Qian, P. Xu, R. Wang, J. Yao, and L. Zhang, Journal of Applied Physics **100**, 034101 (2006).

[85] Y. M. Cui, L. W. Zhang, C. C. Wang, G. L. Xie, C. P. Chen, and B. S. Cao, Appl. Phys. Lett. **86**, 203501 (2005).

[86] B. J. Kirby, D. Kan, A. Luykx, M. Murakami, D. Kundaliya, and I. Takeuchi, Journal of Applied Physics **105**, 07D917 (2009).

[87] D. Chrisey and G. Hubler, in *Pulsed laser deposition of thin films*, edited by D. Chrisey and G. Hubler (John Wiley and Sons, New York, 1994).

[88] B.Dam, J. Rector, J. Johansson, J. Huijbregtse, and D. D. Groot, Journal of Applied Physics 3386 (1998).

[89] A. Namiki, T. Kawai, and K. Ichige, Surf. Sci. **166**, 129 (1986).

[90] I. Markov, in *Crystal growth for beginners*, edited by London (World Scientific, Singapore, 1995).

[91] G. Rijnders, G. Koster, D. Blank, and H. Rogalla, Appl. Phys. Lett. 1888 (1997).

[92] G. Rijnders and D. H. Blank, in *Thin films and heterostructures for oxides electronics*, edited by S. B. Ogale (Springer US, New York, 2005).

[93] H. A. Atwater, C. C. Ahn, S. S. Wong, G. He, H. Yoshino, and S. Nikzad, Surf. Rev. and Lett. 525 (1997).

[94] S. Kikuchi, Japan. Journ. of Phys. **5**, 83 (1928).

[95] J. Als-Nielsen and D. M. Morrow, in *Element of modern x-ray*, edited by J. Wiley and Sons (John Wiley and Sons, New York, 2001).

[96] A. K. Jonscher, Chelsea Dielectrics Press (1983).

[97] P. Debye, Dover Publications, New York. 84 (1929).

[98] G. Koster, B. L. Kropman, G. J. H. M. Rijnders, D. H. A. Blank, and H. Rogalla, Appl. Phys. Lett. **73**, 2920 (1998).

[99] T. Hibma, XRD data simulation programm written in IDL6.0 .

[100] M. Babei and D. K. Ross, Physica C: Superconductivity **425**, 130 (2005).

[101] D. A. Rudman, F. Stork, J. Booth, J. Juang, L. Vale, G. Beatty, C. I. Williams, J. Beall, R. Ono, S. Qadri, M. Osofsky, E. Skelton, J. Claassen, G. Gibson, J. MacManus-Driscoll, N. Maide, and L. Cohen, Applied Superconductivity (1999).

[102] K. Wang and J.-F. Li, Appl. Phys. Lett. **91**, 262902 (2007).

[103] L. Ranno, A. Llobet, R. Tiron, and E. Favre-Nicolin, Applied Surface Science **188**, 170 (2002).

[104] A. Llobet, L. Ranno, and J. Pierre, Mat. Sc. Forum **373-376**, 517 (2001).

[105] R. Tackett, G. Lawes, B. C. Melot, M. Grossman, E. S. Toberer, and R. Seshadri, Phys. Rev. B **76**, 024409 (2007).

[106] E. Beyreuther, S. Grafstrom, L. M. Eng, C. Thiele, and K. Dorr, Phys. Rev. B **73**, 155425 (2006).

[107] M. P. de Jong, I. Bergenti, W. Osikowicz, R. Friedlein, V. Dediu, C. Taliani, and W. R. Salaneck, Phys. Rev. B **73**, 052403 (2006).

[108] D. Wang, C. Xiong, G. Liu, Y. Xie, B. Shen, and J. Sun, Physica B: Condensed Matter **371**, 187 (2006).

[109] C. Fadley, Electron Spectroscopy 781 (1972).

[110] L. Fiermans, R. Hoogewijs, and J. Vennik, Surface Science **47**, 1 (1975).

[111] R. P. Gupta and S. K. Sen, Phys. Rev. B 1071 (1974).

[112] R. P. Gupta and S. K. Sen, Phys. Rev. B **12**, 1215 (1975).

[113] H. W. Nesbitt and D. Banerjee, American Mineralogis **83**, 305 (1998).

[114] A. Chaika, A. Ionov, N. Tulina, D. Shulyatev, and Y. Mukovskii, Journal of Electron Spectroscopy and Related Phenomena **148**, 101 (2005).

[115] Q. H. Wu, J.-M. Xu, Q.-C. Zhuang, and S.-G. Sun, Solid State Ionics **177**, 1483 (2006).

[116] B. Gillot, S. Buguet, E. Kester, C. Baubet, and P. Tailhades, Thin Solid Films **357**, 223 (1999).

[117] T. Maitra and A. Taraphder, Europhysics Letters **59**, 896 (2002).

[118] A. Sadoc, C. de Graaf, and R. Broer, Phys. Rev. B **75**, 165116 (2007).

[119] Z. Barandiaran and L. Seijo, The Journal of Chemical Physics **89**, 5739 (1988).

[120] C. de Graaf, R. Broer, W. C. Nieuwpoort, and P. S. Bagus, Chemical Physics Letters **272**, 341 (1997).

[121] L. Hozoi, A.H., de Vries, and R. Broer., Phys. Rev. B **64**, 165104 (2001).

[122] P. S. Bagus, R. Broer, and E. S. Ilton, Chemical Physics Letters **394**, 150 (2004).

[123] V. Galakhov, M. Demeter, S. Bartkowski, M. Neumann, N. A. Ovechkina, E. Kurmaev, N. I. Lobachevskaya, Y. M. Mukovskii, J. Mitchell, and D. Ederer, Phys. Rev. B **65**, 113102 (2002).

[124] H. Raebiger, S. Lany, and A. Zunger, Nature **453**, 763 (2008).

[125] R. Resta, Nature **453**, 735 (2008).

[126] Y. Konishi, Z. Fang, M. Izumi, T. Manako, M. Kasai, H. Kuwahara, M. Kawasaki, K. Terakura, and Y. Tokura, Journal of the Physical Society of Japan **68**, 3790 (1999).

[127] N. Pertsev, A. Tagantsev, and N. Setter, Phys. Rev. B **61**, R825 (2000).

[128] A. R. Akbarzadeh, L. Bellaiche, J. Iniguez, and D. Vanderbilt, Appl. Phys. Lett. **90**, 242918 (2007).

[129] D. Meier, N. Allouane, D. N. Argyriou, J. A. Mydosh, and T. Lorenz, New J. Phys. **9**, 100 (2007).

[130] G. Lalitha and P. V. Reddy, J. of Magn. and Magn. Mat. **320**, 754 (2008).

[131] L. F. Bates, in *Modern Magnetism*, edited by Cambridge (Cambridge University Press, Cambridge, England, 1963).

[132] S. dong, R. Yu, S. Yunoki, J.-M. Liu, and E. Dagotto, Eur. Phys. J. B **69**, 00255 (2009).

[133] S. Venkatesan, C. Daumont, B. Kooi, B. Noheda, and J. D. Hosson, To be published .

[134] J. Privratska and V. Janovec, Ferroelectrics **204**, 321 (1997).

[135] J. Privratska and V. Janovec, Ferroelectrics **222**, 23 (1999).

[136] M. Daraktchiev, G. Catalan, and J. Scott, Ferroelectrics **375**, 122 (2008).

[137] A. V. Goltsev, R. V. Pisarev, T. Lottermoser, and M. Fiebig, Phys. Rev. Lett. **90**, 177204 (2003).

[138] T. Lottermoser and M. Fiebig, Phys. Rev. B **70**, 220407 (2004).

[139] M. Fiebig, T. Lottermoser, D. Frohlich, A. Goltsev, and R. Pisarev, Nature **419**, 818 (2002).

[140] H. Bea and P. Paruch, Nature Materials **8**, 168 (2009).

[141] J. Seidel, L. W. Martin, Q. He, Q. Zhan, Y.-H. Chu, A. Rother, M. E. Hawkridge, P. Maksymovych, P. Yu, M. Gajek, N. Balke, S. V. Kalinin, S.Gemming, F. Wang, G. Catalan, J. F. Scott, N. A. Spaldin, J. Orenstein, and R. Ramesh, Nature Materials **8**, 229 (2009).

[142] J. Scott, J. Mater. Res. **22**, 2053 (2007).

[143] J. Scott, J. Phys.: Condens. Mat. **20**, 021001 (2008).

[144] G. Catalan, Appl. Phys. Lett. **88**, 102902 (2006).

[145] Values between 17-45 have been measured.

[146] N. Mufti, Ph.D. thesis, PhD Thesis, Rijskuniversiteit Groningen, http://irs.ub.rug.nl/ppn/317182129, 2008.

[147] L. Martin−Carron, R. Ramirez, C.Prieto, A. de Andres, J. Sanchez−Benitez, M. Garcia−Hernandez, and J. Martinez, Journal of alloys and compounds **323**, 527 (2001).

[148] G. V. S. Rao, B. M. Wanklyn, and C. N. R. Rao, J. Phys. Chem. Solids **32**, 345 (1971).

[149] F. Kagawa, M. Mochizuki, Y. Onose, H. Murakawa, Y. Kaneko, N. Furukawa, and Y. Tokura, Phys. Rev. Lett. **102**, 057604 (2009).

[150] J. Scott, in *Ferroelectric memories*, edited by K. Itoh and T. Sakurai (Springer-Verlag, Germany Heidelberg, 2000).

[151] A. Seeger, P. Lunkenheimer, J. Hemberger, A. A. Mukhin, V. Y. Ivanov, A. M. Balnashov, and A. Loidl, J. Phys.: Condens. Mat. **11**, 3273 (1999).

[152] C. C. Wang and L. W. Zang, Appl. Phys. Lett. **90**, 142905 (2007).

[153] C. Wang, Y. Cui, and L. W. Zhang, Appl. Phys. Lett. **90**, 012904 (2007).

[154] S. M. Sze and K. N. Kwok, in *Physics of semiconductor devices*, 3rd ed. ed., edited by S. M. Sze (Wiley, Upper Saddle River, 2006).

[155] I. Horcas, R. Fernandez, J. Gomez-Rodriguez, J. Colchero, J. Gomez-Herrero, and A. M. Baro, Rev. Sci. Instrum. **78**, 013705 (2007).

[156] D. Toyota, I. Ohkubo, H. Kumigashira, M. Oshima, T. Ohnishi, M. Lippmaa, M. Kawasaki, and H. Koinuma, Journal of Applied physics **99**, 08N505 (2006).

[157] D. Rubi, A. Vlooswijk, and B. Noheda, Thin Solid Films **517**, 1904 (2009).

[158] J. Krug, Physica A **313**, 47 (2002).

[159] X. Ke, S. Rzchowski, L. J. Belenky, and C. B. Eom, Appl. Phys. Lett. **84**, 5458 (2004).

[160] D. J. Singh, The 40th annual conference on magnetism and magnetic materials **79**, 4818 (1996).

[161] Y. Tokunaga, N. Furukawa, H. Sakai, Y. Taguchi, T.-H. Arima, and Y. Tokura, Nature Materials **8**, 558 (2009).

List of publications

1. C.J.M. Daumont, D. Mannix, S. Venkatesan, D. Rubi, G. Catalan, B.J. Kooi, J.Th.M. De Hosson and B. Noheda, Epitaxial $TbMnO_3$ thin films on $SrTiO_3$ substrates: A structural study, J. Phys.: Condens. Matter **21** N^o 18 (2009) 182001.

2. D. Rubi, C. de Graaf, C.J.M. Daumont, D. Mannix, R. Broer and B. Noheda, Ferromagnetism and increased ionicity in epitaxially grown $TbMnO_3$ films, Phys. Rev. B **79**, 014416 (2009).

3. S. Venkatesan, C.J.M. Daumont, B.J. Kooi, B. Noheda and J.Th.M. De Hosson, Evolution of nanodomain structures and strain relaxation in thin films of the multiferroic $TbMnO_3$: A transmission electron microscopy study. Submitted.

4. C.J.M. Daumont, S. Venkatesan, B.J. Kooi, G. Catalan, J.Th.M. De Hosson, J.F. Scott and B. Noheda, Ferromagnetic domain walls in $TbMnO_3$ thin films. In preparation.

5. C.J.M. Daumont, A. Ferri, S. Faroshkipoor and B. Noheda, Characterizing ferroelectric rotation states in $BiFeO_3$. To be submitted.

Acknowledgments

First of all, I would like to thank my supervisors, Prof. dr. Beatriz Noheda and Prof. dr. Thom Palstra, for giving me the opportunity to enroll as a Ph.D. student, within the European project MaCoMuFi, at the University of Groningen, in the solid state chemistry department within the thin film part of the group. Beatriz, I could not thank you enough for all the advice and great guidance through all these four years, not only for the thesis in itself but also to build an international prospective for my future carrier. You were also here to discuss about personal matters, which forged even more respect. I am really proud of having been under your supervision during these four years. I would also like to address my gratitude to you, Thom. Your skills, scientific criticisms and experience have been really useful to go further in this work. Even though your time went more and more limited through the years, you always had constructive criticisms. I would also like to address many thanks to Dr. Gustau Catalan. He made the $TbMnO_3$ target and grew the first $TbMnO_3$ film in our laboratory. At that time, I was still working on $BiFeO_3$ but, because he had to leave, I got in charge of this project. Many samples after this, has become the subject of my thesis. I would also like to thank Dr. Diego Rubi. From you, I have learned how to perform magnetic measurements. I have benefited from your knowledge and I am very grateful for that. I would also like to thank Dr. Dan Mannix for the time spent working together on the structure of the $TbMnO_3$ thin films during the synchrotron time at the ESRF in Grenoble, France. Your skills and knowledge of the beamline made the measurements a very nice time with lots of useful data that were crucial for this work. I hope we can continue investigating properties of materials. I would also like to thank Dr. Wolfgang Caliebe for his technical help during the synchrotron measurements at the W1 beamline in HASYLAB, Hamburg, Germany. Thank you very much for your availability and quick response during the measurements. I also have to thank Sriram Venkatesan, Dr. ir. Bart Kooi and Prof. dr. Jeff de Hosson for the TEM measurements presented in this thesis and for the very useful discussions. I would also like to thank ir. Gert Ten Brink for the SEM pictures and EDX analysis of some the PLD targets, which are not presented

in this thesis but were very important for other projects. I would also like to thank Prof. dr. Ria Broer and Prof. dr. Coen de Graaf for performing the cluster calculations presented in Chapter 4. Those results were crucial for the understanding of our experimental data and the answer would not have come out without your input. I would also like to thank all the members from the MaCoMuFi (Magnetoelectric coupling on multiferroic thin films) project for the useful discussions and the very interesting work being performed from groups involved in this project. Specially, useful discussions with Xavier Marti and Florencio Sanchez are greatly acknowledged. I would also like to thank Dr. Maxim Mostovoy for useful discussions. I would also like to thank Prof. dr. Petra Rudolf and Regis Gengler and Tatiana Landaluce Fernandez, from her group, for allowing me some XPS time and the useful help and discussion during some measurements. I would also like to thank Henk and Jacob for their technical expertise that helped solving and teaching how to solve technical problems. Many things would not have been possible without you. I would also like to thank Henriet for the administrative work. You were always very helpful and informative about administrative matters that makes my daily life easier.

I feel very grateful to Prof. Josep Fontcuberta, Prof. dr. Petra Rudolf and Prof. dr. ir. Paul van Loosdrecht for being members of my reading committee and for their useful suggestions to improve the manuscript.

I will remember forever my stay in Groningen in the group of Solid State Chemistry. Thanks to all the group members for the work atmosphere. The combination of a thin film part and a bulk part within the group made the discussions really interesting and inspiring. Thank you, Gwilherm, Umut, Claire, Mufti and Johan for the nice scientific discussions and your experimental skills. I would not have been able to reach that point in the measurement of the physical properties without our discussions. Specially, I would like to thank Gwilherm, Claire, Umut and Mufti for the very nice discussion. Of course, I would also like to thank Gijsbert and Ard for the useful discussions concerning the thin film part of my PhD work. Ard, your knowledge of the PLD system was crucial in the setup of the lab when we all started. Without you, Henk and Gustau, it would have taken much more time for the system to be ready when it arrived. We shared the same office during those four years and I thank you for never complaining about the perpetual mess on my desk. Gijsbert, thank you for the valuable and enjoyable discussions.

I also thank all the past, current and new members of the Solid State Chemistry group. Thank you for contributing to the life of the lab and forsharing discussions. Thank you Diego, Anne, Mylene, Claire, Mufti, Gwilherm, Anthony, Saeedeh, Gijsbert, Ard, Coen, Umut, Aramel, Josee, Brian, Jeroen, Johan, Henk, Jacob, Graeme, Syarif, Igor, Szili, Oana, Shiva and visitors Alexander, Irina, Javier and Eric. I would also like to thank all the friends I met in Groningen during those 4 years. First of all, I would

like to thank the 'French' mafia: Gwilherm, Aymeric, Claire, Galice, Mélanie, Jolanda, Damien, Bérénice, Anthony, Julien, Juliette, Martijn. Thank you all for the nice moments we shared. Thank you also for sharing many things and for your friendship. I would also like to thank the 'Italian/Spanish' mafia: Alessio, Filipo, Andrea, Daniele, Tatiana, Luminita. Thank you for your friendship and the nice time we shared. I would also like to thank Primoz, Tom, Simon, Andreas, Gaston, Dejan for nice drinks and discussions and people from the volley-ball I enjoyed playing with. I would also like to thank all the people I met during my short stay in the student house. Thank you Jeanine, Thanos, Elyse, Adam, Agatha, Amara, Mani, Max, Katharina, Soren. I also would like to thank all the people that I might have forgotten to mention for sharing time. Finally, I would like to thank my family for their long distance support over the four years. I cannot say how much I love you all and I dedicate this work to the freedom you gave me to pursue my studies around France and further. Without all this, I would not be where I am today and I am forever grateful.

Christophe Daumont
Groningen
September 21, 2009